Ballistic Majorana nanowire devices

Gül, Ö.

DOI
10.4233/uuid:5f84f8a9-b4e7-4248-a9cb-be9bde19b69d

Publication date
2017

Document Version
Final published version

Citation (APA)
Gül, Ö. (2017). *Ballistic Majorana nanowire devices*. [Dissertation (TU Delft), Delft University of Technology]. https://doi.org/10.4233/uuid:5f84f8a9-b4e7-4248-a9cb-be9bde19b69d

Önder Gül

Ballistic Majorana nanowire devices

Ballistic Majorana nanowire devices

Proefschrift

ter verkrijging van de graad van doctor
aan de Technische Universiteit Delft
op gezag van de Rector Magnificus Prof. Ir. K.C.A.M. Luyben,
voorzitter van het College voor Promoties,
in het openbaar te verdedigen op woensdag 18 oktober 2017 om 15:00 uur

door

Önder GÜL

Diplom-Ingenieur, Electrical Engineering and Information Technology,
RWTH Aachen University, Duitsland,
geboren te Konya, Turkije.

This dissertation has been approved by the promotors:
Prof. Dr. L. P. Kouwenhoven
Prof. Dr. E. P. A. M. Bakkers

Composition of the doctoral committee:

Chairman	
Rector Magnificus	Delft University of Technology
Promotors	
Prof. Dr. L. P. Kouwenhoven	Delft University of Technology
Prof. Dr. E. P. A. M. Bakkers	Delft University of Technology
Independent members	
Prof. Dr. C. M. Marcus	University of Copenhagen, Denmark
Dr. S. de Franceschi	CEA Grenoble, France
Prof. Dr. L. M. K. Vandersypen	Delft University of Technology
Prof. Dr. Y. M. Blanter	Delft University of Technology
Other member	
Dr. S. Goswami	Delft University of Technology

Printed by: Gildeprint

Cover art: Pattern made up of the first 15 prime knots from
commons.wikimedia.org/wiki/File:Knot_table.svg
Design by Tanja Vuksanovic & Önder Gül

Casimir PhD Series, Delft-Leiden 2017-29

ISBN 978-90-8593-313-7

An electronic version of this dissertation is available at
http://repository.tudelft.nl/.

Contents

Summary

This dissertation reports a series of electron transport experiments on semiconductor nanowires towards realizing the hypothesized topological quantum computation. A topological quantum computer manipulates information that is stored nonlocally in the topology of a physical system. Such an operation possesses advantages over the current quantum computation platforms due to its robustness against local sources of decoherence, offering a natural fault-tolerance. Among various candidate platforms to realize topological quantum computation, semiconductor nanowires with strong spin–orbit coupling attached to conventional superconductors have emerged as a prime contender. The predicted topological properties of such a system is associated with the emergence of Majorana modes.

The first experimental studies of Majoranas in semiconductor nanowires have been reported in 2012, shorty after which the experiments in this dissertation have been performed, spanning a four year period between 2013 and 2016. During this period, the presence of disorder has been considered to be the main obstacle towards the realization of a topological quantum computer based on semiconductor nanowires. Disorder can mimic the experimentally measurable properties of Majoranas, or can render the promise of fault-tolerance ineffective. The experiments in this dissertation aim for eliminating the disorder on the surface of the nanowire, and in the interface between the nanowire and the superconductor.

The dissertation starts with introducing the reader to the profound importance of topology in condensed matter physics (Chapter 1), after which the theoretical background of the reported experiments is covered (Chapter 2). The following chapters report experiments studying and reducing the disorder on the semiconductor nanowire surface (Chapter 3), and in the superconductor–semiconductor nanowire interface (Chapter 4). The reduction of disorder results in an experimental observation of ballistic superconductivity in semiconductor nanowires, reported in Chapter 5. Finally, in Chapter 6, we include the materials improvements reported in the previous chapters in the devices allowing for Majorana measurements. These devices show coexistence of ballistic transport and Majorana properties, excluding disorder mechanisms for the explanation of the observed Majorana properties. The dissertation is concluded with Chapter 7, which discusses future directions for realizing a topological quantum computer based on semiconductor nanowires.

Samenvatting

Dit proefschrift rapporteert een serie elektronen transport experimenten op halfgeleider nanodraden met als doel de hypothetische topologische kwantumberekening te realiseren. Een topologische kwantumcomputer manipuleert informatie die niet-lokaal is opgeslagen in de topologie van een fysisch systeem. Een dergelijke operatie heeft voordelen ten opzichte van de huidige kwantumberekeningsplatforms door zijn robuustheid tegen lokale bronnen van decoherentie, wat een natuurlijke fouttolerantie biedt. Tussen verschillende kandidaat-platforms om topologische kwantumberekening te realiseren, zijn halfgeleider nanodraden met een sterke spin–baankoppeling gekoppeld aan conventionele supergeleiders naar voren gekomen als een veelbelovend platform. De voorspelde topologische eigenschappen van een dergelijk systeem zijn verbonden met de verschijning van Majorana modes.

De eerste experimentele studies van Majoranas in halfgeleider nanodraden zijn gerapporteerd in 2012, waarna de experimenten in dit proefschrift zijn uitgevoerd, verspreid over een periode van vier jaar tussen 2013 en 2016. Tijdens deze periode werd de aanwezigheid van wanorde beschouwd als het belangrijkste obstakel voor de realisatie van een topologische kwantumcomputer op basis van halfgeleider nanodraden. Wanorde kan de experimenteel meetbare eigenschappen van Majoranas nabootsen, of kan de belofte van fouttolerantie ineffectief maken. De experimenten in dit proefschrift streven ernaar om de wanorde op het oppervlak van de nanodraad en in het contactvlak tussen de nanodraad en de supergeleider te elimineren.

Het proefschrift begint met het aan de lezer introduceren van het grote belang van topologie in de vaste stof fysica (hoofdstuk 1), waarna de theoretische achtergrond van de gerapporteerde experimenten wordt behandeld (hoofdstuk 2). De volgende hoofdstukken rapporteren experimenten die de wanorde op het halfgeleider nanodraad oppervlak (hoofdstuk 3) en in het supergeleider–halfgeleider nanodraad contactvlak (hoofdstuk 4) bestuderen en verminderen. De vermindering van de wanorde resulteert in een experimentele waarneming van ballistische supergeleiding in halfgeleider nanodraden, gerapporteerd in hoofdstuk 5. Tot slot nemen we in hoofdstuk 6 de in de voorgaande hoofdstukken gerapporteerde materiaalverbeteringen in de nanodraad devices op, waardoor Majorana-metingen mogelijk zijn. Deze devices tonen coëxistentie van ballistische transport en Majorana eigenschappen, waardoor wanorde mechanismen kunnen worden uitgesloten als verklaring van de waargenomen Majorana eigenschappen. Het proefschrift wordt afgesloten met hoofdstuk 7, waarin toekomstige stappen worden besproken voor het realiseren van een topologische kwantumcomputer op basis van halfgeleider nanodraden.

1

Introduction

1

Some time in elementary school we all learn about the states of matter: solid, liquid, gas. Water, for example, is a liquid characterized by H_2O molecules that are free to move in all directions. This free movement allows water to take any arbitrary shape. Ice, on the other hand, is a solid state of matter. Unlike water, ice has structural rigidity which arises from the ordered arrangement of its molecules. In most cases, solids consist of crystals which can be thought as periodic patterns of atoms, ions or molecules. A two-dimensional crystal is illustrated in Figure 1.1 (top) by a tessellation of the Dutch artist M.C. Escher. The entire pattern can be reconstructed by repeating the motif, in this case a rhombus, shown in Figure 1.1 (bottom). This is called translational symmetry, an essential property of crystals. Note, however, that the reconstruction would only work when repeating the unit cell along certain directions. For other directions, the pattern would look different and form a different crystal. In other words, crystals have discrete (discontinuous) translational symmetry. On the contrary, water has continuous translational symmetry. This is because a rearrangement of water molecules, for example by putting it in a different container, would not change its physical properties.

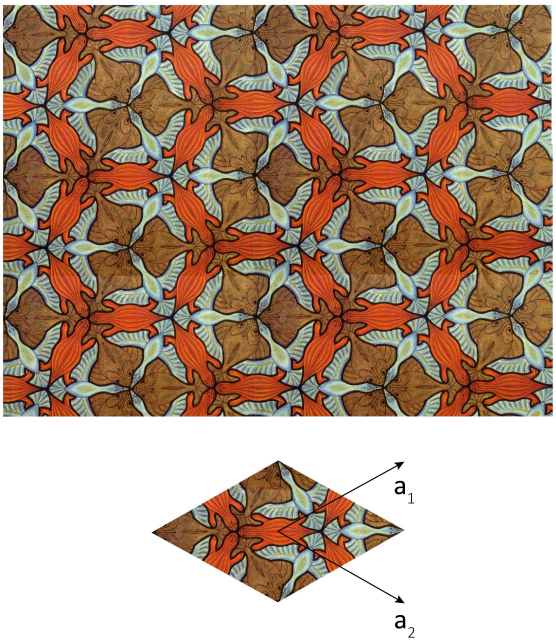

Figure 1.1 | *Fish / Duck / Lizard* (No. 69) by M.C. Escher illustrating a planar lattice. Top figure shows a pattern consisting of a periodic arrangement of fish, turtles and birds representing a two-dimensional crystal. Bottom figure shows the motif, or the unit cell, from which the top pattern can be reconstructed. a_1 and a_2 are the unit vectors which, together with the unit cell, define the crystal. Figure used by permission [1].

When a liquid solidifies into a crystal, it changes from a phase with continuous symmetry, or a high-symmetry state, to a phase where the continuous symmetry is reduced to a discrete set of symmetries, a low-symmetry state [2]. A change of symmetry is the underlying cause of most phase transitions observed in condensed matter physics. Fig-

ure 1.2 illustrates two important examples: Top panel shows the ferroelectric phase transition of lead titanate, a material with wide range of applications as a transducer due to its piezoelectricity. The phase transition is a result of a shift of the ions in the crystal upon lowering the temperature below a critical value, which changes the structure reducing the symmetry. In the bottom panel a ferromagnetic phase transition is depicted where the randomly oriented electron spins can align below a critical temperature, the hallmark of magnets. In this case, random orientation of the electron spins results in a continuous rotational symmetry which is broken in the ferromagnetic phase, similar to freezing of water. Another example is the superconducting phase transition which is associated by broken electromagnetic gauge symmetry. We will learn more about superconductors in the following chapters.

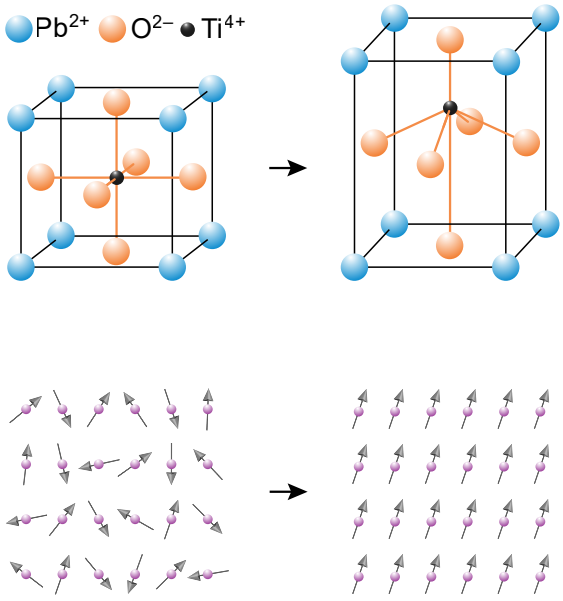

Figure 1.2 | Ferroelectric and ferromagnetic phase transition. Top panel shows the phase transition of lead titanate ($PbTiO_3$) to a ferroelectric phase due to shifting ions which changes the crystal structure from cubic to tetragonal. Bottom panel depicts a ferromagnetic phase transition. Here, the randomly oriented atomic magnetic moments, or the spins, in the paramagnetic phase align below a critical temperature resulting in a magnetization. Top panel adapted from [3].

Characterizing phase transitions by a change in the underlying symmetries of a system was developed in 1940s by the Russian physicist Lev Landau, and since then his approach has been applied to all states of matter for many years. However, in 1980s this paradigm was challenged by the discovery of the quantum Hall effect [4] which provided an example of a unique state that does not arise from a change in symmetry. Instead, quantum Hall state is characterized by its distinct topology [5], which does not depend on the specific geometry or smooth changes in material parameters, illustrated in Figure 1.3. This robustness is manifested in precise quantization of Hall conductance in

1

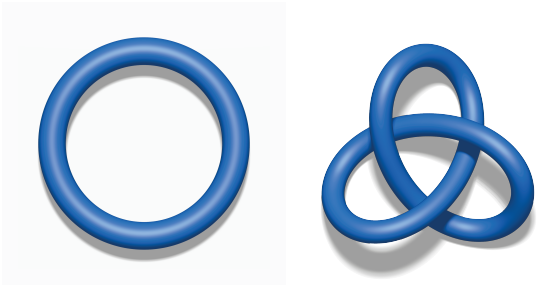

Figure 1.3 | Topological distinction of matter. The trivial knot, or unknot, (left) and the trefoil knot (right) cannot be transformed into each other without cutting and refixing. This is due to the differences in their topology which is not affected by smoothly varying their shape, for example by bending or squeezing. While the topology of knots can be visualized in position space, the distinct topology of the quantum Hall state becomes apparent in momentum space. Adapted from [6].

units of e^2/h which consists of two fundamental constants of nature: e the elementary charge and h the Planck constant, shown in Figure 1.4. This quantization is universal and insensitive to various experimental conditions such as the type or purity of the material, which has led quantum Hall effect to be used for maintaining the standard of electrical resistance. Both the experimental discovery of quantum Hall effect and the theoretical findings of topological states have been awarded by a Nobel Prize, respectively, to Klitzing in 1985, and to Thouless, Haldane and Kosterlitz in 2016 [2].

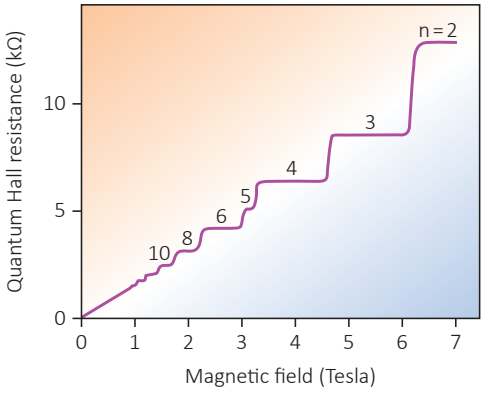

Figure 1.4 | Quantum Hall effect. The measured quantum Hall resistance, or the inverse of conductance, is plotted as a function of applied magnetic field. Quantum Hall resistance is given by $n^{-1} \times h/e^2$, where n is an integer characterizing each plateau and $h/e^2 \approx 26\,\mathrm{k\Omega}$. The quantization is evident from the staircase-like shape of the measured resistance. Adapted from [7].

In the past decade the field of topology in condensed matter has substantially grown by the prediction and the realization of new types of topological states [8]. These so-called topological insulators share similarities with the quantum Hall state but differ in that they do not require an externally applied magnetic field. Instead, the topological

state is achieved by spin–orbit coupling, a relativistic effect which couples the spin and the momentum of electrons, and causes electrons that are moving through a crystal to feel an internal momentum-dependent magnetic field. The effect of spin–orbit coupling to the dispersion of electrons is introduced in the following chapter.

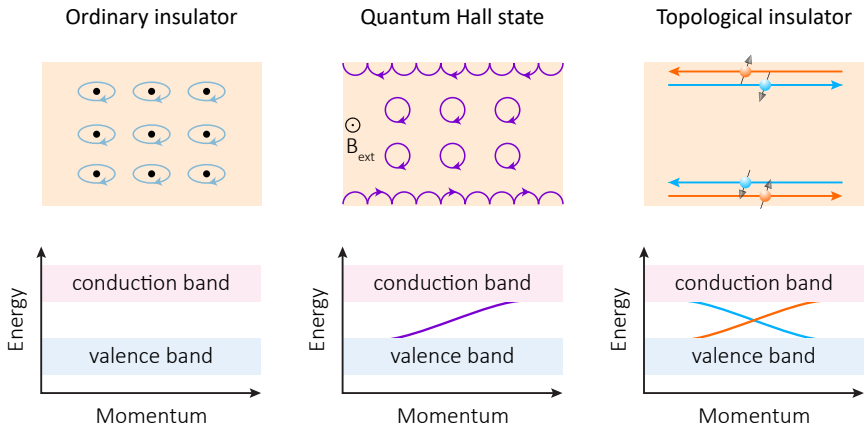

Figure 1.5 | Ordinary insulator, quantum Hall state and topological insulator. Electronic states can have different topologies. In ordinary insulators, the outermost electrons are localized around the ion cores and cannot propagate freely in the crystal. An energy gap separates the localized valence electrons from the available excitation states in the conduction band. In the quantum Hall regime, the external magnetic field confines the electrons in cyclotron orbits and opens an energy gap. However, there are conducting gapless boundary modes along the edges of the crystal due to the nontrivial topology of the quantum Hall state. Topological insulators are similar to the quantum Hall state and have an energy gap in the bulk of the crystal. However, gapless boundary modes result from spin–orbit coupling and do not require an external magnetic field. Because of this difference, there are two counter-propogating boundary modes which carry opposite spin. All three states are topologically distinct. Adapted from [8].

Past decade's discoveries have led the intriguing concept of topology to not only provide unique insight into physics of materials, but also to guide the design of novel devices for practical applications. A particularly exciting avenue is to use topology to realize a quantum computer [9]. Quantum computers are predicted to outperform classical computers for certain tasks but their state-of-the-art building blocks, called quantum bits or qubits, are still fragile and require extreme conditions of operation. Even a small interaction of a qubit with its environment can spoil the stored information causing computational errors. Current efforts to realize a quantum computer are therefore directed towards error-correction [10]. Topological states of matter, on the other hand, promise a natural alternative for error-protected quantum computation owing to their robustness against small changes in the environment.

In 2008 Fu and Kane predicted that the combination of a topological insulator with an ordinary s-wave superconductor supports Majorana modes, the zero-energy excitations of a topological superconductor [11]. Because of their non-Abelian statistics, which is different from fermion and boson statistics, Majorana modes can be used as building blocks of a topological quantum computer [9]. Fu and Kane's seminal study has enabled hybrid approaches for a condensed matter realization of Majorana modes. Until

then such research efforts had been limited to rare p-wave superconductors or fractional quantum Hall systems, materials that are in the quantum Hall state but additionally include electron-electron interaction, which demand very high purity and very low temperatures. Their proposal and the following ones have led many other materials in combination with common superconductors to be pursued for Majoranas. Besides topological insulators, these materials include graphene [12], two-dimensional electron gases [13], atomic chains [14], and semiconductor nanowires [15, 16]—the scope of this dissertation.

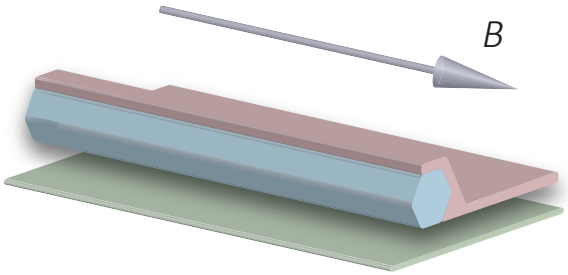

Figure 1.6 | A Majorana nanowire device. A semiconductor nanowire with spin–orbit coupling (blue) is attached to a superconductor (pink). An electrostatic gate (green) tunes the electron density in the nanowire. An external magnetic field B is oriented along the wire.

Majorana research in semiconductor nanowires was initiated in 2010 by two theory works [17, 18], which outlined superconductivity, spin–orbit coupling, electrostatic tunability, and finally an external magnetic field as the requirements (Figure 1.6), the first two being common to all proposals following Fu and Kane's hybrid approach. Because both superconductivity [19] and spin–orbit coupling [20] were previously demonstrated in electrostatically tunable semiconductor nanowires, they have offered a natural platform to realize a topological superconducting state. Soon after, several experiments reported characteristic Majorana signatures in spin–orbit coupled semiconductor nanowires combined with superconductors [15, 16, 21–27], which we call here Majorana nanowire devices.

Like all topological systems, Majorana nanowire devices are characterized by a degenerate ground state (there are more than one configuration with the lowest energy) and an energy gap between the ground state and the rest of the excitations. The robustness of the topology ultimately relies on this energy gap, the so-called topological gap. Several studies have demonstrated that the topological gap is adversely affected by disorder [28–30]. Morover, disorder has been both theoretically and experimentally shown to mimic characteristic Majorana signatures [31–36]. This dissertation reports experiments aiming to reduce the disorder in indium antimonide (InSb) Majorana nanowire devices, and has the following outline:

Chapter 2 introduces the theoretical concepts related to the experiments reported in the following chapters.

Chapter 3 reports experiments demonstrating an improvement in nanowire mobility, an inverse measure for disorder. The improvement is realized by optimizing various exper-

imental conditions during the fabrication of nanowire devices. The devices reported in the following chapters have been fabricated using this optimized fabrication recipe.

Chapter 4 reports experiments demonstrating an improvement in the induced superconducting gap in the semiconductor nanowire which is directly related to the topological gap. The improvement is realized by increasing the uniformity of the superconductor–semiconductor nanowire interface. These interface improvements have been included in the experiments reported in the following chapters.

Chapter 5 reports experiments demonstrating ballistic transport in semiconductor nanowires with induced superconductivity, the hallmark of low-disorder transport regime. Ballistic transport is achieved owing to the device improvements reported in the previous chapters.

Chapter 6 reports experiments demonstrating characteristic Majorana signatures in semiconductor nanowire devices exhibiting ballistic transport properties. This observation excludes the known alternative explanations for Majorana signatures that invoke disorder.

Chapter 7 concludes the dissertation by summarizing the results and providing an outlook.

References

[1] *Fish / Duck / Lizard* (No. 69) by M. C. Escher. All M. C. Escher works ©2017 The M. C. Escher Company - The Netherlands. All rights reserved. www.mcescher.com

[2] *Topological phase transitions and topological phases of matter*. Scientific Background on the Nobel Prize in Physics 2016, compiled by the Class for Physics of the Royal Swedish Academy of Sciences (2016)

[3] Perovskite image by Pinin. commons.wikimedia.org/wiki/File:Perovskite.svg

[4] Klitzing, K. v.; Dorda, G. & Pepper, M. New method for high-accuracy determination of the fine-structure constant based on quantized Hall resistance. *Phys. Rev. Lett.* **45,** 494 (1980)

[5] Thouless, D. J.; Kohmoto, M.; Nightingale, M. P. & den Nijs, M. Quantized Hall Conductance in a Two-Dimensional Periodic Potential. *Phys. Rev. Lett.* **49,** 405 (1982)

[6] Images of unknot and trefoil knot by Jim.belk.
commons.wikimedia.org/wiki/File:Blue_Unknot.png
commons.wikimedia.org/wiki/File:Blue_Trefoil_Knot.png

[7] Avron, J.; Osadchy, D. & Seiler, R. A Topological Look at the Quantum Hall Effect. *Physics Today* **56,** 38 (2003)

[8] Kane, C. L. & Hasan, M. Z. Topological insulators. *Rev. Mod. Phys.* **82,** 3045 (2010)

[9] Nayak, C.; Simon, S. H.; Stern, A.; Freedman, M. & Das Sarma, S. Non-Abelian anyons and topological quantum computation. *Rev. Mod. Phys.* **80,** 1083 (2008)

[10] Lidar, D. A. & Brun, T. A. *Quantum Error Correction.* Cambridge University Press (2013)

[11] Fu, L.; & Kane, C. L. Superconducting Proximity Effect and Majorana Fermions at the Surface of a Topological Insulator. *Phys. Rev. Lett.* **100,** 096407 (2008)

[12] Lee, G.-H. et al. Inducing superconducting correlation in quantum Hall edge states. *Nature Phys.* **13,** 693 (2017)

[13] Suominen, H. J. et al. Scalable Majorana devices. arXiv:1703.03699 (2017)

[14] Nadj-Perge, S. et al. Observation of Majorana fermions in ferromagnetic atomic chains on a superconductor. *Science* **346,** 602 (2014)

[15] Mourik, V. et al. Signatures of Majorana fermions in hybrid superconductor-semiconductor nanowire devices. *Science* **336,** 1003-1007 (2012)

[16] Albrecht, S. M. et al. Exponential protection of zero modes in Majorana islands. *Nature* **531,** 206-209 (2016)

[17] Lutchyn, R. M., Sau, J. D. & Das Sarma, S. Majorana fermions and a topological phase transition in semiconductor-superconductor heterostructures. *Phys. Rev. Lett.* **105,** 077001 (2010)

[18] Oreg, Y., Refael, G. & von Oppen, F. Helical liquids and Majorana bound states in quantum wires. *Phys. Rev. Lett.* **105,** 177002 (2010)

[19] Doh, Y.-J. et al. Tunable Supercurrent Through Semiconductor Nanowires. *Science* **309,** 272 (2005)

[20] Fasth, C. et al. Direct Measurement of the Spin-Orbit Interaction in a Two-Electron InAs Nanowire Quantum Dot. *Phys. Rev. Lett.* **98,** 266801 (2007)

[21] Das, A. et al. Zero-bias peaks and splitting in an Al-InAs nanowire topological superconductor as a signature of Majorana fermions. *Nature Phys.* **8,** 887-895 (2012)

[22] Rokhinson, L. P., Liu, X. & Furdyna, J. K. The fractional a.c. Josephson effect in a semiconductor–superconductor nanowire as a signature of Majorana particles. *Nature Phys.* **8,** 795-799 (2012)

[23] Deng, M. T. et al. Anomalous zero-bias conductance peak in a Nb–InSb nanowire–Nb hybrid device. *Nano Lett.* **12,** 6414-6419 (2012)

[24] Churchill, H. O. H. et al. Superconductor-nanowire devices from tunneling to the multichannel regime: Zero-bias oscillations and magnetoconductance crossover. *Phys. Rev. B* **87,** 241401(R) (2013)

[25] Finck, A. D. K., Van Harlingen, D. J., Mohseni, P. K., Jung, K. & Li, X. Anomalous modulation of a zero-bias peak in a hybrid nanowire-superconductor device. *Phys. Rev. Lett.* **110,** 126406 (2013)

[26] Deng, M. T. et al. Majorana bound state in a coupled quantum-dot hybrid-nanowire system. *Science* **354,** 1557-1562 (2016)

[27] Chen, J. et al. Experimental phase diagram of a one-dimensional topological superconductor. arXiv:1610.04555 (2016)

[28] Potter, A. C. & Lee, P. A. Engineering a $p + ip$ superconductor: Comparison of topological insulator and Rashba spin-orbit-coupled materials. *Phys. Rev. B* **83,** 184520 (2011)

[29] Sau, J. D.; Tewari, S. & Das Sarma, S. Experimental and materials considerations for the topological superconducting state in electron- and hole-doped semiconductors: Searching for non-Abelian Majorana modes in 1D nanowires and 2D heterostructures. *Phys. Rev. B* **85,** 064512 (2012)

[30] Takei, S., Fregoso, B. M., Hui, H.-Y., Lobos, A. M. & Das Sarma, S. Soft superconducting gap in semiconductor Majorana nanowires. *Phys. Rev. Lett.* **110,** 186803 (2013)

[31] Liu, J., Potter, A. C., Law, K. T. & Lee, P. A. Zero-bias peaks in the tunneling conductance of spin-orbit-coupled superconducting wires with and without Majorana end-states. *Phys. Rev. Lett.* **109,** 267002 (2012)

[32] Bagrets, D. & Altland, A. Class D spectral peak in Majorana quantum wires. *Phys. Rev. Lett.* **109,** 227005 (2012)

[33] Pikulin, D. I., Dahlhaus, J. P., Wimmer, M., Schomerus, H. & Beenakker, C. W. J. A zero-voltage conductance peak from weak antilocalization in a Majorana nanowire. *New J. Phys.* **14,** 125011 (2012)

[34] Lee, E. J. H. et al. Zero-Bias anomaly in a nanowire quantum dot coupled to superconductors. *Phys. Rev. Lett.* **109,** 186802 (2012)

[35] Lee, E. J. H. et al. Spin-resolved Andreev levels and parity crossings in hybrid superconductor-semiconductor nanostructures. *Nature Nanotech.* **9,** 79-84 (2014)

[36] Liu, C.-X., Sau, J. D., Stanescu, T. D. & Das Sarma, S. Andreev bound states versus Majorana bound states in quantum dot-nanowire-superconductor hybrid structures: Trivial versus topological zero-bias conductance peaks. arXiv:1705.02035 (2017)

2

Theory

2.1. Introduction to superconductivity

In this section we qualitatively introduce superconductivity which the experiments reported in this thesis use to create Majoranas.

2

Superconductivity is a phenomenon of zero electrical resistance (perfect conductance) [1] and an expulsion of magnetic field (perfect diamagnetism) [2]. It occurs in certain materials below a characteristic critical temperature and critical field. Importantly, superconducting phase is associated with electrons behaving coherently which lend themselves to be described by a single wave function.

Superconductivity is treated by two different approaches. First of these is the *Ginzburg–Landau theory* [3, 4] which concentrates on superconducting electrons and accounts for the macroscopic quantum mechanics of the superconducting state. While this approach is very successful in describing the electrodynamics of superconductors, it does not treat superconductivity at a microscopic level due to its phenomenological nature [5]. Since we are interested in a microscopic treatment, this approach is not covered in this thesis. Instead we will make use of *Bardeen–Cooper–Schrieffer (BCS) theory* of superconductivity which we qualitatively introduce below.

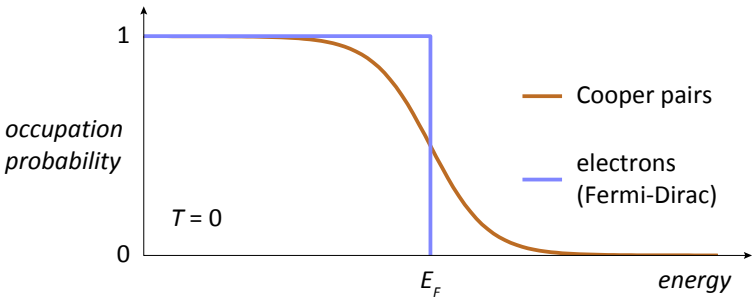

Figure 2.1 | Occupation probability of Cooper pairs. Occupation of the ground state at zero temperature in the presence of an attractive interaction between electrons. For comparison Fermi-Dirac distribution is also plotted which describes the ground state occupation of a normal metal with noninteracting electrons. (In a normal metal electrons occupy all states below the Fermi energy E_F leaving all states empty above E_F.) Note that the superconducting ground state is a many-body state from which excitations below an energy Δ are not allowed. This results in the superconducting energy gap Δ in the excitation spectrum which is not visible in this representation. The excitation properties of superconductors are introduced below in Section 2.2.

Microscopic mechanism of superconductivity was first explained by Bardeen, Cooper, and Schrieffer, within the framework of what is now called the BCS theory, based on attractive interactions between electrons [6]. BCS theory shows that the ground state of a system of electrons with attractive interactions is reached when electrons occupy k-states in pairs [7]. These pairs, the so-called *Cooper pairs*, consist of electrons with opposite momentum and spin, and form the many-body ground state of the superconducting phase. While BCS pairing model does not depend on the origin of the attractive interaction, it is found to be mediated by the collective motion of the positively charged ion-cores in the lattice that are called phonons [5]. Here, an electron scatters from state k to k' emitting a virtual phonon which is absorbed by its partner-electron scattering

from $-k$ to $-k'$ [8]. Because this process requires the availability of both occupied k-states and unoccupied k'-states within a certain energy window, electrons do not prefer a step-function distribution which is energetically unfavourable even at zero temperature (contrary to normal metals, see Figure 2.1). Instead, electrons occupy states with energies above the Fermi energy to form Cooper pairs. Resulting kinetic energy increase is compensated by the bound state energy 2Δ, the minimum energy required to break a Cooper pair. Importantly, this minimum energy requirement corresponds to an energy gap in the excitation spectrum. The presence of an excitation gap from the many-body ground state dictates many important characteristics of superconductors, for example the ability to carry currents without dissipation.[1]

2.2. Bogoliubov–de Gennes formalism

Here we introduce a formalism to express excitations from the many-body ground state of a superconductor. Both the Majoranas and the charge transport between a superconductor and a normal conductor are described using these excitations.

In the previous section we have introduced the pairing of electrons with opposite momentum and spin. For such a system the effective Hamiltonian in momentum space, the so-called *pairing Hamiltonian*, can be written as [5, 10]

$$H_k = \sum_k E_k a_k^\dagger a_k - \sum_{k,l\in\delta} V_{kl} a_l^\dagger a_{-l}^\dagger a_{-k} a_k, \tag{2.1}$$

where a positive wave vector k (l) implies spin up and a negative wave vector spin down. The first sum accounts for the energy of noninteracting electrons $E_k = \hbar^2 k^2/2m^* - E_F$, with $\hbar$ denoting the reduced Plank constant, m^* the effective mass of electrons, and E_F the Fermi energy. $a^\dagger$ is the creation, a the annihilation, and $a^\dagger a$ the number operator for electrons. The second sum is the pairing term describing the attractive interaction of electrons within a small energy window around the Fermi level,[2] with V_{kl} the matrix element of the interaction potential. The pairing term which is quartic in electron operators can be simplified using mean-field approximation where the fluctuations of $a_{-k}a_k$ from their expectation values $\langle a_{-k}a_k\rangle$ are assumed to be minimal. Denoting $\langle a_{-k}a_k\rangle = b_k$ mean-field approximation implies $(a_l^\dagger a_{-l}^\dagger - b_l)(a_{-k}a_k - b_k) \approx 0$, and one arrives at the so-called *model Hamiltonian*

$$H_k = \sum_k E_k a_k^\dagger a_k - \sum_{k\in\delta} \left(\Delta_k a_k^\dagger a_{-k}^\dagger + \Delta_k^* a_{-k} a_k - \Delta_k b_k^*\right) \tag{2.2}$$

$$\text{with } \Delta_k = \sum_l V_{kl} b_l. \tag{2.3}$$

Here Δ_k is the superconducting pair function. An important implication of mean-field approximation is that the Hamiltonian no longer preserves the electron number due to

[1] Note that perfect conductivity does not directly follow from an excitation gap. For a BCS theory-based explanation of why superconductors *super*conduct readers are advised to refer to [9].

[2] The sum runs over a limited k and l values around the Fermi wave vector indicated by $k, l \in \delta$. This is because the superconducting pairing requires the availability of both occupied and empty k-states within a small energy window. For $E << E_F$ there are no empty states, for $E >> E_F$ there are no occupied states. Hence the attractive interaction affects only the electrons with energies close to E_F.

the terms creating and destroying *pairs* of electrons. However *parity*—or number of electrons (mod 2)—remains preserved. After inverse Fourier transforming the operators in momentum space, the Hamiltonian in position space can be written as [11]

$$H_r = \int dr \left(\sum_\sigma \psi_\sigma^\dagger H_0 \psi_\sigma + \Delta_r \psi_\uparrow^\dagger \psi_\downarrow^\dagger + \Delta_r^* \psi_\downarrow \psi_\uparrow \right), \tag{2.4}$$

now with spin index $\sigma = \uparrow$ or $\downarrow$ shown explicitly, where

$$H_0 = -\hbar^2 \nabla^2 / 2m^* + U_r - E_F \tag{2.5}$$

and ψ the annihilation operator for position eigenfunction. Here the scalar potential U_r and the pair potential Δ_r can vary spatially, which is in contrast to Equations (2.1) and (2.2) describing a homogeneous electron gas with attractive interactions. This choice is necessary to study inhomogeneous systems such as a normal conductor–superconductor interface. To conveniently describe excitations from the ground state of paired electrons, H_r in Equation (2.4) can be expressed in a new form

$$H_{\text{eff}} = E_g + \sum_n E_n c_n^\dagger c_n, \tag{2.6}$$

where the electron operators are replaced with the fermion operators for noninteracting particles, or *quasiparticles*, defined as [12]

$$c_n^\dagger = \int dr \left(u_n \psi_\uparrow^\dagger + v_n \psi_\downarrow \right). \tag{2.7}$$

This is the so-called *Bogoliubov transformation* where the new form of the Hamiltonian describes the ground state energy E_g of Cooper pairs and the excitation energy E_n of quasiparticle n. Quasiparticles are represented by a superposition of a spin-up electron and a spin-down hole with probability amplitudes u and v, respectively. They are electron-like for $|u|^2 > |v|^2$, and hole-like for the opposite case. These quasiparticle excitations can be described by the *Bogoliubov–de Gennes (BdG) equation*

$$\begin{pmatrix} H_0 & \Delta_r \\ \Delta_r^* & -H_0^* \end{pmatrix} \vec{\varphi} = E\vec{\varphi}, \quad \vec{\varphi} = \begin{pmatrix} u \\ v \end{pmatrix} \tag{2.8}$$

with H_0 the single particle Hamiltonian given in Equation (2.5). The pair potential Δ_r couples the two components of the quasiparticle vector $\vec{\varphi}$. For a homogeneous superconductor with $\Delta_r = \Delta_0 = |\Delta_0|$ and plane wave solutions for quasiparticles, the excitation energy E is given as[3] [13–15]

$$E = \sqrt{\epsilon^2 + \Delta_0^2}, \quad \epsilon = \hbar^2 k^2 / 2m^* - E_F, \tag{2.9}$$

plotted in Figure 2.2. Here, ϵ can be both positive or negative. Positive ϵ denotes an electron-like excitation with wave vector $k > k_F = \sqrt{2m^* E_F}/\hbar$ and negative ϵ a hole-like

[3] BdG equations contain a double set of solutions with both positive and negative E which are not independent. Here we neglect negative E, which allows us to represent all electron solutions with wave vector $k > k_F$ and all hole solutions with $k < k_F$.

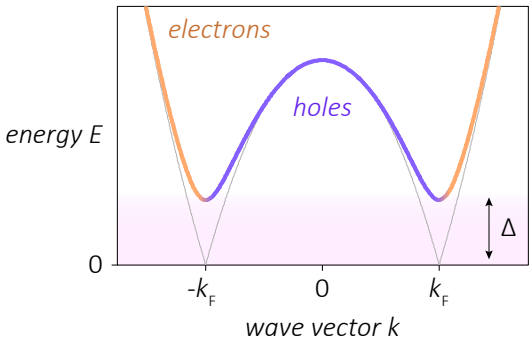

Figure 2.2 | Excitation spectrum of a superconductor. Energy solutions E of Bogoliubov–de Gennes equation is plotted as a function of wave vector k. Lowest possible excitation energy is Δ corresponding to the pairing-induced superconducting energy gap. For a quasiparticle to occupy an excited (single-particle) state, its energy must be larger than Δ. Since ground state consists of paired electrons, an energy of 2Δ is needed to create an excitation. For $|k| < k_F$ the excitations are hole-like with group velocity $\partial E/\hbar\partial k$ pointing opposite to the wave vector. For $|k| > k_F$ quasiparticles are electron-like. Faint gray line depicts the excitations for a normal conductor with $\Delta = 0$ for which the excitations can be arbitrarily small.

excitation ($k < k_F$), with k_F the Fermi wave vector. As an important consequence, for hole-like excitations the direction of the group velocity is opposite to the corresponding wave vector. The quasiparticle vectors have the form[4]

$$\vec{\varphi} = \begin{pmatrix} u_0 \\ v_0 \end{pmatrix} e^{\mathrm{i}kr} \tag{2.10}$$

$$u_0^2 = \tfrac{1}{2}\left(1 + \epsilon/E\right) \tag{2.11}$$

$$v_0^2 = 1 - u_0^2. \tag{2.12}$$

Equations (2.8) – (2.12) will be used to treat the charge transport between a normal conductor and a superconductor in the next section. Before that we turn our attention to the quasiparticle density of states.

Quasiparticle density of states. In the preceding part we described the excitations from the ground state using noninteracting quasiparticles via Bogoliubov transformation. The quasiparticles are of fermionic nature and are created (or destroyed) much the same way as the electrons in a normal conductor, i.e., there is a one-to-one correspondence between the quasiparticle operator c and the electron operator ψ. Therefore, one can obtain the quasiparticle density of states N_s by equating it to that of a normal conductor $N_s(E)dE = N_n(\epsilon)d\epsilon$, and assuming a constant density of states in the normal conductor $N_n(\epsilon) = N_0$. Using Equation (2.9) one obtains

$$N_s(E) = N_0 E/\sqrt{E^2 - \Delta^2}. \tag{2.13}$$

[4] Alternatively one can define $u_0^2 = \frac{1}{2}\left(1 + \sqrt{E^2 - \Delta^2}/E\right)$. However, since the second term is always positive, this definition does not distinguish between electron- and hole-like excitations. In this case separate definitions of quasiparticle vectors are required: $\vec{\varphi}_e = (u_0, v_0)$ for electron-like excitations, and $\vec{\varphi}_h = (v_0, u_0)$ for hole-like excitations.

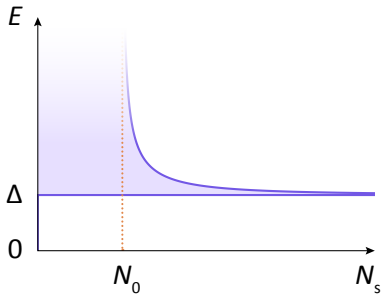

Figure 2.3 | Quasiparticle density of states. The density of excitation states in a superconductor N_s is plotted as a function of energy E. There are no states within the superconducting gap Δ. For $E = \Delta$ quasiparticle density of states diverges. Red dotted line depicts the normal density of states N_0 which is assumed to be constant for $E \ll E_F$.

Figure 2.3 shows the quasiparticle density of states N_s along with the density of states for a normal conductor. One can see that there are no states within the superconducting gap Δ. For $E = \Delta$ the density of state diverges. These divergent peaks are commonly referred to as *coherence peaks*.

2.3. Andreev reflection

Here we introduce a mechanism which maintains the charge transport between a superconductor and a normal conductor. This mechanism dictates the transport properties of Majorana nanowire devices.

In the previous section we have introduced the Bogoliubov–de Gennes equation describing excitations in a superconductor from the many-body ground state of Cooper pairs which we will use in the following to treat the charge transport between a normal conductor and a superconductor. We have seen that superconductors do not allow single-particle excitations below the superconducting energy gap Δ. This energy gap together with the coupling of electron- and hole-like excitations dramatically affect the transport between a superconductor and a normal conductor, described below.

Consider a normal conducting source in contact with a superconducting drain (see Figure 2.4). Electrons in the normal conductor with an energy $E > \Delta$ moving towards the superconductor can enter the superconductor by being converted into quasiparticles with the same energy. This, however, does not work for energies $E < \Delta$ since there are no quasiparticle states in the superconductor. Instead, electron excitations with such small energies are reflected from the superconductor as hole excitations with the same energy. This process, the so-called *Andreev reflection*, maintains the charge transport between a normal conductor and a superconductor [16]. Importantly, because hole excitations carry a positive charge, Andreev reflection implies $2e$ charge transport corresponding to an addition of a Cooper pair to the superconductor.

The general formalism describing the charge transport between a normal conductor and a superconductor is developed by Blonder, Tinkham, and Klapwijk known as the *BTK model* [13]. In addition to Andreev reflection, BTK model also includes normal re-

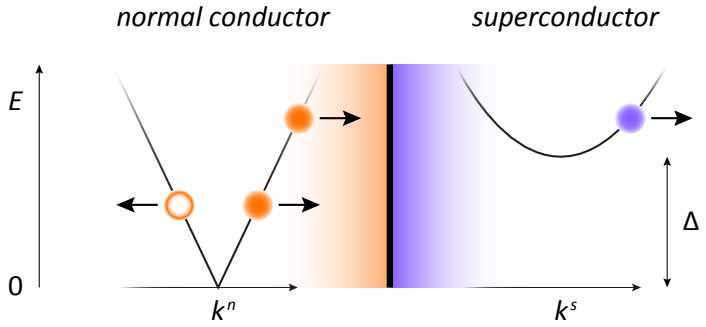

Figure 2.4 | Andreev reflection. Charge transport across an interface between a normal conductor (orange) and a superconductor (violet). Black curves represent the excitation spectrum on the both sides of the interface for positive wave vector k^n and k^s in the normal conductor and the superconductor, respectively. Filled circles depict the electrons, empty circles the holes. Arrows indicate the propagation direction of electrons and holes. An electron in the normal conductor with an energy $E > \Delta$ moving towards the superconductor enters the superconductor by being converted into a quasiparticle with the same energy. In contrast, an electron with $E < \Delta$ is reflected from the superconductor as a hole.

flection of charge carriers to account for backscattering due to an imperfect interface. This is achieved by introducing a potential barrier between the normal conductor and the superconductor. In this case, the wave solutions of the normal conductor include the incident electron, the Andreev reflected hole with coefficient r_A, and the normal reflected electron with coefficient r_N. Following Equations (2.8) – (2.12) waves propagating in the normal conductor are expressed as

$$\vec{\varphi}_n = \begin{pmatrix}1\\0\end{pmatrix} e^{\mathrm{i}k_n^+ r} + r_A \begin{pmatrix}0\\1\end{pmatrix} e^{\mathrm{i}k_n^- r} + r_N \begin{pmatrix}1\\0\end{pmatrix} e^{-\mathrm{i}k_n^+ r} \tag{2.14}$$

$$k_n^\pm = \left(k_F^2 \pm \frac{2m^*}{\hbar^2} E\right)^{1/2}, \tag{2.15}$$

where k^+ the wave vector for electrons and k^- the holes. The superconductor solutions are the transmitted electron-like and hole-like excitations with the coefficients t_e and t_h, respectively,

$$\vec{\varphi}_s = t_e \begin{pmatrix}u_0\\v_0\end{pmatrix} e^{\mathrm{i}k_s^+ r} + t_h \begin{pmatrix}u_0\\v_0\end{pmatrix} e^{-\mathrm{i}k_s^- r} \tag{2.16}$$

$$k_s^\pm = \left(k_F^2 \pm \frac{2m^*}{\hbar^2} \sqrt{E^2 - \Delta^2}\right)^{1/2}. \tag{2.17}$$

The coefficients can be obtained from the continuity of the waves at the interface. One can already see that for energies $E < \Delta$ there are no propagating solutions in the superconductor. The quasiparticle waves are exponentially damped away from the interface since wave vectors contain imaginary components. Only for energies $E > \Delta$ can the quasiparticles propagate into the superconductor. In the following we will not focus further on the solutions in the superconductor $\vec{\varphi}_s$, we instead refer the interested reader to [13, 15].

We now turn our attention to the wave solutions in the normal conductor. The probability of Andreev and normal reflection is given as

$$|r_A|^2 = \begin{cases} \dfrac{\Delta^2}{E^2+(\Delta^2-E^2)(2/T-1)^2} \\ u_0^2 v_0^2/\gamma^2 \end{cases}, \quad |r_N|^2 = \begin{cases} 1-|r_A|^2 & \text{for } E<\Delta \\ \dfrac{(1-T)(u_0^2-v_0^2)^2}{T^2\gamma^2} & \text{for } E>\Delta. \end{cases} \tag{2.18}$$

Here $\gamma = (u_0^2 - v_0^2)/T + v_0^2$, where T the transmission probability through the delta potential with weight $\hbar v_F (1/T-1)^{1/2}$, and v_F the Fermi velocity. Using these reflection probabilities, the electrical current I through a normal conductor–superconductor interface can be calculated via [13]

$$I = 2\frac{e}{h}\int dE\big(f(E-eV)-f(E)\big)\big(1+|r_A|^2-|r_N|^2\big), \tag{2.19}$$

with $f(E)$ the Fermi distribution and V the bias voltage where we assumed single subband occupation for the normal conductor. It is instructive to examine two important cases: If the bias voltage is much larger than the superconducting gap ($E = eV \gg \Delta$), the probability of Andreev reflection vanishes ($r_A = 0$), and the current becomes

$$I = TG_0V, \tag{2.20}$$

with $G_0 = 2e^2/h$ the conductance quantum. We will refer to the corresponding conductance $G_n = I/V = TG_0$ as the *above-gap* conductance, noting that G_n is also known in the literature as the *normal state* conductance since it is recovered for $\Delta = 0$ as well. For the second case we consider excitations with small energy $E = eV \ll \Delta$ and obtain the so-called *subgap* conductance [17]

$$G_s = \frac{I}{V} = \frac{2T^2}{(2-T)^2}G_0. \tag{2.21}$$

We will now compare the subgap conductance with the above-gap conductance to understand how Andreev reflection affects the charge transport (Figure 2.5). For high transmission ($T \to 1$) the subgap conductance is enhanced due to Andreev processes where an incoming electron is reflected as a hole at the interface generating a Cooper pair in the superconductor. For unit transmission probability Andreev reflection doubles the charge being transported from e to $2e$ which doubles the conductance: $G_s/G_n = 2$. On the other hand, for low transmission ($T \to 0$) the subgap conductance is suppressed. This is because unlike above-gap conductance which is linear in T, subgap conductance scales quadratically with the transmission $G_s \approx T^2/2$, leading to $G_s \ll G_n$ for low transmission values. Importantly, in this low transmission regime, the conductance reveals the density of excitation states in the superconductor (compare Figure 2.5b with Figure 2.3). The experiments reported in this thesis make use of this method (introduced below in Section 2.8) to probe excitations in a superconductor, such as Majorana modes.

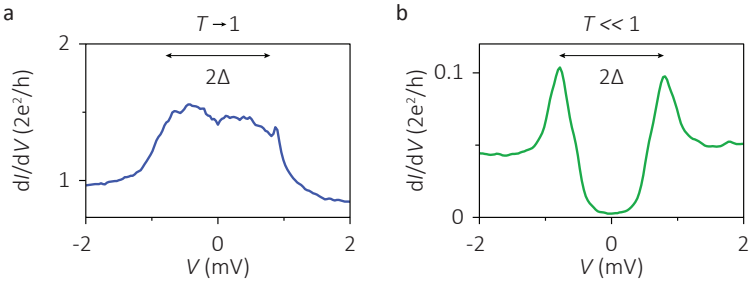

Figure 2.5 | Andreev transport between a semiconductor nanowire and a superconductor. Panels show the measured conductance dI/dV in units of $G_0 = 2e^2/h$ as a function of bias voltage V for the limiting cases of high and low transmission T. **a,** For high transmission $T \to 1$, the subgap conductance G_s is enhanced compared to the above-gap conductance G_n. **b,** For low transmission $T << 1$, the subgap conductance G_s is suppressed compared to the above-gap conductance G_n. In this low transmission regime, dI/dV reveals the density of excitation states in the superconductor. Note the coherence peaks at $|eV| = \Delta$ which indicate the superconducting gap edge. For $eV < \Delta$ there are no excitation states in the superconductor. For $eV > \Delta$ the density excitation states in the superconductor is finite and independent of the quasiparticle energy (eV).

2.4. Different types of superconducting pairing

In the previous sections we have described superconductivity based on pairing of electrons with opposite spin. However, although unconventional, other types of pairing are physically possible as well. Because emergence of Majoranas rely on a superconducting pairing of electrons with parallel spin component, we introduce below a generalized approach which can describe unconventional types of pairing.

We relax the assumption in Equations (2.1) – (2.3) that opposite wave vector indices imply opposite spin, and indicate the spin index explicitly. The superconducting pair function becomes

$$\Delta_{k,ss'} = \sum_l V_{kl,ss's''s'''}\, b_{l,s''s'''} \tag{2.22}$$

$$\text{with } b_{l,s''s'''} = \left\langle a_{-l,s''}\, a_{l,s'''} \right\rangle. \tag{2.23}$$

Here, k, l indicates the wave vector as before, and s the spin orientation. The pair function can now describe pairing of electrons with arbitrary spin orientation and be expressed as a matrix in spin space

$$\hat{\Delta}_k = \begin{pmatrix} \Delta_{k,\uparrow\uparrow} & \Delta_{k,\uparrow\downarrow} \\ \Delta_{k,\downarrow\uparrow} & \Delta_{k,\downarrow\downarrow} \end{pmatrix}, \tag{2.24}$$

with $\uparrow, \downarrow$ the spin orientation [18, 19]. Using fermion anticommutation rules, one can show that

$$b_{k,ss'} = -b_{-k,s's}. \tag{2.25}$$

To get an insight into how electrons are paired, we separate $b_{k,ss'}$ into an orbital part and a spin part: $b_{k,ss'} = \phi_k\, \chi_{ss'}$. For Equation (2.25) to hold, either ϕ_k is an odd function of k and $\chi_{ss'}$ is symmetric under particle exchange or ϕ_k is even in k and $\chi_{ss'}$ is antisymmetric

under particle exchange. The first case represents the odd parity spin-triplet pairing and the latter even parity spin-singlet pairing. The pair function can be generalized as

$$\hat{\Delta}_k = \left[\Delta_s(k) + \vec{\Delta}_t(k)\vec{\sigma}\right] i\sigma_y, \tag{2.26}$$

with $\Delta_s(k)$ the singlet pairing component, $\vec{\Delta}_t(k)$ the three-dimensional vector describing the triplet pairing component, and $\vec{\sigma} = (\sigma_x, \sigma_y, \sigma_z)$ the three-dimensional vector of Pauli matrices. Using this expression, a conventional (*s-wave*[5]) superconductor has the form

$$\hat{\Delta}_k = \begin{pmatrix} 0 & \Delta_{k,\uparrow\downarrow} \\ \Delta_{k,\downarrow\uparrow} & 0 \end{pmatrix} = \begin{pmatrix} 0 & \Delta_s(k) \\ -\Delta_s(k) & 0 \end{pmatrix} = \begin{pmatrix} 0 & \Delta_0 \\ -\Delta_0 & 0 \end{pmatrix}, \tag{2.27}$$

with $\Delta_s(k) = \sum_l V_{kl}\phi_l = \Delta_0$. Here, $\vec{\Delta}_t(k) = 0$ and $\chi_{ss'} = |\uparrow\downarrow\rangle - |\downarrow\uparrow\rangle$ reflecting the singlet pairing. Note that Δ_0 has no k dependence, a property of s-wave superconductors. Another singlet example is the so-called *d-wave* pairing with $\Delta_s(k) = \Delta_0(k_x^2 - k_y^2)/k_F$.

Among triplet superconductors, a notable case is the *p-wave* pairing with $\vec{\Delta}_t(k) = \Delta_0(k_x, k_y, 0)/k_F$. When the superconductor is spin-polarized, this results in a pair function $\hat{\Delta}_k \propto k_x \pm ik_y$, the so-called spinless $p_x \pm ip_y$ superconductivity. In two dimensions, this type of pairing leads to topological superconductivity with Majorana modes in vortex cores [20, 21]. Below we explicitly show the emergence of Majorana modes in a one-dimensional spinless p-wave superconductor.

2.5. Kitaev chain

Here we introduce a simple one-dimensional toy model which supports Majoranas. Although unphysical, this model illustrates how Majoranas emerge in superconducting wires, laying the groundwork for later realistic Majorana nanowire proposals which the experiments reported in this thesis follow.

A simple model in which Majoranas appear was introduced by Kitaev using a one-dimensional tight-binding representation of a p-wave superconductor, the so-called *Kitaev chain* [22]. Such a system can be described by

$$H = -\mu \sum_{j=1}^{n} \left(a_j^\dagger a_j - \tfrac{1}{2}\right) - t \sum_{j=1}^{n-1} \left(a_j^\dagger a_{j+1} + a_{j+1}^\dagger a_j\right) + \sum_{j=1}^{n-1} \left(\Delta a_j a_{j+1} + \Delta^* a_{j+1}^\dagger a_j^\dagger\right), \tag{2.28}$$

where μ is the chemical potential, a_i the electron annihilation operator, t the hopping amplitude, and Δ the superconducting gap. The same spin projection is assigned for all operators implying pairing of electrons with equal spins, the p-wave pairing introduced above. This spinless regime is in contrast to conventional (BCS) superconductivity introduced earlier in Equation (2.1) where pairing occurs for electrons with opposite spins, the s-wave pairing. Figure 2.6 depicts the Kitaev chain with n electron sites. Index j denotes the site of the electron. Superconductivity pairs the neighbouring electrons, where the site j couples with the site $j+1$. We now introduce the *Majorana operator* γ whose

[5] The pairing descriptions *s*, *p*, and *d*-wave relate to the atomic orbitals.

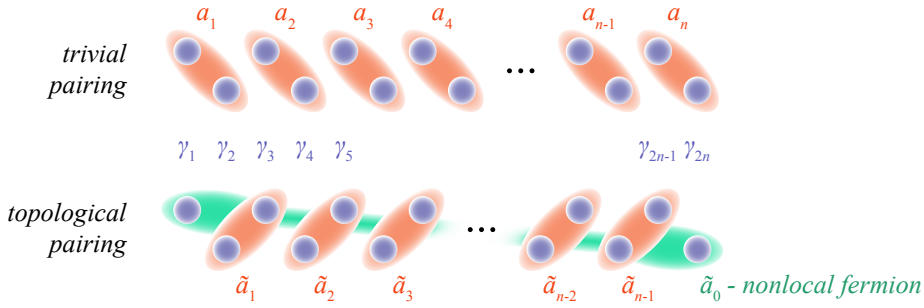

Figure 2.6 | Kitaev chain. Orange ellipses denote local electron (fermion) sites, violet circles the Majorana sites. A Majorana site with the operator γ is paired with an adjacent Majorana. For the trivial pairing, Majorana operators of the same electron site a_j are paired to form n number of local fermions $a_1 \dots a_n$. In contrast, for the topological pairing, Majorana operators from the neighbouring electron sites (a_j and a_{j+1}) are paired. As a result, Majorana sites on both ends cannot be paired with an adjacent Majorana. Instead, the unpaired Majoranas form a *nonlocal* fermion $\tilde{a}_0$ indicated in green. The remaining paired Majoranas can be expressed as $n-1$ number of local fermions $\tilde{a}_1 \dots \tilde{a}_{n-1}$.

construction can be imagined as splitting a fermion (electron) into its real and imaginary parts:

$$a_j = \tfrac{1}{2}(\gamma_{2j-1} + \mathrm{i}\gamma_{2j}) \tag{2.29}$$

$$a_j^\dagger = \tfrac{1}{2}(\gamma_{2j-1} - \mathrm{i}\gamma_{2j}). \tag{2.30}$$

Equation (2.28) can be expressed using these Majorana operators. The are two special cases for which the chain shows distinct excitation properties. Taking $t = \Delta = 0$ and $\mu < 0$ one arrives at

$$H = -\mathrm{i}\frac{\mu}{2}\sum_{j=1}^{n}\gamma_{2j-1}\gamma_{2j} = -\mu\sum_{j=1}^{n}\left(a_j^\dagger a_j - \tfrac{1}{2}\right). \tag{2.31}$$

This expression corresponds to the case where Majorana operators of the same electron site are paired, the so-called *topologically trivial* phase. In other words this case describes n electron sites which can be occupied by noninteracting fermions. There is a unique ground state with all electron sites being empty, which has an even parity (zero occupation). Excitations correspond to an electron site being occupied which has an energy $|\mu|$.

For the second case, one takes $t = \Delta \neq 0$ and $\mu = 0$, and the Hamiltonian reads

$$H = \mathrm{i}t\sum_{j=1}^{n-1}\gamma_{2j}\gamma_{2j+1} \tag{2.32}$$

corresponding to pairing of Majoranas from neighbouring electron sites, the so-called *topologically nontrivial*[6] phase. Importantly, the first and the last Majorana operator of

[6] The term 'topologically nontrivial' is commonly abbreviated as 'topological' while 'topologically trivial' simply as 'trivial'.

the chain dropped out from the Hamiltonian. To see the implications of this, one defines new operators

$$\tilde{a}_0 = \tfrac{1}{2}(\gamma_1 + \mathrm{i}\gamma_n) \tag{2.33}$$

$$\tilde{a}_0^\dagger = \tfrac{1}{2}(\gamma_1 - \mathrm{i}\gamma_n) \tag{2.34}$$

constructed from the unpaired Majorana operators missing from Equation (2.32). Operators $\tilde{a}_0$ and $\tilde{a}_0^\dagger$ commute with the Hamiltonian and represent a *nonlocal* fermion bound to the ends of the chain. However, since they do not appear in the Hamiltonian, occupying the corresponding mode requires *zero energy*. Starting with ground state $|0\rangle$ with zero occupation satisfying $\tilde{a}_0|0\rangle = 0$, one can write

$$\tilde{a}_0^\dagger|0\rangle = |1\rangle \tag{2.35}$$

$$\langle 0|H|0\rangle = \langle 1|H|1\rangle\,. \tag{2.36}$$

The states $|0\rangle$ and $|1\rangle$ have the same energy but differ in the occupation of the nonlocal end mode. However, both ground states are identical in the bulk which is described by rewriting Equation (2.32) using new fermion operators

$$\tilde{a}_j = \tfrac{1}{2}(\gamma_{2j} + \mathrm{i}\gamma_{2j+1}) \tag{2.37}$$

$$\tilde{a}_j^\dagger = \tfrac{1}{2}(\gamma_{2j} - \mathrm{i}\gamma_{2j+1}), \tag{2.38}$$

that combine Majorana operators from neighbouring sites. The bulk Hamiltonian

$$H = 2t\sum_{j=1}^{n-1}\left(\tilde{a}_j^\dagger\tilde{a}_j - \tfrac{1}{2}\right) \tag{2.39}$$

now represents a chain with $n-1$ electron sites due to the missing nonlocal end mode, and have an excitation energy of $2t$. Remarkably, in contrast to conventional (trivial) superconductors with a nondegenerate ground state consisting of a superposition of even number of particles (condensate of Cooper pairs) and a gapped excitation spectrum, topological phase of the Kitaev chain allows for a zero-energy excitation supporting a twofold degenerate ground state. These ground states $|0\rangle$ and $|1\rangle$ differ in parity[7] of the zero-energy fermion determined by the operator

$$P = 1 - 2\tilde{a}_0^\dagger\tilde{a}_0 = -\mathrm{i}\gamma_1\gamma_n, \tag{2.40}$$

whereas the rest of the excitations are gapped out.

The derivation above holds for the special case $t = \Delta \neq 0$ and $\mu = 0$. However one can show that the unpaired Majoranas remain as long as $2t > |\mu|$ and $\Delta \neq 0$ assuming an infinite chain. For a finite chain Majorana end modes couple introducing an extra interaction term

$$H_{\mathrm{in}} = \mathrm{i}\frac{t_0}{2}\gamma_1\gamma_n \tag{2.41}$$

[7] Note that while the number of electrons is not a well-defined quantity in superconductors, fermion parity—the evenness or oddness of the number of electrons—is preserved.

to the Hamiltonian. While this interaction term results in an energy difference t_0 between $|0\rangle$ and $|1\rangle$, it vanishes exponentially with the length of the chain:

$$t_0 \propto e^{-L/\xi}, \quad \xi = \hbar v_F/\Delta \tag{2.42}$$

with L the chain length, ξ the Majorana localization length, v_F the Fermi velocity and Δ the superconducting gap. Due to this exponential relation, as long as Majoranas are far apart ($L \gg \xi$), the ground state degeneracy remains.

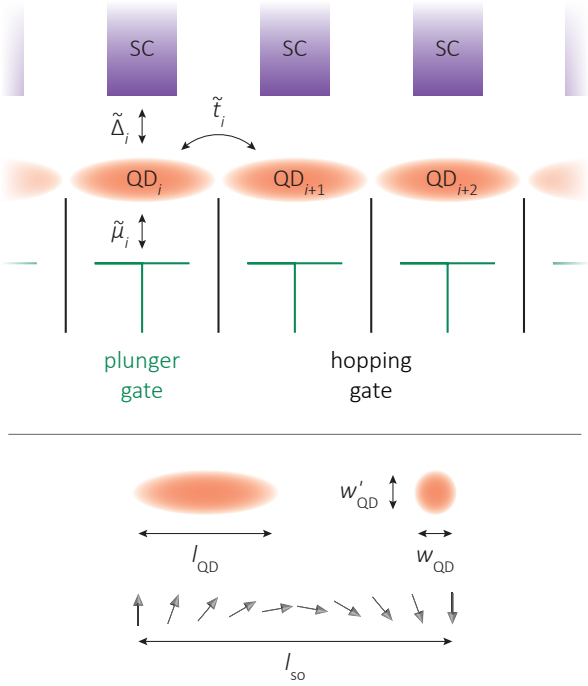

Figure 2.7 | A linear quantum dot array effectively representing the Kitaev chain. Orange ellipses depict the quantum dots (QD) with index i, each coupled to a superconductor (SC) shown in purple rectangles. The chemical potential in each dot $\tilde{\mu}_i$ is controlled by an individual plunger gate. The hopping parameter $\tilde{t}_i$ is controlled by the hopping gates. The dimensions of the quantum dot are given by the dot length l_{QD}, the dot width w_{QD}, and the dot depth w'_{QD}. For a spin–orbit length $l_{so} \gg w_{QD}, w'_{QD}$ the direction of the spin–orbit field is independent of the dot index i [24]. In this case, the external magnetic field can be oriented perpendicular the spin–orbit field for the entire length of the array, which simplifies tuning the system into the topological phase [24]. Further simplification in tuning is achieved for a dot length $l_{QD} \lesssim l_{so}$ [24].

Realizing a Kitaev chain using quantum dots. Although the Kitaev chain is unphysical due to the assumption of spinless electrons, it can nevertheless be represented by a realistic system based on a linear quantum dot array [23, 24], shown in Figure 2.7. Each quantum dot QD_i is coupled to a superconducting electrode SC which induces pairing $\tilde{\Delta}_i$. The geometric confinement separates the energies of the quantum dot levels which correspond to the states with different electron occupation. For a sufficiently strong confinement, the level spacing becomes the largest energy term in the Hamiltonian, and

all other levels can be neglected besides the one close to the Fermi level. The spinless regime can be effectively reached by an external magnetic field, which Zeeman-splits the otherwise doubly spin-degenerate quantum dot levels. To allow for superconducting pairing between the neighbouring dots with the same spin polarization, one requires spin–orbit coupling which rotates the spin polarization of the left end of the dot with respect to the right end. Reaching the topological regime requires the chemical potential of the dots to be $\tilde{\mu}_i^2 = \epsilon_z^2 - \tilde{\Delta}_i^2$, with ϵ_z the Zeeman energy. This is analogous to taking $\mu = 0$ for the Kitaev chain in Equation (2.32). Finally, when the hopping parameter is set to be $\tilde{t}_i \ll \epsilon_z$, the Hamiltonian of the linear quantum dot array can be mapped to that of the Kitaev chain [24].

2.6. Properties of Majoranas

Here we introduce the properties of Majoranas which are interesting both for fundamental physics and for practical applications. Importantly, we will see that when exchanged Majoranas behave differently than all elementary particles, and that this unique property can be used to build a quantum computer.

We have introduced in the previous section that two unpaired Majoranas can describe a nonlocal fermion mode with zero-energy in a topological superconductor giving rise to a degenerate ground state with a gapped excitation spectrum. One can show that Majorana operators are Hermitian $\gamma_i = \gamma_i^\dagger$ using Equations (2.29) and (2.30). They satisfy the anticommutation relation

$$\{\gamma_i \gamma_j\} = \gamma_i \gamma_j + \gamma_j \gamma_i = 2\delta_{ij} \tag{2.43}$$

derived from the fermion anticommutation rules. From these relations it follows that a single Majorana mode does not represent a number state, and the number operator n_M associated with a single Majorana is an identity operator without any physical meaning $n_\mathrm{M} = \gamma_i^\dagger \gamma_i = 1$. Instead, an occupation is described by a fermion combining a pair of Majoranas as demonstrated in the previous section. Using a fermion operator a_i constructed from two spatially separated Majoranas $a_i = \frac{1}{2}(\gamma_{2i-1} + \mathrm{i}\gamma_{2i})$, the number operator is expressed by

$$n_i = a_i^\dagger a_i = \tfrac{1}{2}(1 + \mathrm{i}\gamma_{2i-1}\gamma_{2i}). \tag{2.44}$$

We will now introduce the ground state degeneracy associated with the presence of Majorana modes. For a superconducting system with $2N$ spatially separated Majoranas, one can construct N nonlocal zero-energy fermions a_i. Each zero-energy fermion allows an occupation of 0 or 1 given by the number operator n_i leading to a 2^{N-1}-fold degenerate ground state.[8] All ground states have the same total parity

$$P = \prod_i^N (1 - 2n_i) = (-\mathrm{i})^N \gamma_1 \gamma_2 \ldots \gamma_{2N}, \tag{2.45}$$

[8] Conservation of parity reduces the ground state degeneracy from 2^N to 2^{N-1} because only half of the states belong to the same parity subspace. This can be easily understood for $N = 1$: The occupation of the zero-energy fermion cannot change without a transfer of external charge to the superconductor.

a quantity which is preserved in superconductors, but differ in the occupation of the nonlocal zero-energy fermions n_i. Importantly, the occupation of the nonlocal fermions can only be measured by letting the constituting Majoranas interact to form a *local* fermion. As a crucial consequence, the quantum state of a system supporting noninteracting Majorana modes is *topologically protected* against (parity-preserving) local disturbances, demonstrating Majoranas' potential in quantum computing.

We now turn our attention to the nonlocal fermion occupation n_i which defines the quantum state of a topological superconductor. We mentioned above that n_i is measurable only by letting the spatially separated Majoranas interact which removes the degeneracy of the states with different occupation of the nonlocal fermions. n_i can be inferred from the interaction energy E_i via

$$E_i = t_i \left(n_i - \tfrac{1}{2}\right), \tag{2.46}$$

where we used Equations (2.41) and (2.44). This energy corresponds to the nonzero energy cost to occupy the fermion mode described by a_i which represents a local mode for interacting Majoranas. The interaction is set by the term t describing the tunnel coupling between Majoranas (see Equation (2.42)). Tunnel coupling can be switched on in many ways, for example, by bringing Majoranas together, by tuning the superconducting gap, or by changing the conductance of the section bridging two Majoranas. Finally, when the superconductor hosting Majoranas is small, the charging energy of the system removes the degeneracy of the different parity states even for a vanishing tunnel coupling by converting parity states into charge states [25]. In this case the coupling term is proportional to [14]

$$t \propto \left(E_J^3 E_C\right)^{1/4} e^{-\sqrt{8E_J/E_C}} \cos(\pi q/e), \tag{2.47}$$

with E_C the charging energy, E_J the Josephson energy, and q the offset charge. Notably, the coupling between Majoranas vanishes exponentially as $\sqrt{E_J/E_C}$ increases so that the ground state degeneracy remains for $\sqrt{E_J/E_C} \gg 1$. This coupling mechanism, the so-called Coulomb coupling, forms the basis of many current proposals to realize quantum information processing using Majoranas [26–31].

A measurement of the interaction energy E (or its sign) allows for a readout of the parity $P = (1-2n) = -\mathrm{i}\gamma_i\gamma_j = \pm 1$. Such a measurement can be performed in many ways. For example, in a Josephson junction with two topological superconducting wires, the phase dependence of the Josephson current is related to the interaction energy between the coupled Majoranas at each side of the junction [32]. Other recent proposals make use of a superconducting quantum bit (a transmon qubit) embedded in a transmission line resonator where the interaction energy is revealed via microwave spectroscopy [27, 33]. Conductance measurements are also proposed for detecting the interaction energy through interferometry [29, 30]. Further, a quantum dot tunnel-coupled to a topological superconductor experiences a parity-dependent energy shift which can then be measured by various means [31]. As a final example, one can use a charge sensor capacitively coupled to a topological superconductor to readout the interaction energy [28].

We will now proceed with introducing the *non-Abelian* exchange statistics of Majoranas, different from all elementary particles which obey either Fermi–Dirac or Bose–Einstein statistics. This non-Abelian property of Majoranas directly follows from the

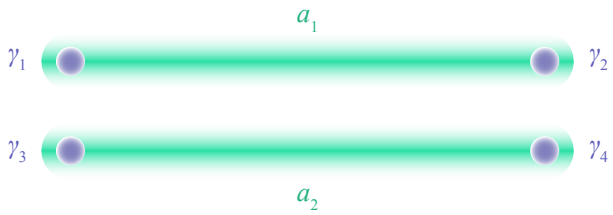

Figure 2.8 | A topological superconductor with four Majoranas. The four Majorana modes $\gamma_1 \ldots \gamma_4$ are depicted as violet spheres. γ_1 and γ_2 form the nonlocal fermion a_1, γ_3 and γ_4 the nonlocal fermion a_2.

ground state degeneracy of a topological superconductor [21] and allows for protected manipulations of quantum information as we will see below. To demonstrate the non-Abelian exchange statistics, we will sequentially exchange Majorana modes in different orders, and show that the order of exchange indeed determines the resulting state [34, 35]. First we introduce the braid operator which represents the exchange of Majorana γ_i and γ_{i+1}

$$B_{i,i+1} = e^{\pm\frac{\pi}{4}\gamma_i\gamma_{i+1}} = \frac{1}{\sqrt{2}}\left(1 \pm \gamma_i\gamma_{i+1}\right), \quad \gamma_i\gamma_{i+1} = \mathrm{i}P \tag{2.48}$$

where $\pm$ distinguishes between clockwise and counter-clockwise exchange[9] and P denotes the parity operator of the fermion formed by γ_i and γ_{i+1} (see Equation (2.40)).[10] We consider a doubly degenerate ground state with four Majoranas γ_{1-4}, shown in Figure 2.8. $\gamma_{1,2}$ form the nonlocal fermion a_1, and $\gamma_{3,4}$ the nonlocal fermion a_2:

$$a_1 = \tfrac{1}{2}\left(\gamma_1 + \mathrm{i}\gamma_2\right) \tag{2.49}$$

$$a_2 = \tfrac{1}{2}\left(\gamma_3 + \mathrm{i}\gamma_4\right) \tag{2.50}$$

We specify the states $|n_1, n_2\rangle$ by the occupation of fermion a_1 and a_2. Applying the exchange sequences $B_{23}B_{12}$ and $B_{12}B_{23}$ for example on $|00\rangle$ produces different results

$$B_{23}B_{12}\,|00\rangle = \frac{1+\mathrm{i}}{2}\left(|00\rangle + \mathrm{i}|11\rangle\right) \tag{2.51}$$

$$B_{12}B_{23}\,|00\rangle = \frac{1+\mathrm{i}}{2}\left(|00\rangle + |11\rangle\right) \tag{2.52}$$

demonstrating the non-Abelian exchange statistics of Majoranas. Non-Abelian property follows from the fact that two exchanges involving the same Majorana mode do not commute.[11]

A braid operation can be realized in a wire-based system by physically moving Majorana modes using electrostatic gates [32]. Alternative proposals to implement braiding

[9] Exchanging two Majoranas is equivalent to moving a Majorana around the other to complete half a revolution. This explains the degree of freedom due to clockwise and counter-clockwise exchange.

[10] Here we used $e^{\mathrm{i}\alpha A} = \cos(\alpha) + \mathrm{i}A\sin(\alpha)$ for an operator A with $A^2 = 1$. Parity operator P satisfies this condition. In matrix representation the equation becomes $e^{\mathrm{i}\alpha A} = \cos(\alpha)I + \mathrm{i}\sin(\alpha)A$, with I the identity matrix.

[11] Mathematically: $B_{12}B_{23} \neq B_{23}B_{12}$ or $\gamma_1\gamma_2\gamma_2\gamma_3 = \gamma_1\gamma_3 \neq \gamma_2\gamma_3\gamma_1\gamma_2 = -\gamma_3\gamma_2\gamma_1\gamma_2 = \gamma_3\gamma_2\gamma_2\gamma_1 = \gamma_3\gamma_1$.

in wires rely on adiabatically changing the coupling between Majoranas without physically moving them [36]. Here, the coupling between different Majoranas are switched on and off in a particular order which effectively exchanges two Majoranas. This coupling can be of tunnel origin [37] or of Coulomb origin [26–28, 33] with the latter forming the basis of current experimental efforts to realize topological quantum computation using Majoranas at the time of writing.

We will conclude this section by introducing a Majorana quantum bit (qubit), a two-state quantum-mechanical system allowing for information processing using Majoranas. The qubit is represented by a doubly-degenerate ground state of a topological superconductor with four Majorana modes, the same system we considered above to demonstrate the non-Abelian exchange statistics of Majoranas (see Figure 2.8, and Equations (2.49) and (2.50)). The two states of the qubit $|n_1, n_2\rangle$ can then be given for example by $|00\rangle$ and $|11\rangle$ in the even parity subspace.[12] An arbitrary state has the form

$$|\psi\rangle = c_0\,|00\rangle + c_1\,|11\rangle\,, \quad |\psi\rangle \equiv \begin{pmatrix} c_0 \\ c_1 \end{pmatrix}, \quad |c_0|^2 + |c_1|^2 = 1. \tag{2.53}$$

Importantly, the products of Majorana operators can be expressed using Pauli matrices[13]

$$\sigma_x = -\mathrm{i}\gamma_1\gamma_4 = -\mathrm{i}\gamma_2\gamma_3 \tag{2.54}$$

$$\sigma_y = -\mathrm{i}\gamma_1\gamma_3 = -\mathrm{i}\gamma_4\gamma_2 \tag{2.55}$$

$$\sigma_z = -\mathrm{i}\gamma_1\gamma_2 = -\mathrm{i}\gamma_3\gamma_4. \tag{2.56}$$

Here we remind the reader that in Bloch sphere representation[14] with $|00\rangle \equiv |0\rangle$ and $|11\rangle \equiv |1\rangle$, the exponential of a Pauli matrix σ_i corresponds to the rotation operator $R_i(\theta)$ which rotates a qubit state by an angle θ around axis n

$$R_n(\theta) = e^{\mathrm{i}\frac{\theta}{2}\sigma_n} \quad n = x, y, z. \tag{2.57}$$

Using Equations (2.48) and (2.54) – (2.57) we find that braid operations correspond to qubit rotations by a quantized angle $\pi/2$: $R_n(\pi/2) = B_{ij}$. This quantized angle indicates the topological error-protection of the qubit rotations for vanishing coupling between Majoranas. We note that while performing universal quantum computation requires constructing arbitrary unitary operations which is not possible using only $\pi/2$-rotations, universality can be obtained by supplementing braid operations with only a few nontopological operations [38–40]. Finally, because topological operations necessitate much less error correction,[15] a Majorana-based topological quantum computer can be realized using less qubits and operations compared to conventional platforms for quantum computation [42].

[12] The other possible qubit states $|01\rangle$ and $|10\rangle$ are in the odd parity subspace. Starting with even parity, odd parity subspace is not accessible by Majorana exchange (braid) operations which preserve the parity.

[13] Note that $a_1^\dagger a_2^\dagger|00\rangle = -a_2^\dagger a_1^\dagger|00\rangle = |11\rangle$ and $-a_1 a_2\,|11\rangle = a_2 a_1\,|11\rangle = |00\rangle$ which follows from the definition of fermion creation and annihilation operators satisfying anticommutation relations.

[14] An arbitrary qubit state $|\psi\rangle = e^{\mathrm{i}\alpha}(\cos(\theta/2)\,|0\rangle + e^{\mathrm{i}\phi}\sin(\theta/2)\,|1\rangle)$ can be geometrically represented on the surface of a three dimensional sphere with unit radius, the so-called Bloch sphere. Bloch sphere representation neglects the global phase ($\alpha = 0$). The basis vectors $|0\rangle$ and $|1\rangle$ correspond to the north and the south pole of the Bloch sphere, respectively.

[15] Due to the probabilistic nature of quantum mechanics, a quantum computer must include error correction which can be implemented using overhead both on the software and on the hardware level [41].

2.7. Majoranas in semiconductor nanowires

Here we introduce how Majoranas can be realized starting with a semiconductor nanowire. We will also see how Majoranas respond to various experimental parameters.

In the previous section we have seen how Majoranas appear in a one-dimensional p-wave superconductor, in particular, in a spinless chain with superconducting pairing. While there are no established superconductors with p-wave pairing at the time of writing,[16] such exotic modes can nevertheless be realized with conventional superconductors using various condensed matter platforms such as graphene [45], topological insulators [46–48], atomic chains [49], two-dimensional electron gases [50, 51], and semiconductor nanowires [52–54].[17] In the following, we will focus on the latter and show that a semiconductor nanowire with spin–orbit coupling supports a topological superconducting phase with p-wave pairing when combined with an s-wave superconductor in an external magnetic field.

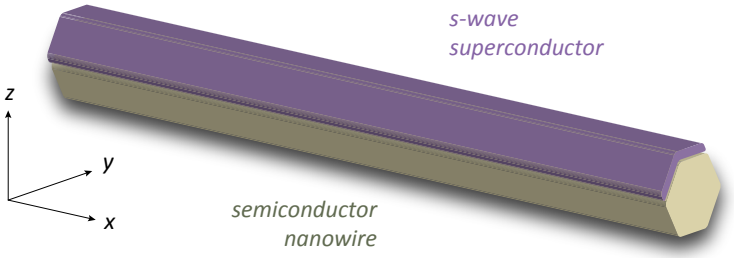

Figure 2.9 | A Majorana nanowire. A semiconductor nanowire with spin–orbit coupling (beige) is proximity-coupled to an s-wave superconductor (purple) which covers the two facets of the nanowire. The nanowire axis is along x. The spin–orbit field is assumed to be along y.

Figure 2.9 shows a semiconductor nanowire proximity-coupled to an s-wave superconductor. To describe such a proximitized wire with spin–orbit coupling in the presence of a magnetic field we will use [57, 58]

$$H = \int dy \Psi^\dagger H_{\mathrm{BdG}} \Psi, \quad \Psi^\dagger = (\psi_\uparrow^\dagger, \psi_\downarrow^\dagger, \psi_\downarrow, -\psi_\uparrow). \tag{2.58}$$

H_{BdG} denotes the Bogoliubov–de Gennes Hamiltonian, Ψ is the so-called Nambu spinor including electron operators. In contrast to Equation (2.7) where the superconducting pairing was limited to s-wave, here we use both spin projections for electron creation and annihilation operators requiring a four-component notation. In this Nambu basis H_{BdG} is a 4×4 matrix which can be written as

$$H_{\mathrm{BdG}} = \left(\frac{\mathbf{p}^2}{2m^*} - \mu \right) (\tau_z \otimes I) + \frac{\alpha_{\mathrm{R}}}{\hbar} \mathbf{p} (\tau_z \otimes \sigma_y) + \frac{g}{2} \mu_{\mathrm{B}} B_x (I \otimes \sigma_x) + \Delta (\tau_x \otimes I), \tag{2.59}$$

[16] Important p-wave candidates are Sr_2RuO_4 [43] and $Cu_xBi_2Se_3$ [44].

[17] We note that Majorana modes can also be realized in fractional quantum Hall systems, but without the need of superconductivity [55, 56].

with Pauli matrices τ and σ acting on particle-hole and spin degree of freedom, respectively, and I the identity matrix (compare with Equation (2.8)). H_{BdG} consists of four terms: (1) kinetic energy term with the momentum operator $\mathbf{p}$ and the chemical potential μ; (2) spin–orbit term with the coupling strength α_{R}; (3) Zeeman term with Landé g factor, Bohr magneton μ_{B}, and magnetic field B_x; (4) the superconductivity term with the induced pairing potential Δ (taken real). x is the wire axis and y is the direction of the spin–orbit field. The magnetic field is oriented along the wire (perpendicular to the spin–orbit field). We assume single mode occupation in the wire, Rashba type spin–orbit coupling, and that the magnetic field enters the Hamiltonian only as a Zeeman term. The excitation spectrum is then given by[18]

$$E_{\pm} = \left(\epsilon^2 + \epsilon_{so}^2 + \epsilon_z^2 + \Delta^2 \pm 2\sqrt{\epsilon^2(\epsilon_{so}^2 + \epsilon_z^2) + \epsilon_z^2\Delta^2}\right)^{1/2}, \tag{2.60}$$

$$\epsilon = \hbar^2 k^2/2m^* - \mu, \quad \epsilon_{so} = \alpha_{\mathrm{R}} k, \quad \epsilon_z = \tfrac{1}{2} g \mu_{\mathrm{B}} B_x. \tag{2.61}$$

In the following, to see how each term contributes to the excitation spectrum, we will add them one-by-one and finally drive the system into topological superconducting phase by including all necessary ingredients.

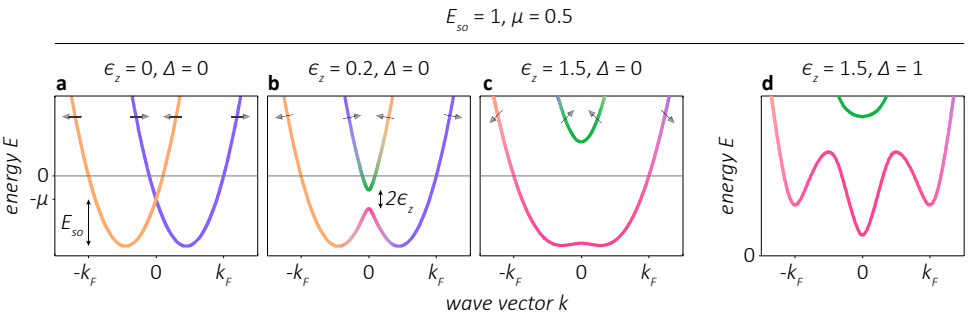

Figure 2.10 | Topological phase transition by introducing superconductivity as the final ingredient. a, Dispersion relation in a semiconductor nanowire with spin–orbit coupling ($m^*\alpha_{\mathrm{R}}^2/2\hbar^2 = E_{so} > 0$) at zero magnetic field ($\epsilon_z = 0$). Spin–orbit coupling splits the otherwise spin-degenerate parabolic bands by shifting each by $\pm k_{so}$ ($k_{so} = m^*\alpha_{\mathrm{R}}/\hbar^2$) in k-axis, and further lowers them by $E_{so} = m^*\alpha_{\mathrm{R}}^2/2\hbar^2$ in energy axis. The arrows represent the orientation of the electron spin for the given subband. **b,** An applied magnetic field introduces a Zeeman energy $\epsilon_z = 0.2$, and opens up an energy gap of $2\epsilon_z$ at $k = 0$. The spin orientation now evolves smoothly in energy, indicated with different colors: orange (←) and violet (→) indicate orientation along spin–orbit field, green (↑) and magenta (↓) along external magnetic field. **c,** Increasing ϵ_z increases the Zeeman energy gap and polarizes the spins more along the external magnetic field. For $\epsilon_z = 1.5$, Fermi level falls within the Zeeman gap and the nanowire is in the helical state. **d,** Introducing superconducting pairing in a helical wire results in topological superconductivity with inverted bands. E_{so}, μ, ϵ_z, and Δ are given in units of meV. The effective mass is taken to be $m^* = m_{\mathrm{InSb}} = 0.013 m_e$.

We start with a semiconducting nanowire with Rashba spin–orbit coupling at zero magnetic field without induced pairing ($\epsilon_z = \Delta = 0 < \alpha_{\mathrm{R}}$), shown in Figure 2.10a. Re-

[18] Note that one recovers Equation (2.9) for vanishing spin–orbit and magnetic field.

stricting ourselves to the particle subspace,[19] the energy eigenvalues are given as

$$E_{\pm} = \epsilon \pm \epsilon_{so} = \hbar^2 k^2 / 2m^* - \mu \pm \alpha_{\mathrm{R}} k. \tag{2.62}$$

Spin–orbit coupling splits the otherwise spin-degenerate parabolic bands in k-axis and results in a momentum-dependent effective magnetic field. Despite this effective magnetic field, the transport is maintained by two electronic subbands with opposite spins where the spin degree of freedom cannot be neglected: For each forward-moving electron with an energy E and a certain orientation of spin, there is a second forward-moving electron with the same energy but opposite spin. However, inducing p-wave superconductivity requires single subband occupation where the electrons with parallel spin components are paired. To reach this spinless regime, one introduces an external magnetic field perpendicular to spin–orbit field giving rise to the dispersion

$$E_{\pm} = \epsilon \pm \sqrt{\epsilon_{so}^2 + \epsilon_z^2} = \hbar^2 k^2 / 2m^* - \mu \pm \sqrt{\alpha_{\mathrm{R}}^2 k^2 + \left(\tfrac{1}{2} g \mu_{\mathrm{B}} B_x\right)^2}, \tag{2.63}$$

shown in Figure 2.10b. External magnetic field B_x splits the subbands in energy axis and tilts the spins of electrons towards the quantization axis, affecting the spectrum stronger for small k where ϵ_{so} is small. At $k = 0$ for which the spin–orbit coupling has no contribution to the dispersion, the external magnetic field opens up an energy gap of $2\epsilon_z$, the so-called helical gap where the electron spin orientation is locked to the direction of momentum. Importantly, when the Fermi level falls within the helical gap ($|\mu| < |\epsilon_z|$), the transport is maintained by a single spin-subband which provides pairs of electrons with opposite momenta but parallel spin component (Figure 2.10c), the prerequisite of p-wave superconductivity. Indeed, inducing s-wave pairing in a helical wire results in topological superconductivity with an inverted excitation gap for $\mu^2 < \epsilon_z^2 - \Delta^2$, shown in Figure 2.10d. Below we demonstrate the evolution of the excitation gap as a function of magnetic field which clearly shows the inversion of the bands.

In our consideration above, we introduced pairing as the final ingredient to obtain topological superconductivity. While it is insightful to do so, experimentally it is more common to introduce the Zeeman energy (magnetic field) or to change the chemical potential (carrier density) to drive the system into the topological phase. In the following we start from a semiconducting nanowire with spin–orbit coupling and induced pairing Δ at zero magnetic field. Next, we gradually increase Zeeman energy ϵ_z which first closes and then reopens the excitation gap at $k = 0$ resulting in a topological phase with inverted bands.

Figure 2.11a shows that superconductivity opens a gap Δ in the excitation spectrum leading to two energy minima for zero magnetic field: one at Fermi wave vector k_F denoted by Δ_F and the other at a smaller k.[20] Although not an energy minimum for $\mu \neq 0$, another essential point in the dispersion is $k = 0$ where the excitation gap is given by Δ_0.[21] Together with Δ_F, Δ_0 dictates the topology of the system. Introducing a small Zeeman energy tilts the spins of electrons towards the quantization axis and splits the bands,

[19] For no superconducting pairing, the Hamiltonian can be written considering only the particle subspace: $H = \left(\frac{\mathbf{p}^2}{2m^*} - \mu\right) I + \frac{\alpha_{\mathrm{R}}}{\hbar} \mathbf{p} \sigma_y + \frac{g}{2} \mu_{\mathrm{B}} B_x \sigma_x$.

[20] For chemical potential $\mu = 0$, the position of the latter minima shifts to $k = 0$.

[21] For $\epsilon_z = 0$, the gap values are $\Delta = \Delta_F \leq \Delta_0$. For $\epsilon_z = \mu = 0$, the gap values become $\Delta = \Delta_F = \Delta_0$.

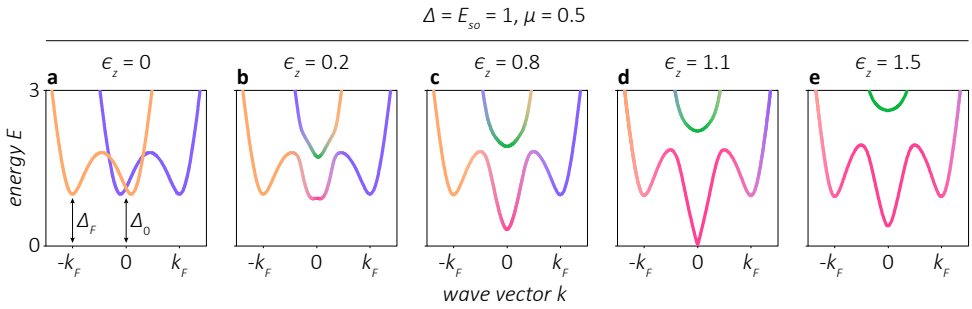

Figure 2.11 | Topological phase transition driven by an external magnetic field. **a,** Dispersion relation in a semiconductor nanowire with induced pairing $\Delta = 1$ and spin–orbit coupling ($E_{so} = 1$) at zero magnetic field ($\epsilon_z = 0$). Superconductivity opens a gap Δ in the excitation spectrum. **b,** An applied magnetic field introduces a Zeeman energy $\epsilon_z = 0.2$, and splits the bands at $k = 0$. The spin orientation evolves smoothly in energy, indicated with different colors: orange (←) and violet (→) indicate orientation along spin–orbit field, green (↑) and magenta (↓) along external magnetic field. **c,** Increasing ϵ_z decreases Δ_0. **d,** For $\epsilon_z^2 = \Delta^2 + \mu^2$, Δ_0 closes. **e,** Further increase of ϵ_z reopens Δ_0 driving the system into the topological phase. All energies are given in units of meV. The effective mass is taken to be $m^* = m_{\mathrm{InSb}} = 0.013 m_e$.

shown in (Figure 2.11b and c). At the degeneracy point $k = 0$, the upper spin-subband is lifted to higher energies while the lower spin-subband is pushed down. This decreases Δ_0 which is given by

$$\Delta_0 = \left| \sqrt{\Delta^2 + \mu^2} - \epsilon_z \right|. \tag{2.64}$$

Further increase of Zeeman energy closes the gap Δ_0 at $\epsilon_z' = \sqrt{\Delta^2 + \mu^2}$, the critical Zeeman energy for which the system undergoes topological phase transition (see Figure 2.11d). For $\epsilon_z > \epsilon_z'$ the gap Δ_0 reopens signifying the topological phase with inverted bands (see Figure 2.11e). In this phase, Zeeman energy continuously increases Δ_0 while further aligning the spins of electrons at opposite momenta, whose pairing is now of p-wave type. Indeed, for $\epsilon_z \gg E_{so} = \alpha_{\mathrm{R}}^2 m^* / 2\hbar^2$, with E_{so} the spin–orbit energy constant, one can neglect the upper spin-subband at higher energies and simplify the system to a spinless p-wave superconductor with an effective gap $|\Delta_p| = \alpha_{\mathrm{R}} \Delta / \hbar \epsilon_z$ supporting Majoranas at its ends [32]. While this simplification is valid only for large magnetic fields, as long as the bulk excitation gap does not close, Majorana modes remain at the ends of the wire since their presence is linked to the topology of the bands. Below we show that the bulk excitation gap indeed remains finite for a wide range of parameters demonstrating the robustness of Majorana modes.[22]

The bulk excitation gap in the topological regime is determined by Δ_F away from the phase transition where $\Delta_F < \Delta_0$. Δ_F has only a weak dependence on μ which can be neglected.[23] We now turn to the dependence of Δ_F on Zeeman energy ϵ_z and the spin–

[22] Note that the evolution of Δ_0 for varying ϵ_z and μ does *not* depend on spin–orbit coupling. For example, increasing ϵ_z closes and reopens Δ_0 according to Equation (2.64) even for $E_{so} = 0$. However, for small E_{so} the excitation gap is limited by Δ_F away from the phase transition, which vanishes quickly with increasing ϵ_z (see Equation (2.65)). For $E_{so} = 0$, Δ_0 and Δ_F close at the same time, but Δ_F does not reopen, demonstrating the necessity of spin–orbit coupling for obtaining topological superconductivity.

[23] Δ_F increases monotonically for increasing μ.

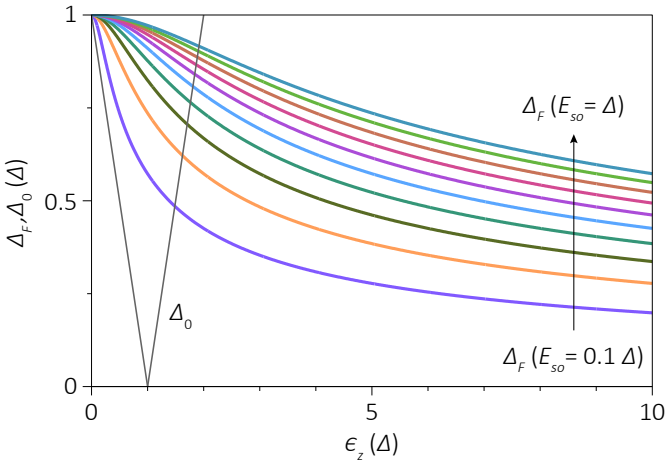

Figure 2.12 | Evolution of Δ_F and Δ_0 in an external magnetic field for $\mu = 0$. Gray thin curve represents $\Delta_0 = |\Delta - \epsilon_z|$. Colored thick curves represent Δ_F for varying E_{so} $(0.1 \ldots 1\Delta)$. At zero magnetic field ($\epsilon_z = 0$), $\Delta_F = \Delta_0 = \Delta$. Increasing ϵ_z decreases Δ_F only slowly. Increasing E_{so} increases Δ_F protecting it from closing in an external magnetic field. For $E_{so} = 0$, Δ_0 and Δ_F close at the same time, but Δ_F does not reopen.

orbit energy constant E_{so}. While the exact expression of Δ_F is complicated,[24] taking $\mu = 0$ it can be written in an approximate form [59]

$$\Delta_F \approx \Delta \left(\frac{4E_{so}}{2E_{so} + \sqrt{4E_{so}^2 + \epsilon_z^2}} \right)^{1/2} \tag{2.65}$$

valid for finite E_{so}. Figure 2.12 shows that a larger E_{so} results in a larger Δ_F protecting the topological phase. Importantly, Δ_F remains finite for finite magnetic fields and for all μ indicating the robustness of the topological phase.

2.8. Experimental detection of Majoranas

Here we introduce how one can experimentally detect Majoranas in a semiconductor nanowire device using tunneling spectroscopy.

In the previous section we have seen that a topological superconducting wire hosts a pair of separated Majoranas bound to its ends forming a nonlocal fermion. The presence of this nonlocal fermion allows a topological superconductor to have a zero-energy excitation for large ranges of chemical potential (carrier density) and magnetic field, a unique property distinguishing topological superconductors from trivial ones. In the following we will see that this zero-energy excitation is expected to give rise to resonant Andreev reflection, another distinctive feature of Majoranas.

[24] Note that Δ_F is not located exactly at k_F for finite Zeeman energies.

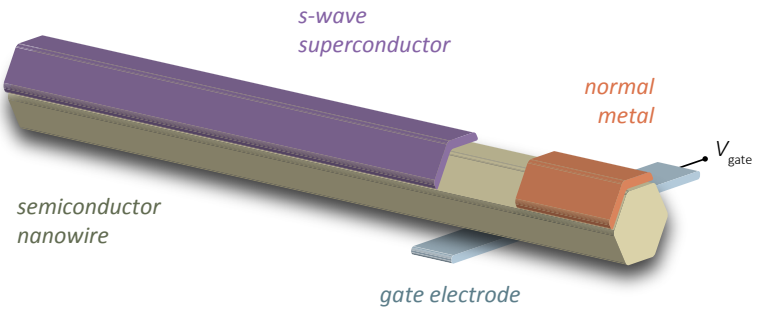

Figure 2.13 | Tunneling spectroscopy. A semiconductor nanowire with spin–orbit coupling (beige) is contacted by an s-wave superconductor (purple) which induces pairing in the wire. The extended wire section is contacted by a normal metal (orange) leaving a noncovered wire section between both contacts. The noncovered wire section is capacitively coupled to a gate electrode which, for negative gate voltages, depletes the section between the contacts forming an electrostatically defined tunnel barrier. The conductance through the nanowire measured using both contacts resolves the quasiparticle (excitation) density of states in the proximitized nanowire.

The excitation spectrum of a superconductor can be measured via tunneling spectroscopy, a technique many experiments have relied on to obtain characteristic Majorana signatures in various materials systems [47, 49, 52]. In tunneling spectroscopy one sends a current to the superconductor through a tunnel barrier where the resulting conductance reflects the density of excitation states (see Figure 2.13). The presence of Majoranas is detected as a zero-energy state in the otherwise gapped excitation spectrum. Importantly, this Majorana state leads to resonant Andreev reflection with unit transmission probability resulting in a $2e^2/h$ conductance peak at zero energy independent of the tunnel barrier strength [60]. To see this we will describe the transport between a normal conductor and a grounded superconductor using the reflection matrix r

$$\begin{pmatrix} \varphi_e^o \\ \varphi_h^o \end{pmatrix} = r \begin{pmatrix} \varphi_e^i \\ \varphi_h^i \end{pmatrix} \quad \text{with} \quad r = \begin{pmatrix} r_{ee} & r_{eh} \\ r_{he} & r_{hh} \end{pmatrix}. \tag{2.66}$$

φ denotes the amplitude of $i$ncoming or $o$utgoing waves (see superscript) corresponding to $e$lectrons or $h$oles (see subscript) in the normal conductor. For N occupied subbands, r is a $2N \times 2N$ matrix with its all 4 elements being $N \times N$ matrices. For a single subband without spin degeneracy ($N = 1$), the elements of r correspond to the probabilities of normal and Andreev reflection for incoming electrons similar to Equations (2.14) and (2.18)

$$|r_{ee}|^2 = |r_N|^2 \tag{2.67}$$
$$|r_{he}|^2 = |r_A|^2. \tag{2.68}$$

Here r_{ee} is the probability of incoming electron to be reflected as an electron (normal reflection), and r_{he} the probability of incoming electron to be reflected as a hole (Andreev reflection). We have seen in Section 2.3 that in a superconductor propagation of waves is not allowed for subgap energies. This implies incoming waves can either scatter back

or are Andreev reflected yielding

$$|r_{ee}|^2 + |r_{he}|^2 = 1 \tag{2.69}$$
$$|r_{eh}|^2 + |r_{hh}|^2 = 1, \tag{2.70}$$

equivalent to the unitarity of the reflection matrix r for subgap energies. The conductance for arbitrary number of subbands N is then given as

$$G = G_0 \mathrm{Tr}(r_{he} r_{he}^\dagger) \quad \text{with} \quad G_0 = \frac{2e^2}{h}, \tag{2.71}$$

which becomes $G = G_0 |r_{he}|^2$ for $N = 1$. For zero energy, particle-hole symmetry imposes the additional requirement $r_{ee} = r_{hh}^*$ and $r_{eh} = r_{he}^*$.[25] For $N = 1$ the reflection matrix r must become [61–63]

$$r_{\mathrm{triv}} = \pm \begin{pmatrix} e^{\mathrm{i}\phi_1} & 0 \\ 0 & e^{-\mathrm{i}\phi_1} \end{pmatrix} \quad \text{or} \quad r_{\mathrm{topo}} = \pm \begin{pmatrix} 0 & e^{\mathrm{i}\phi_2} \\ e^{-\mathrm{i}\phi_2} & 0 \end{pmatrix}. \tag{2.72}$$

Remarkably, for the reflection matrix of the form r_{triv} Andreev reflection probability is zero, whereas r_{topo} corresponds to unit Andreev reflection probability. This is related to $\det(r)$ signifying a topological quantum number [62, 64, 65] with $\det(r_{\mathrm{triv}}) = +1$ indicating the trivial phase, and $\det(r_{\mathrm{topo}}) = -1$ the topological phase. As a result, the topological phase with Majorana end modes is associated with a quantized conductance at zero energy.

References

[1] Onnes, H. K. *Nobel Lecture* (1913)

[2] Meissner, W. & Ochsenfeld, R. *Naturwissenschaften* **21**, 787 (1933)

[3] Landau, L. D. & Ginzburg, V. *Zh. Eksp. Teor. Fiz.* **20**, 1064 (1950)

[4] Gor'kov, L. P. *Sov. Phys. JETP* **36**, 1364 (1959)

[5] Tinkham, M. *Introduction to Superconductivity.* 2nd Edition. Dover Publications, Inc., New York (2004)

[6] Bardeen, J.; Cooper, L. N. & Schrieffer, J. R. *Phys. Rev.* **108**, 1175 (1957)

[7] Cooper, L. N. *Phys. Rev.* **104**, 1189 (1956)

[8] Van Duzer, T. & Turner, C. W. *Principles of Superconductive Devices and Circuits.* Edward Arnold, London (1981)

[9] Ibach, H. & Lüth, H. *Solid-State Physics: An Introduction to Principles of Material Science.* 4th Edition. Springer-Verlag, Berlin Heidelberg (2009)

[25] At zero energy particle hole symmetry requires $\tau_x r^* \tau_x = r$ with τ_x the Pauli matrix. Note that time-reversal and spin-rotation symmetries are not imposed due to external magnetic field and spin–orbit coupling, respectively. This is in contrast to the BTK approach introduced in Section 2.3 (see also refs. [13, 17]).

[10] Desai, B. R. *Quantum Mechanics with Basic Field Theory.* Cambridge University Press (2010)

[11] De Gennes, P.-G. *Superconductivity of Metals and Alloys.* Westview Press, Boulder, CO (1999)

[12] Datta, S.& Bagwell, P. F. *Superlattices Microstruct.* **25**, 1233 (1999)

[13] Blonder, G.; Tinkham, M. & Klapwijk, T. *Phys. Rev. B* **25**, 4515 (1982)

[14] Nazarov, Y. V. & Blanter, Y. M. *Quantum Transport: Introduction to Nanoscience.* Cambridge University Press (2009)

[15] Schäpers, T. *Superconductor/Semiconductor Junctions.* Springer-Verlag Berlin Heidelberg (2001)

[16] Andreev, A. F. *Sov. Phys. JETP* **19**, 1228 (1964)

[17] Beenakker, C. W. J. *Phys. Rev. B* **46**, 12841 (1992)

[18] Sigrist, M & Ueda, K. *Rev. Mod. Phys.* **63**, 239 (1991)

[19] Sigrist, M. *AIP Conf. Proc.* **789**, 165 (2005)

[20] Read, N & Green, D. *Phys. Rev. B* **61**, 10267 (2000)

[21] Ivanov, D. A. *Phys. Rev. Lett.* **86**, 268 (2001)

[22] Kitaev, A. Y. *Phys. Usp.* **44**, 131 (2001)

[23] Sau, J. D. & Das Sarma, S. *Nat. Commun.* **3**, 964 (2011)

[24] Fulga, I. C.; Haim, A.; Akhmerov, A. R. & Oreg, Y. *New J. Phys.* **15**, 045020 (2013)

[25] Fu, L. *Phys. Rev. Lett.* **104**, 056402 (2010)

[26] van Heck, B.; Akhmerov, A. R.; Hassler, F.; Burrello, M. & Beenakker, C. W. J. *New J. Phys.* **14**, 035019 (2012)

[27] Hyart, T. et al. *Phys. Rev. B* **88**, 035121 (2013)

[28] Aasen, D. et al. *Phys. Rev. X* **6**, 031016 (2016)

[29] Plugge, S.; Rasmussen, A.; Egger, R. & Flensberg, K. *New J. Phys.* **19**, 012001 (2017)

[30] Vijay, S. & Fu, L. *Phys. Rev. B* **94**, 235446 (2016)

[31] Karzig, T. et al. *Phys. Rev. B* **95**, 235305 (2017)

[32] Alicea, J.; Oreg, Y.; Refael, G.; von Oppen, F. & Fisher, M. P. *Nat. Phys.* **7**, 412 (2011)

[33] Hassler, F.; Akhmerov, A. R. & Beenakker, C. W. J. *New J. Phys.* **13**, 095004 (2011)

[34] Alicea, J. *Rep. Prog. Phys.* **75**, 076501 (2012)

[35] Leijnse, M. & Flensberg, K. *Semicond. Sci. Technol.* **27**, 124003 (2012)

[36] von Oppen, F.; Peng, Y. & Pientka, F. *Topological superconducting phases in one dimension.* Topological Aspects of Condensed Matter Physics: Lecture Notes of the Les Houches Summer School. Oxford University Press (2017)

[37] Sau, J. D.; Clarke, D. J. & Tewari, S. *Phys. Rev. B* **84**, 094505 (2011)

[38] Bravyi, S. & Kitaev, A. *Phys. Rev. A* **71**, 022316 (2005)

[39] Bravyi, S. *Phys. Rev. A* **73**, 042313 (2006)

[40] Nayak, C.; Simon, S. H.; Stern, A.; Freedman, M. & Das Sarma, S. *Rev. Mod. Phys.* **80**, 1083 (2008)

[41] Lidar, D. A. & Brun, T. A. *Quantum Error Correction.* Cambridge University Press (2013)

[42] Das Sarma, S.; Freedman, M. & Nayak, C. *Npj Quantum Information* **1**, 15001 (2015)

[43] Mackenzie, A. P. & Maeno, Y. *Rev. Mod. Phys.* **75**, 657 (2003)

[44] Sasaki, S. et al. *Phys. Rev. Lett.* **107**, 217001 (2011)

[45] San-Jose, P.; Lado, J. L.; Aguado, R.; Guinea, F. & Fernández-Rossier, J. *Phys. Rev. X* **5**, 041042 (2015)

[46] Pribiag, V. S. et al. *Nat. Nanotech.* **10**, 593 (2015)

[47] Xu, J.-P. et al. *Phys. Rev. Lett.* **114**, 017001 (2015)

[48] Bocquillon, E. et al. *Nat. Nanotech.* **12**, 137 (2017)

[49] Nadj-Perge, S. et al. *Science* **346**, 602 (2014)

[50] Pientka, F. et al. *Phys. Rev. X* **7**, 021032 (2017)

[51] Hell, M.; Leijnse, M.& Flensberg, K. *Phys. Rev. Lett.* **118**, 107701 (2017)

[52] Mourik, V. et al. *Science* **336**, 1003 (2012)

[53] Albrecht, S. et al. *Nature* **531**, 206 (2016)

[54] Deng, M. T. et al. *Science* **354**, 1557 (2016)

[55] Willett, R. L.; Nayak, C.; Shtengel, K.; Pfeiffer, L. N. & West, K. W. *Phys. Rev. Lett.* **111**, 186401 (2013)

[56] Zibrov, A. A. et al. arXiv:1611.07113 (2016)

[57] Oreg, Y.; Refael, G. & von Oppen, F. *Phys. Rev. Lett.* **105**, 177002 (2010)

[58] Lutchyn, R. M.; Sau, J. D. & Das Sarma, S. *Phys. Rev. Lett.* **105**, 077001 (2010)

[59] Zuo, K. & Mourik, V. Signatures of Majorana Fermions in Hybrid Superconductor-Semiconductor Nanowire Devices. PhD thesis, Delft University of Technology (2016)

[60] Law, K. T.; Lee, P. A. & Ng, T. K. *Phys. Rev. Lett.* **103**, 237001 (2009)

[61] Wimmer, M.; Akhmerov, A. R.; Dahlhaus, J. P. & Beenakker, C. W. J. *New J. Phys.* **13**, 053016 (2011)

[62] Beenakker, C. W. J.; Dahlhaus, J. P.; Wimmer, M. & Akhmerov, A. R. *Phys. Rev. B* **83**, 085413 (2011)

[63] Béri, B. *Phys. Rev. B* **79**, 245315 (2009)

[64] Akhmerov, A. R.; Dahlhaus, J. P.; Hassler, F.; Wimmer, M. & Beenakker, C. W. J. *Phys. Rev. Lett.* **106**, 057001 (2011)

[65] Fulga, I. C.; Hassler, F.; Akhmerov, A. R. & Beenakker, C. W. J. *Phys. Rev. B* **83**, 155429 (2011)

3

Towards high mobility InSb nanowire devices

Önder Gül*, David J. van Woerkom*, Ilse van Weperen*, Diana Car, Sébastien R. Plissard, Erik P.A.M. Bakkers, Leo P. Kouwenhoven

We study the low-temperature electron mobility of InSb nanowires. We extract the mobility at 4.2 Kelvin by means of field effect transport measurements using a model consisting of a nanowire-transistor with contact resistances. This model enables an accurate extraction of device parameters, thereby allowing for a systematic study of the nanowire mobility. We identify factors affecting the mobility, and after optimization obtain a field effect mobility of $\sim 2.5 \times 10^4$ cm^2/Vs. *We further demonstrate the reproducibility of these mobility values which are among the highest reported for nanowires. Our investigations indicate that the mobility is currently limited by adsorption of molecules to the nanowire surface and/or the substrate.*

This chapter has been published in *Nanotechnology* **26**, 215202 (2015).
*These authors contributed equally to this study.

3.1. Introduction

Advances in nanowire growth have led to development of novel quantum devices, such as cooper-pair splitters [1], hybrid semiconductor-superconductor devices [2] and spin-orbit qubits [3]. Nanowire devices thus allow exploration of mesoscopic transport in a highly confined system and show potential as a quantum computation platform. Outstanding nanowire transport properties, such as a high level of tunability of device conductance and low disorder, have been essential to the realization of these experiments.

Recently, hybrid superconductor-semiconducting nanowire devices have been identified [4, 5] as a suitable platform to study Majorana end modes [6], zero-energy bound states that exhibit topological properties. Among various systems, InSb nanowires emerged as a very promising candidate due to their large spin-orbit interaction and large g factor. Reports on signatures of Majorana bound states in InSb nanowire-based systems followed quickly after their theoretical prediction [7–9]. To further develop this topological system, a reduction of the disorder in the nanowire is essential [10, 11]. Disorder reduces or even closes the topological gap that gives Majoranas their robustness, thereby impairing their use as topological qubits. Disorder is quantified by measurements of carrier mobility, which relates directly to the time between scattering events. Evaluation of carrier mobility in nanowires therefore indicates their potential for transport experiments and is thus crucial to further development of nanowire-based quantum devices.

According to the Matthiessen rule, various scattering mechanisms altogether determine the net mobility through [12]

$$\frac{1}{\mu} = \frac{1}{\mu_1} + \frac{1}{\mu_2} + \dots \tag{3.1}$$

Here μ represents the net mobility which results from distinct scattering mechanisms each giving rise to a separate mobility μ_n. In other words, the most dominant scattering contribution limits and hence determines the net mobility. Therefore the mobility can be improved by identifying the limiting mechanism and subsequently reducing or eliminating it.

Apart from the recently introduced Hall effect measurements on nanowires [13, 14], field effect transport measurements are the most common and experimentally most feasible method to extract charge carrier mobility in these systems. Here, one measures the current flowing through the nanowire channel contacted by two electrodes as a function of the gate voltage with fixed voltage bias. The conductance of the channel is described by the linear region of the accumulation regime of a field effect transistor (FET) [15]. In this case the conductance of the channel is

$$G(V_g) = \frac{\mu C}{L^2}\left(V_g - V_{th}\right), \tag{3.2}$$

with gate voltage, V_g, mobility, μ, capacitance, C, channel length, L, and threshold voltage, V_{th}. If the capacitance and the channel length are known, the field effect mobility can be determined from the transconductance, $g_m = dG/dV_g$. In most cases, to extract the mobility, the maximum (peak) transconductance is used. One should note that both the mobility and the field effect transport is described using the Drude model where charge carrier transport is classical and diffusive.

Previous studies showed that low-temperature field effect mobility for nominally undoped III-V nanowires is mainly limited by crystal defects such as stacking faults [16–20], and surface effects such as surface roughness [21, 22]. Point defects are also thought to have an effect on the mobility [23]. However, as they are difficult to detect so far no direct connection between impurities and mobility has been reported. Highest reported low-temperature field effect mobilities are $1.6 - 2.5 \times 10^4$ cm^2/Vs. Such mobilities are observed in InAs nanowires [16, 24], InAs/InP core-shell nanowires [25, 26] and GaN/AlN/AlGaN core-shell nanowires after correction for contact resistances [27]. However, in most of these studies either data on a single device is reported, or the average mobility of several devices is significantly lower than the reported maximum [26]. Systematic studies of such high-mobility nanowire FETs are thus largely lacking.

Concerning field effect mobility, the InSb nanowires we investigate differ in several respects from their oft-studied InAs counterparts: the InSb nanowires we use have a larger diameter of approximately 100 nm, reducing their surface-to-volume ratio compared to the thinner InAs nanowires, and are likely to have no surface accumulation layer. Instead, upward band bending leading to surface carrier depletion has been reported for both clean [28] and oxygen-covered InSb surfaces with (110) orientation, the orientation of our InSb nanowire facets. As the InSb facets are atomically flat no surface roughness is expected. Finally, the nanowires are purely zinc-blende and are free of stacking faults and dislocations. The growth of InSb nanowires we study is described in [29] and [30]. Given the differences between InSb nanowires and other nanowire materials it is an open question what determines the low-temperature mobility in InSb nanowires. We note that while in [29] field effect mobilities of these InSb wires are reported, no systematic investigation of the nanowire mobility was performed. The mobility extraction method presented here allows such a thorough investigation, thereby revealing new insights on nanowire mobility.

To identify the factors affecting the mobility of InSb nanowires, we characterized the low-temperature mobility of nanowire FETs fabricated using different experimental parameters. We tailored the extraction of field effect mobility for the nanowires we study to accurately determine the essential transistor parameters of nanowire FETs. By systematic studies we developed a recipe that results in reproducible average mobilities of $\sim 2.5 \times 10^4$ cm^2/Vs. While this value represents an average over many devices, the extracted mobility from a single measurement may exceed 3.5×10^4 cm^2/Vs. After optimizing the fabrication, we also find that adhesion of molecules to the nanowire and/or the substrate currently limits the extracted mobility. Although such adsorption effects are known to modify the nanowire conductance [17, 31] and also the room-temperature mobility [32–34] (note that ref. [33] reports an increase of mobility upon adsorption, whereas ref. [34] a reduction), our identification of surface adsorption being the limiting factor to low-temperature field effect mobility is new. The amount of adsorbates is reduced by evacuating the sample space for longer time prior to cool down and suggestions for further reduction of the adsorbates as well as to minimize their contribution to the field effect transport are made. We finally discuss various methods to investigate the surface properties of InSb nanowires.

3.2. Experimental details

InSb nanowire FETs are fabricated on a heavily doped Si substrate (used as a global back-gate) terminated with a 285-nm-thick dry thermal SiO_2 (Fig. 3.1b). The substrate is patterned with alignment markers prior to nanowire deposition. Nanowires are positioned on the substrate using a micro-manipulator [35]. Two terminal contacts are realized by electron beam lithography, metal evaporation (Ti/Au 5/145 nm) and lift-off. Argon plasma etching is employed prior to contact deposition. Further details about the fabrication process and the measurements can be found in Supplementary Section 3.S1 and 3.S2, respectively.

Due to the absence of a surface accumulation layer in InSb nanowires, an interface resistance of a few kilo ohms cannot be eliminated upon contacting the nanowire [36]. Such interface resistances are known to reduce the transconductance, resulting in an underestimation of the intrinsic mobility [37, 38]. Moreover, at a temperature of 4 K universal conductance fluctuations complicate the extraction of mobility from transconductance. We therefore tailor the extraction of field effect mobility to our InSb nanowire FETs [39]. We model the interface resistances by a resistor R_s with a fixed value (no gate voltage dependence), connected in series to the nanowire channel. A substantial part of the device resistance at high gate voltage stems from the interface resistances, strongly affecting the gate voltage dependent conductance. This complicates accounting for a possible change of mobility with gate voltage. We therefore assume a mobility independent of gate voltage. The device conductance is then given by (see also Fig. 3.1a)

$$G(V_g) = \left(R_s + \frac{L^2}{\mu C \left(V_g - V_{th} \right)} \right)^{-1}. \tag{3.3}$$

This equation allows for extraction of field effect mobility using a fit to the measured $G(V_g)$. Here, the mobility μ, the interface resistances R_s, and the threshold voltage V_{th} are the free fit parameters. We restrict the fitting range to $G^{-1}(V_g) \leq 100\,\mathrm{k\Omega}$. We independently calculate the capacitance from a finite element model of the device (see Fig. 3.1c inset), where we take into account that quantum confinement in our nanowires reduces the classical capacitance by ~ 20% [40, 41]. Neglecting quantum effects in our capacitance calculation would lower the extracted mobility values by ~ 20%. Further details on the calculation of the capacitance can be found in Supplementary Section 3.S3. We compared the mobility values extracted by a fit using eq. 3.3 with the mobility values obtained from peak transconductance, a common method to extract nanowire mobility, and found matching results (see Supplementary Section 3.S4). For a representative fabrication run, mean forward mobility of 11 devices is found to be $2.9 \times 10^4\,\mathrm{cm^2/Vs}$ using our fit method, whereas peak-transconductance method yields 2.7 (1.9) $\times 10^4\,\mathrm{cm^2/Vs}$ with (without) taking into account the interface resistances. Our fit method, however, differs from peak transconductance method where the mobility is extracted from the maximum value of the transconductance using a small gate voltage range. Because we consider the transconductance in a wide gate voltage range by fitting a large section of $G(V_g)$, the extracted mobility is insensitive to small conductance fluctuations. This is contrary to the peak transconductance where conductance fluctuations greatly affect the extracted mobility. We show in Supplementary Section 3.S5 that our simple

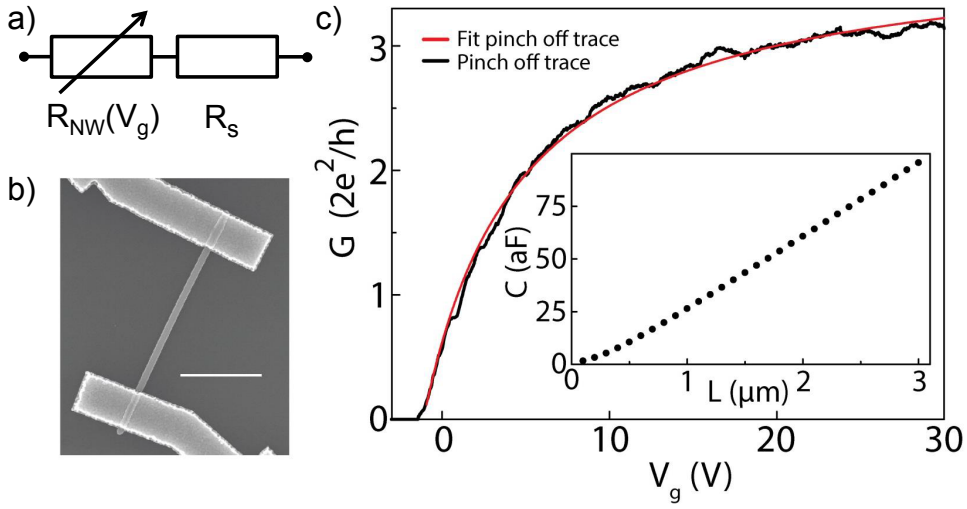

Figure 3.1 | a) Electrical diagram of the InSb nanowire FET. The FET is modelled as a nanowire channel with a resistance controlled by a nearby gate, $R_{NW}(V_g) = G_{NW}^{-1}(V_g)$, in series with fixed interface resistances, R_s. **b)** Electron microscope image of an InSb nanowire FET. Nanowire diameter is ~ 100 nm. The nanowire is deposited onto a Si substrate covered with 285 nm dry thermal SiO_2. Ti/Au (5/145 nm) contacts have spacing of 1, 1.5, 2 or 2.5 μm. Scale bar is 1 μm. **c)** Conductance G, as a function of back gate voltage V_g (black curve). Source-drain bias is set to 10 mV throughout the study. Field effect mobility is extracted from a fit to the conductance (red curve) using eq. 3.3. All measurements are performed at a temperature of 4.2 K. Inset: Gate-nanowire capacitance C, as a function of source-drain contact spacing L. Capacitance is extracted from a finite element model of the device geometry. Contacts are included in the simulated device geometry and lead to a non-linear $C(L)$ at small contact spacing.

model with gate voltage-independent interface resistances is a valid approximation for our measurements. However, despite our thorough analysis a general drawback of field effect mobility remains: the uncertainty in the calculated capacitance value affects the extracted mobility directly. Nanowires suffer from this drawback as their small dimensions do not allow a straightforward experimental extraction of capacitance.

To determine what limits the mobility in our devices, we systematically studied the effect of various experimental parameters by measuring ~ 10 devices simultaneously fabricated on the same substrate. We then change one parameter at a time for each fabrication run to deduce its effect on the field effect mobility.

3.3. Results and discussions

3.3.1. Nanowire surface and adsorption

Nanowire conductivity at room temperature is known to increase after evacuation of the sample space following mounting of devices [17, 42]. We find that evacuation also strongly affects $G(V_g)$ at low temperature (4 K). Comparing the $G(V_g)$ measured for short and long sample space evacuation time prior to cool down, we observe a steeper increase of conductance with gate voltage after long-time evacuation (Fig. 3.2a). Considering a number of devices on the same measurement chip, we find almost a doubling of the mo-

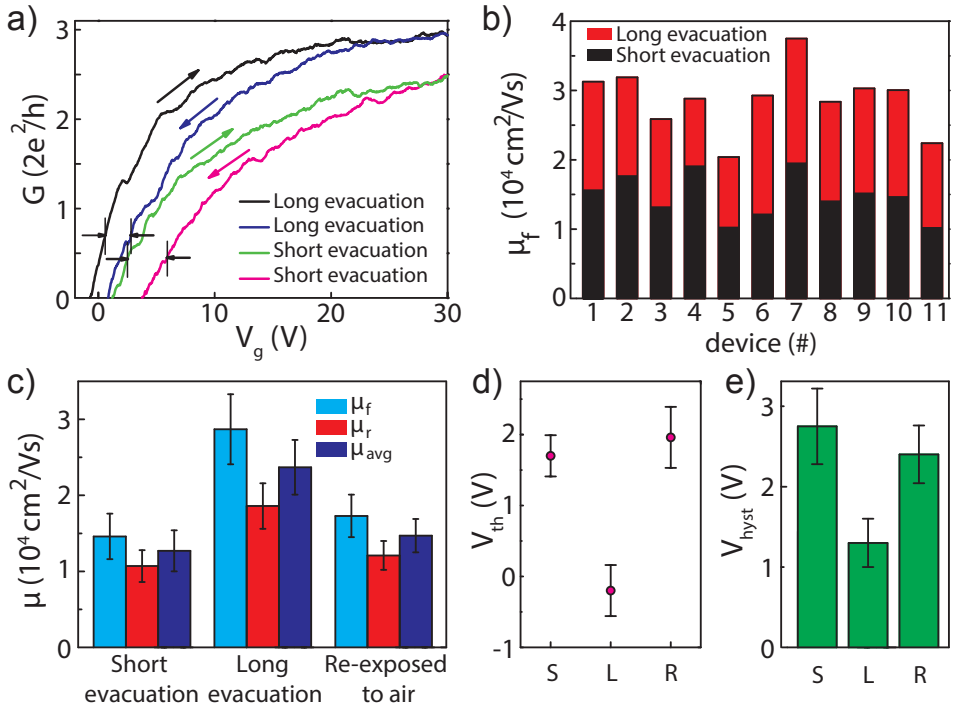

Figure 3.2 | a) Conductance $G(V_g)$ of samples measured after evacuation of the sample space for a short or long period of time prior to cool down. Samples are evacuated for ~ 15 minutes (~ 65 hours), giving the green and pink (black and blue) conductance curves for forward and reverse sweep direction respectively. Arrows indicate sweep direction. The same chip with nanowire devices is first evacuated only shortly (yielding the data denoted with 'short evacuation'), then evacuated for longer-time ('long evacuation' data), reexposed to air for ~ 90 hours and evacuated shortly (~ 15 minutes) again ('re-exposure' data), see panel c. The substrate was cleaned prior to nanowire deposition. Hysteresis of both pairs of conductance curves is indicated with arrows and vertical lines. Although the hysteresis is indicated at non-zero G, the hysteresis reported in panel c is extracted from the difference in threshold voltage between conductance curves with forward and reverse sweep direction. **b)** Mobility obtained with forward sweep direction, μ_f, of individual devices after short (black) or long (red) device evacuation time. **c)** Mobility after short-time evacuation, long-time evacuation, and reexposure to air. μ_{avg} is the average of the mobility obtained with forward sweep direction, μ_f, and with reverse sweep direction, μ_r. **d)** Threshold voltage extracted from forward sweep direction, V_{th} after short-time evacuation (S), long-time evacuation (L) and reexposure to air (R). **e)** Hysteresis V_{hyst}, after short-time evacuation (S), long-time evacuation (L) and reexposure to air (R). The hysteresis is given by the difference in threshold voltage between forward and reverse sweep direction. All values in panels c, d and e are an average, obtained from fits to the conductance curve of each device on the measurement chip. Error bars in panels c, d and e indicate the standard deviation.

bility values after long-time sample evacuation (Fig. 3.2b). The re-exposure of samples to air after long-time evacuation results in a reduction of mobility (Fig. 3.2c) with values very similar to those obtained from the initial measurements with a short-time sample space evacuation. The transconductance is larger when the gate is swept from low towards high voltages (forward sweep direction) leading to higher mobility compared to the case of sweeping from high gate voltages to low (reverse sweep direction) (Fig. 3.2c).

Moreover, after long-time evacuation a shift of the threshold voltage towards more negative values is observed (Fig. 3.2d) together with a reduced hysteresis (Fig. 3.2e). Both the threshold voltage and the hysteresis regain their initial values obtained from short-time evacuation once the sample is re-exposed to air, similar to the extracted mobility: exposing the devices to air has a reversible effect on the field effect transport parameters we extract from the fits. All extracted fit parameters can be found in Supplementary Table 3.S1.

A hysteresis in transconductance dependent on ambient conditions has been studied before by Kim *et al* [43] and Wang *et al* [44], and was attributed to the adsorption of water onto the nanostructure and onto the SiO_2 substrate. Evacuation of the sample environment leads to desorption of water, thereby reducing the hysteresis. However sample evacuation alone is insufficient to fully remove the adsorbed water. The similarities between our observations and those reported by Wang *et al* and Kim *et al*, considering both the influence of gate voltage sweep direction on the shift of the threshold voltage, as well as the reduction of hysteresis with evacuation time and the reversibility of the effect when reexposing samples to air, strongly suggest that the field effect transport is affected by molecules adsorbed to the nanowire and/or the SiO_2 substrate. Water is highly likely to be the main adsorbate because reexposing the device to ambient atmosphere following long evacuation time of sample space yields values of mobility, threshold voltage and hysteresis similar to those obtained from the measurements with short evacuation time. InSb nanowires have however also shown decreased conductance in response to isopropanol and acetone [31].

It is an open question how adsorbates affect device conductance at low temperature. The alignment of polar molecules by gate electric field may result in an additional gating [44]. However, the mechanism through which such alignment causes hysteresis is not clear. Another scenario is charge trapping by adsorbed molecules [43]. Such trapping could possibly lead to an asymmetry between forward and reverse sweep direction, yielding the observed hysteresis and sweep direction dependent mobility. The observed trapping mechanism is likely to have a long response time, as our measurements are taken at relatively low gate voltage sweep rates (120 mV/s). Unlike refs. [32, 43, 44], we find no dependence on sweep rate for rates between 3 – 600 mV/s. Nonetheless, repeated measurements yield the same $G(V_g)$, implying that between scans the traps are emptied.

3.3.2. Substrate cleaning

We further find that cleaning of Si/SiO_2 substrates by remote oxygen plasma prior to nanowire deposition results in an enhanced gate dependence of low-temperature conductivity. Fig. 3.3a shows $G(V_g)$ curves of individual devices, while Fig. 3.3b shows an average over extracted mobilities obtained from measurements of ~ 10 FETs with and without substrate cleaning. All other fabrication and measurement steps are the same for both sets of devices. The remote oxygen plasma most probably removes hydrocarbons that remain on the substrates after fabrication of alignment markers or during storage of samples in a polymer-containing environment. We verified that the oxygen plasma cleaning does not decrease the thickness of the SiO_2 gate dielectric within the measurable range < 1 nm.

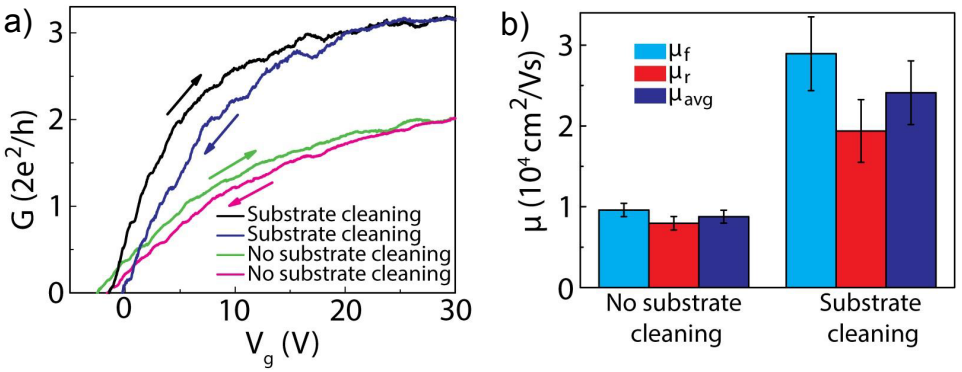

Figure 3.3 | a) Conductance curves $G(V_g)$ obtained from samples without and with substrate cleaning. Forward and reverse sweep direction are indicated with arrows. Samples have been evacuated for ~ 60 hours before cool down. **b)** Forward, reverse and average mobility with and without substrate cleaning. Values are averages obtained from fits to conductance curves of individual devices. Error bars indicate standard deviation.

3.3.3. Contact spacing

A correlation between FET source-drain contact spacing and extracted field effect mobility is found (Fig. 3.4). Although the spread in mobility at a given contact spacing is substantial, an overall increase of extracted mobility is observed with increasing contact spacing. To determine whether the dependence of the field effect mobility on contact spacing originates from the length of the used nanowire, FETs with short (1 μm) contact

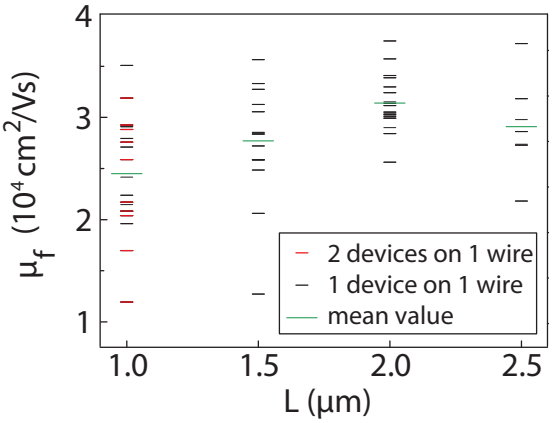

Figure 3.4 | Mobility obtained by sweeping the gate voltage in forward direction, μ_f, as a function of source-drain contact spacing L. Data from 5 different measurement chips (see Supplementary Section 3.S6). Red lines indicate mobility values obtained from long nanowires on which three contact electrodes were placed, resulting in two FETs in series, while black lines correspond to the mobility of single FET devices. Mean forward mobility for each contact spacing is $\mu_{f,m}(L = 1\,\mu\text{m}) = 2.4\times10^4$ cm^2/Vs, $\mu_{f,m}(L = 1.5\,\mu\text{m}) = 2.8\times10^4$ cm^2/Vs, $\mu_{f,m}(L = 2\,\mu\text{m}) = 3.1\times10^4$ cm^2/Vs and $\mu_{f,m}(L = 2.5\,\mu\text{m}) = 2.9\times10^4$ cm^2/Vs.

spacing were realized both on short wires, and on long wires using three contact electrodes resulting in two FETs in series. Devices made from both long and short wires with 1 μm contact spacing give similar mobility (see Fig. 3.4). The contact spacing dependence is thus a device property rather than a nanowire property.

A reduced mobility for short contact spacing is expected when transport is (quasi-) ballistic rather than diffusive [45, 46]. We have observed ballistic transport in our wires [36] with a device geometry and measurement conditions different from those here. Here we expect quasi-ballistic transport in our devices with a mean free path comparable to nanowire diameter $l_e \sim 0.1\,\mu$m. While devices with $L/l_e \gg 1$ are preferable, our InSb nanowires can currently not be grown longer than $\sim 3.5\,\mu$m. However, while for channel length of 1 μm (quasi-)ballistic effects may play a role, mobility values obtained from our devices with longer contact spacing yield a better estimate of field effect mobility. Moreover, effects related to the metal contacts are expected to play a larger role in devices with short contact spacing and can possibly contribute to the observed decrease of $\mu(L)$ in short channel devices. Possible explanations are that (1) the contacts reduce the capacitance of short devices more than expected from the Laplace simulations (in which the nanowire is assumed to be metallic) or (2) electrons are injected from and absorbed over a finite length underneath the contacts, leading to an effective L larger than the contact spacing.

3.3.4. Reproducibility

Altogether, cleaning the SiO_2 substrate before wire deposition and applying a long sample evacuation time yields $\mu_{avg} \approx 2.5 \times 10^4\,\mathrm{cm}^2/\mathrm{Vs}$ for devices with a contact spacing $L = 2\,\mu$m. This mobility is the average value of $\mu_f = 3.1 \times 10^4\,\mathrm{cm}^2/\mathrm{Vs}$ (see Fig. 3.4) and $\mu_r = 1.9 \times 10^4\,\mathrm{cm}^2/\mathrm{Vs}$. These high mobilities result from measurements of ~ 15 devices

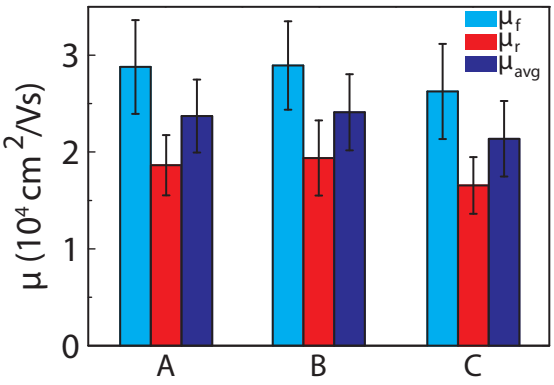

Figure 3.5 | Average mobilities obtained with forward (μ_f) and reverse (μ_r) sweep direction. First group of data (batch A) corresponds to the fabrication run presented in Fig. 3.2 (long-time evacuation), batch B is presented in Fig. 3.3b (with substrate cleaning), whereas batch C is a separate batch to demonstrate the reproducibility of our results. Average mobility μ_{avg} is the average of forward and reverse mobility. All results are obtained by improved cleaning of the substrate and long evacuation time of the sample space. Error bars indicate standard deviation.

fabricated in different fabrication runs (see Supplementary Section 3.S6 for details) using the same fabrication recipe. Fig. 3.5 demonstrates the reproducibility of our results: mobility obtained from three different fabrication runs are very similar. The optimized nanofabrication recipe as well as an overview of all the parameters extracted from the fits to the conductance vs. gate voltage curves that yield Fig. 3.5 are given in Supplementary Section 3.S1 and Supplementary Table 3.S2, respectively.

3.4. Conclusions and outlook

Low-temperature field effect mobility of InSb nanowires is extracted by measuring the conductance as a function of gate voltage. Taking surface adsorption and substrate cleaning into consideration, an optimized nanofabrication recipe has been obtained yielding average field effect mobilities of $\sim 2.5 \times 10^4$ cm^2/Vs. It is demonstrated that the obtained mobility values are highly reproducible.

As we show that surface adsorption has a large impact on field effect mobility, further studies should be directed towards minimizing the adsorbates and analysis of surface properties. An improved design of the measurement setup allowing for heating and better evacuation of the sample space is likely to facilitate a further desorption of adsorbates. Exposing the devices to UV-light during evacuation, which may assist desorption, can also be investigated [31]. Further, passivating the nanowire surface by removing the native oxide followed by application of a high quality dielectric likely reduces surface adsorption. Possible methods are atomic hydrogen cleaning [47] or chemical etching followed by dielectric deposition [48]. Alternatively, by suspending the nanowires above a metallic gate using vacuum as a dielectric, one can minimize the effects of the substrate adsorption, leaving the wire adsorption as the predominant constituent affecting the field effect mobility. In the case of adsorbates creating a fluctuating potential profile along the wire resulting in charge scattering, a core-shell structure is expected to yield a higher field effect mobility because the potential fluctuations due to adsorbates are spatially separated from the channel owing to the shell. Finally, to study the surface composition of the nanowire and the substrate, x-ray photoelectron spectroscopy or Auger electron spectroscopy could be used [49].

3.S. Supplementary Information

3.S1. Optimized fabrication recipe

- Substrate cleaning: 10 minutes remote oxygen plasma cleaning (Tepla 300 Plasma Asher) of the p^{++}-Si substrate covered with 285 nm dry thermal SiO_2 with predefined Au alignment markers (oxygen pressure 1 mbar, plasma power 600 W). All substrates were from the same wafer.

- Wire deposition: deterministic positioning of wires using a setup similar to that described in ref. [35]. Wires were always taken from the same section on the same growth chip.

- SEM imaging of the nanowires with surrounding alignment markers. Images are used for the subsequent design of the contacts.

- Spin resist: PMMA 950A4 at 4 krpm, baking > 15 minutes at a temperature of 175 °C.
- Electron beam writing of the contact design.
- Development: MIBK:IPA 1:3 60 s, IPA 60 s.
- Ar etching (AJA International sputtering system) using rf-plasma: pressure 3 mTorr, Ar flow 50 sccm, power 100 W, duration 300 s, no rotation of the sample holder. A voltage of 300 V is applied to the sample holder.
- Contact deposition: e-beam evaporation of Ti/Au 5/145 nm with deposition rate 0.5 Å/s and 2 Å/s respectively.
- Lift-off in acetone: the sample with acetone is heated for several hours and left in acetone for ≥ 12 h.
- Samples were stored in an Ar glove box between fabrication and mounting.

3.S2. Measurements

- Sample space (IVC) evacuated for ~ 60 hours after mounting (insert type: Desert Cryogenics).
- For thermalisation, He of ~10 mbar is added to sample space at room temperature before cooling down the devices. During low-temperature measurements samples are kept in a vacuum environment.
- $G(V_g)$ measured using 10 mV bias, gate voltage range from −6 V to +30 V with sweep rate 6 mV/50 ms. Measured in forward and reverse sweep direction.
- To check a possible sweep rate dependence of $G(V_g)$, gate voltage steps of 0.15, 0.3, 0.6, 1.5, 3, 6, 15, 30 [mV/(50 ms)] is used both in forward and reverse sweep direction. No dependence on sweep rate was found.

3.S3. Device capacitance

The capacitance for different channel lengths is calculated with a 3D Laplace solver for a realistic device geometry including the metallic leads. Here the wire is assumed to be metallic. Then, for a more accurate representation of the device capacitance and to account for quantum confinement effects, 2D Schrödinger-Poisson solver was used and its result is compared with the capacitance calculated with 2D Laplace solver. A reduction of capacitance by 20% is found for the case of quantum mechanical treatment of the wire. In Fig. 3.1c (inset), the capacitance calculated by 3D Laplace solver with a 20% reduction is plotted. These plotted capacitance values are used for mobility extraction and expected to represent channel capacitance realistically.

3.S4. Comparison of field effect mobility extraction methods

We extract mobility values by fitting the conductance curves $G(V_g)$ in a large gate voltage range. However, in the literature mobility is commonly extracted from a small gate voltage range where the transconductance has its maximum value (peak transconductance). This gate voltage range is typically close to the threshold voltage where the mo-

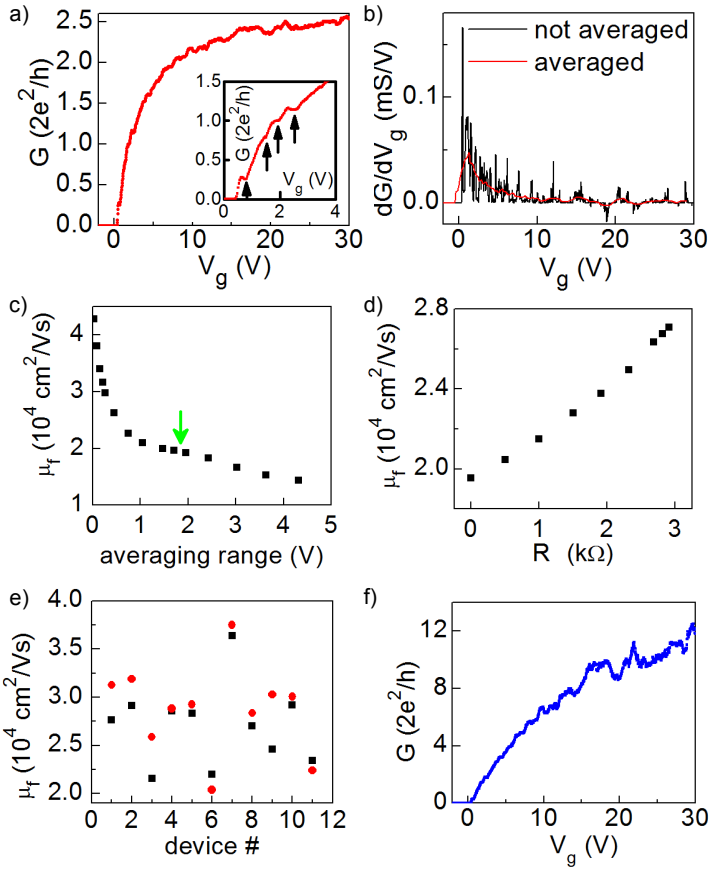

Figure 3.S1 | a) Conductance G, as a function of gate voltage V_g. Inset: Zoom-in of the conductance near pinch-off. The arrows point at universal conductance fluctuations resulting in fluctuations in transconductance. **b)** Transconductance dG/dV_g without (black) and with (red) averaging over 1.8 V gate voltage range. Averaging is applied to remove the fluctuations that lead to peaks and dips in the transconductance. **c)** Field effect mobility μ_f obtained from peak transconductance as a function of gate voltage averaging range. Plotted values of peak-mobility is the average of 11 devices on the same chip (long evacuation time experiment, Fig. 3.2). The green arrow denotes the averaging range of 1.8 V used for the averaged curve in panel b. This averaging window is used in further analysis to obtain peak-mobility. **d)** Peak-mobility as a function of series resistance subtracted from $G(V_g)$. Peak-mobility is the average of 11 devices on the same chip. **e)** Comparison between field effect mobility μ_f obtained for individual devices using the fit according to eq. 3.3 (red points) and the mobility obtained from peak transconductance (black points). **f)** Conductance as a function of gate voltage after the correction for interface resistances. For this device an interface resistance R_s = 4 kΩ is assumed. Conductance curve without the correction for R_s is shown in panel a.

bility is expected to be the highest. Here, we compare the field effect mobility obtained using our method – fitting the conductance curves $G(V_g)$ – to the field effect mobility obtained from peak transconductance, the standard method for extracting mobility in nanowires. We denote the mobility obtained using the latter as peak-mobility. We describe the extraction of peak-mobility in the following: By numerically differentiating the measured $G(V_g)$ shown in Fig. 3.S1a, one obtains the transconductance $g_m = dG/dV_g$. This transconductance is shown in Fig. 3.S1b (black curve). After taking the numerical derivative, an averaging is performed to remove the fluctuations in transconductance (red curve in Fig. 3.S1b). The peak-mobility is then obtained from the maximum value of transconductance using $\mu = g_m L^2/C$ (see eq. 3.2). Peak-mobility depends strongly on the chosen averaging range. This dependence is shown in Fig. 3.S1c. Here, mean forward peak-mobility of 11 devices from a single fabrication run is plotted against the averaging range. We choose the averaging range to be 1.8 V, the value at which the rapid decrease of peak-mobility with respect to averaging range diminishes.

Next interface resistances are taken into account since they affect the extracted peak-mobility. This is done by subtracting the contribution of a gate-independent series resistance R from the measured conductance curve $G(V_g)$. Fig. 3.S1f shows an example of such a conductance curve corrected for interface resistances. From such a curve we determine the transconductance, and from the maximum value of transconductance peak-mobility is extracted. The peak-mobility depends on the subtracted R, shown in Fig. 3.S1d. Here, as mentioned above, mean forward peak-mobility of 11 devices from a single fabrication run is plotted. (The peak-mobility for $R = 0$ is the one indicated with a green arrow in Fig. 3.S1c.) For zero subtracted resistance ($R = 0$), the transconductance has a global maximum near pinch-off (Fig. 3.S1b, red curve). Upon increasing the value of R subtracted from $G(V_g)$, the transconductance values increase for all gate voltages, with the amount of increase being larger for higher gate voltages. When R exceeds the value of interface resistances R_s, the transconductance no longer has a global maximum near pinch-off. When R is increased even further, transconductance starts to increase with gate voltage, a case we regard to be unrealistic. R_s for individual devices varies between 1.5 kΩ and 4 kΩ, with an average R_s of ~ 3 kΩ. After the subtraction of R_s, the mean peak-mobility of 11 devices obtained using forward sweep direction is (27.1 ± 4.2) × 10^3 cm^2/Vs (see Fig. 3.S1d) compared to (28.7 ± 4.8) × 10^3 cm^2/Vs obtained from fits to the conductance curves. Both values are within error margin the same. Comparing mobilities of individual devices obtained using both methods (Fig. 3.S1e), we conclude that both methods give similar values. The small difference is due to slightly larger interface resistances obtained from the fitting method, giving an average R_s of 3.7 kΩ.

3.S5. Simplification of gate voltage-independent interface resistances

Here we check our simplification of modelling the interface resistances R_s to be gate voltage independent. We fit the measured device conductance $G(V_g)$ using eq. 3.3 to determine R_s, the mobility μ, and the threshold voltage V_{th}. The measured device conductance after the subtraction of R_s is denoted by $G_{\mathrm{ch}}(V_g)$. In our model $G_{\mathrm{ch}}(V_g)$ has the form $G_{\mathrm{L}}(V_g) = (V_g - V_{th})\mu C/L^2$, which corresponds to a conductance linear in gate voltage with the transport properties extracted from the fit mentioned above. In Fig. 3.S2 we plot representative curves of $G_{\mathrm{ch}}(V_g)$ (black) and compare them with $G_{\mathrm{L}}(V_g)$ (red). We

find that $G_L(V_g)$ matches well with $G_{ch}(V_g)$, demonstrating that our simple model with gate voltage-independent interface resistances is a valid approximation for our measurements.

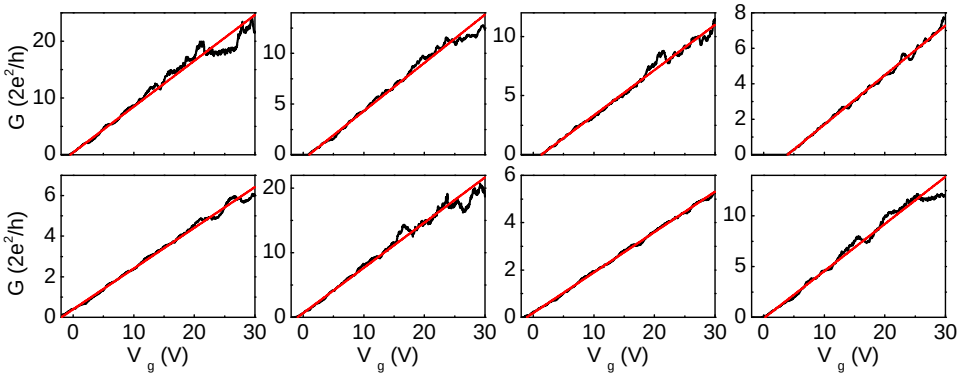

Figure 3.S2 | Panels show the measured device conductance after subtracting the interface resistance, $G_{ch}(V_g)$ (black), together with $G_L(V_g)$ (red), which is the conductance linear in gate voltage with the transport properties extracted from the fit. $G_{ch}(V_g)$ shown in upper row (lower row) are from the data set presented in Fig. 3.2a (Fig. 3.3a).

3.S6. Overview of measured devices

- Evacuation time experiment (fabricated according to our optimized recipe described above). Mobility was extracted from measurements of 11 devices with contact spacing between 1 and 2 μm. Average contact spacing 1.41 μm. Data reported in Fig. 3.2. Long evacuation time data is also included in Fig. 3.4 and Fig. 3.5 (Batch A).

- FETs without substrate cleaning and with long-time evacuation. Fabricated according to our optimized recipe, with the exception that we used different settings for Ar etching. Here we used 400 V on the sample holder and etched for 150 s while keeping all the other settings the same. This yields the same amount of etching of InSb nanowire ($\sim$ 70 nm) as etching at 300 V for 300 s. 11 devices, contact spacing of all devices is 2 μm. Data reported in Fig. 3.3.

- FETs with substrate cleaning and with long-time evacuation. Fabricated according to our optimized recipe, with the exception that we used different settings for Ar etching. Here we used 400 V on the sample holder and etched for 150 s while keeping all the other settings the same. This yields the same amount of etching of InSb nanowire ($\sim$ 70 nm) as etching at 300 V for 300 s. 11 devices, contact spacing between 1 and 2 μm. Average length 1.42 μm. Data reported in Fig. 3.3, Fig. 3.4, and Fig. 3.5 (Batch B).

- FETs fabricated according to our optimized recipe. 13 devices, contact spacing between 1 and 2.5 μm. Average contact spacing 1.73 μm. Data reported in Fig. 3.4 and Fig. 3.5 (Batch C).

- FETs fabricated according to the recipe, with the addition of a thin layer of perfluorodecyltrichlorosilane (FDTS) deposited onto the devices after fabrication. No improvement of mobility was observed with respect to devices without FDTS. 11 devices, contact spacing between 1 and 2.5 μm. Average contact spacing 1.64 μm. Data reported in Fig. 3.4.

- FETs fabricated according to our optimized recipe, but with substrate oxygen plasma cleaning of 60 s instead of 10 minutes. After oxygen plasma cleaning a thin layer of FDTS was deposited onto the substrate, after which fabrication proceeded according to the recipe. No improvement of mobility was observed with respect to devices without FDTS and with the usual 10 minutes cleaning. 10 devices, contact spacing between 1 and 2.5 μm. Average contact spacing 1.85 μm. Data reported in Fig. 3.4.

3.S7. Average device characteristics obtained from several measurement and fabrication runs

	Short-time evacuation	Long-time evacuation	Reexposed to air
μ_f (10^3 cm^2/Vs)	14.6 ± 3.0	28.7 ± 4.6	17.3 ± 2.8
μ_r (10^3 cm^2/Vs)	10.7 ± 2.1	18.6 ± 3.0	12.1 ± 1.9
μ_{avg} (10^3 cm^2/Vs)	12.7 ± 2.7	23.7 ± 3.6	14.7 ± 2.2
V_{th} (V)	1.70 ± 0.29	-0.20 ± 0.36	1.96 ± 0.43
V_{hyst} (V)	2.75 ± 0.47	1.31 ± 0.30	2.40 ± 0.36
R_s ($k\Omega$)	3.7 ± 0.7	3.7 ± 1.0	4.1 ± 1.2

Table 3.S1 | Mobility, threshold voltages V_{th}, hysteresis, V_{hyst} and series resistances, R_s, extracted from fits to conductance curves $G(V_g)$ of the evacuation time experiment. Mobility is obtained with forward sweep direction, μ_f and reverse sweep direction, μ_r. The average mobility of these two sweep directions, μ_{avg}, is also reported. V_{th} is the threshold voltage obtained from fits to $G(V_g)$ taken with forward sweep direction. Mobility, threshold voltage and hysteresis are also shown in Fig. 3.2c, d and e, respectively.

Batch	A	B	C
μ_f (10^3 cm^2/Vs)	28.7 ± 4.6	28.9 ± 4.4	26.0 ± 4.7
μ_r (10^3 cm^2/Vs)	18.6 ± 3.0	19.4 ± 3.9	16.4 ± 3.0
μ_{avg} (10^3 cm^2/Vs)	23.7 ± 3.6	24.2 ± 3.9	21.2 ± 3.8
V_{th} (V)	-0.20 ± 0.36	-0.51 ± 0.45	-0.37 ± 0.39
V_{hyst} (V)	1.31 ± 0.30	1.14 ± 0.22	1.41 ± 0.28
R_s ($k\Omega$)	3.7 ± 1.0	3.0 ± 0.8	4.8 ± 1.8

Table 3.S2 | Mobility, threshold voltage, V_{th}, hysteresis, V_{hyst}, and series resistance, R_s, obtained from fits to the conductance curves $G(V_g)$ of three batches of high-mobility devices. Mobility is obtained with forward sweep direction, μ_f and reverse sweep direction, μ_r. The average mobility of these two sweep directions, μ_{avg}, is also reported. V_{th} is the threshold voltage obtained from fits to $G(V_g)$ taken using forward sweep direction. Mobilities and series resistances are also shown in Fig. 3.5.

Acknowledgement

We thank K. Zuo, D. Szombati, V. Mourik, A. Geresdi and J. W. G. van den Berg for preliminary studies and fruitful discussions. This work has been supported by Dutch Organisation for Scientific Research (NWO), Foundation for Fundamental Research on Matter (FOM), European Union Seventh Framework Programme under grant agreement no. 265073 (NANOWIRING), and Microsoft Corporation Station Q.

Author contribution

Ö.G., D.J.v.W., and I.v.W. fabricated the devices, performed the measurements, analyzed the data, and wrote the manuscript. D.C., S.P. and E.P.A.M.B. grew the InSb nanowires. L.P.K. supervised the project. All authors commented on the manuscript.

References

[1] L. Hofstetter, S. Csonka, J. Nygård and C. Schönenberger. Cooper pair splitter realized in a two-quantum-dot Y-junction. *Nature* **461,** 960-963 (2009)

[2] Y.-J. Doh, J. A. van Dam, A. L. Roest, E. P. A. M. Bakkers, L. P. Kouwenhoven and S. De Franceschi. Tunable supercurrent through semiconductor nanowires. *Science* **309,** 272-275 (2005)

[3] S. Nadj-Perge, S. M. Frolov, E. P. A. M. Bakkers and L. P. Kouwenhoven. Spin-orbit qubit in a semiconductor nanowire. *Nature* **468,** 1084-1087 (2010)

[4] R. M. Lutchyn, J. D. Sau and S. Das Sarma. Majorana fermions and a topological phase transition in semiconductor-superconductor heterostructures. *Phys. Rev. Lett.* **105,** 077001 (2010)

[5] Y. Oreg, G. Refael and F. von Oppen. Helical liquids and Majorana bound states in quantum wires. *Phys. Rev. Lett.* **105,** 177002 (2010)

[6] E. Majorana. Teoria simmetrica dell'elettrone e del positrone. *Nuovo Cimento* **14,** 171-184 (1937)

[7] V. Mourik, K. Zuo, S. M. Frolov, S. R. Plissard, E. P. A. M. Bakkers and L. P. Kouwenhoven. Signatures of Majorana fermions in hybrid superconductor-semiconductor nanowire devices. *Science* **336,** 1003-1007 (2012)

[8] M. T. Deng, C. L. Yu, G. Y. Huang, M. Larsson, P. Caroff and H. Q. Xu. Anomalous zero-bias conductance peak in a Nb-InSb nanowire-Nb hybrid device. *Nano Lett.* **12,** 6414-6419 (2012)

[9] H. O. H. Churchill, V. Fatemi, K. Grove-Rasmussen, M. T. Deng, P. Caroff, H. Q. Xu and C. M. Marcus. Superconductor-nanowire devices from tunneling to the multichannel regime: Zero-bias oscillations and magnetoconductance crossover. *Phys. Rev. B* **87,** 241401(R) (2013)

[10] J. D. Sau, S. Tewari and S. Das Sarma. Experimental and materials considerations for the topological superconducting state in electron- and hole-doped semiconductors: Searching for non-Abelian Majorana modes in 1D nanowires and 2D heterostructures. *Phys. Rev. B* **85,** 064512 (2012)

[11] A. C. Potter and P. A. Lee. Engineering a p+ip superconductor: Comparison of topological insulator and Rashba spin-orbit-coupled materials. *Phys. Rev. B* **83,** 184520 (2011)

[12] N. W. Ashcroft and N. D. Mermin. *Solid State Physics*. New York: Holt, Rinehart and Winston (1976)

[13] C. Blömers, T. Grap, M. I. Lepsa, J. Moers, S. Trellenkamp, D. Grützmacher, H. Lüth and T. Schäpers. Hall effect measurements on InAs nanowires. *Appl. Phys. Lett.* **101,** 152106 (2012)

[14] K. Storm, F. Halvardsson, M. Heurlin, D. Lindgren, A. Gustafsson, P. M. Wu, B. Monemar and L. Samuelson. Spatially resolved Hall effect measurement in a single semiconductor nanowire. *Nature Nanotech.* **7,** 718-722 (2012)

[15] S.M. Sze. *Physics of Semiconductor Devices*. 2nd ed. New York: Wiley (1981)

[16] M. D. Schroer and J. R. Petta. Correlating the nanostructure and electronic properties of InAs nanowires. *Nano Lett.* **10,** 1618-1622 (2010)

[17] A. V. Kretinin, R. Popovitz-Biro, D. Mahalu and H. Shtrikman. Multimode Fabry-Perot conductance oscillations in suspended stacking-faults-free InAs nanowires. *Nano Lett.* **10,** 3439-3445 (2010)

[18] H. Shtrikman, R. Popovitz-Biro, A. V. Kretinin and P. Kacman. GaAs and InAs Nanowires for ballistic transport. *IEEE J. Selected Top. Quant. Electron.* **17,** 922-934 (2011)

[19] N. Gupta, Y. Song, G. W. Holloway, U. Sinha, C. M. Haapamaki, R. R. Lapierre and J. Baugh. Temperature-dependent electron mobility in InAs nanowires. *Nanotechnology* **24,** 225202 (2013)

[20] M. J. L. Sourribes, I. Isakov, M. Panfilova, H. Liu and P. A. Warburton. Mobility enhancement by Sb-mediated minimisation of stacking fault density in InAs nanowires grown on silicon. *Nano Lett.* **14,** 1643-1650 (2014)

[21] A. C. Ford, S. B. Kumar, R. Kapadia, J. Guo and A. Javey. Observation of degenerate one-dimensional sub-bands in cylindrical InAs nanowires. *Nano Lett.* **12,** 1340-1343 (2012)

[22] S. Chuang, Q. Gao, R. Kapadia, A. C. Ford, J. Guo and A. Javey. Ballistic InAs nanowire transistors. *Nano Lett.* **13,** 555-558 (2013)

[23] M. Bar-Sadan, J. Barthel, H. Shtrikman and L. Houben. Direct imaging of single Au atoms within GaAs nanowires. *Nano Lett.* **12,** 2352-2356 (2012)

[24] F. Wang, S. Yip, N. Han, K. Fok, H. Lin, J. J. Hou, G. Dong, T. Hung, K. S. Chan and J. C. Ho. Surface roughness induced electron mobility degradation in InAs nanowires. *Nanotechnology* **24,** 375202 (2013)

[25] X. Jiang, Q. Xiong, S. Nam, F. Qian, Y. Li and C. M. Lieber. InAs/InP radial nanowire heterostructures as high electron mobility devices. *Nano Lett.* **7,** 3214-3218 (2007)

[26] J. W. W. van Tilburg, R. E. Algra, W. G. G. Immink, M. A. Verheijen, E. P. A. M. Bakkers and L. P. Kouwenhoven. Surface passivated InAs/InP core/shell nanowires. *Semicond. Sci. Technol.* **25,** 024011 (2010)

[27] Y. Li, J. Xiang, F. Qian, S. Gradecak, Y. Wu, H. Yan, D. A. Blom and C. M. Lieber. Dopant-free GaN/AlN/AlGaN radial nanowire heterostructures as high electron mobility transistors. *Nano Lett.* **6,** 1468-1473 (2006)

[28] G. W. Gobeli and F. G. Allen. Photoelectric properties of cleaved GaAs, GaSb, InAs, and InSb surfaces; Comparison with Si and Ge. *Phys. Rev.* **137,** A150-A158 (1965)

[29] S. R. Plissard, D. R. Slapak, M. A. Verheijen, M. Hocevar, G. W. G. Immink, I. van Weperen, S. Nadj-Perge, S. M. Frolov, L. P. Kouwenhoven and E. P. A. M. Bakkers. From InSb nanowires to nanocubes: looking for the sweet spot. *Nano Lett.* **12,** 1794-1798 (2012)

[30] D. Car, J. Wang, M. A. Verheijen, E. P. A. M. Bakkers and S. R. Plissard. Rationally designed single-crystalline nanowire networks. *Adv. Mater.* **26,** 4875 (2014)

[31] M. V. Penchev. Ph.D. thesis, University of California, Riverside (2012)

[32] S. A. Dayeh, P. K. L. Yu, E. T. Yu and D. Wang. Transport properties of InAs nanowire field effect transistors: The effects of surface states. *Journ. Vac. Sci. Technol. B* **25,** 1432 (2007)

[33] J. Du, D. Liang, H. Tang, X. P. A. Gao. InAs nanowire transistors as gas sensor and the response mechanism. *Nano Lett.* **9,** 4348-4351 (2009)

[34] P. Offermans, M. Crego-Calama, S. H. Brongersma. Gas Detection with vertical InAs nanowire arrays. *Nano Lett.* **10,** 2412-2415 (2010)

[35] K. Flöhr, M. Liebmann, K. Sladek, H. Y. Günel, R. Frielinghaus, F. Haas, C. Meyer, H. Hardtdegen, T. Schäpers, D. Grützmacher and M. Morgenstern. Manipulating InAs nanowires with submicrometer precision. *Rev. Sci. Instrum.* **82,** 113705 (2011)

[36] I. van Weperen, S. R. Plissard, E. P. A. M. Bakkers, S. M. Frolov and L. P. Kouwenhoven. Quantized conductance in an InSb nanowire. *Nano Lett.* **13,** 387-391 (2013)

[37] D. K. Schroder. *Semiconductor Material and Device Characterization.* 3rd ed. New York: John Wiley & Sons (2006)

[38] W. Lu, P. Xie and C. M. Lieber. Nanowire transistor performance limits and applications. *IEEE Trans. Electron Dev.* **55,** 2859-2876 (2008)

[39] S. R. Plissard, I. van Weperen, D. Car, M. A. Verheijen, G. W. G. Immink, J. Kammhuber, L. J. Cornelissen, D. B. Szombati, A. Geresdi, S. M. Frolov, L. P. Kouwenhoven and E. P. A. M. Bakkers. Formation and electronic properties of InSb nanocrosses. *Nature Nanotech.* **8,** 859-864 (2013)

[40] L. Wang, D. Wang and P. M. Asbeck. A numerical Schrödinger-Poisson solver for radially symmetric nanowire core-shell structures. *Solid-State Electron.* **50,** 1732-1739 (2006)

[41] D. Eeltink. M.Sc. thesis, Delft University of Technology (2013)

[42] S. Nadj-Perge. Ph.D. thesis, Delft University of Technology (2010)

[43] W. Kim, A. Javey, O. Vermesh, Q. Wang, Y. Li and H. Dai. Hysteresis Caused by Water Molecules in Carbon Nanotube Field-Effect Transistors. *Nano Lett.* **3,** 193-198 (2003)

[44] D. Wang, Y.-L. Chang, Q. Wang, J. Cao, D. B. Farmer, R. G. Gordon and H. Dai. Surface chemistry and electrical properties of germanium nanowires. *J. Am. Chem. Soc.* **126,** 11602-11611 (2004)

[45] M. Shur. Low ballistic mobility in submicron HEMTs. *IEEE Electron Device Lett.* **23,** 511-513 (2002)

[46] Z. Chen and J. Appenzeller. Mobility extraction and quantum capacitance impact in high performance graphene field-effect transistor devices. *IEEE IEDM Technical Digest* **21.1,** 509-512 (2008)

[47] M. Hjort. Ph.D. thesis, Lund University (2014)

[48] C. H. Hou, M. C. Chen, C. H. Chang, T. B. Wu, C. D. Chiang and J. J. Luo. Effects of Surface Treatments on Interfacial Self-Cleaning in Atomic Layer Deposition of Al_2O_3 on InSb. *J. Electrochem. Soc.* **155,** G180-G183 (2008)

[49] S. Chu, G. Wang, W. Zhou, Y. Lin, L. Chernyak, J. Zhao, J. Kong, L. Li, J. Ren and J. Liu. Electrically pumped waveguide lasing from ZnO nanowires. *Nature Nanotech.* **6,** 506-510 (2011)

4

Hard superconducting gap in InSb nanowires

Önder Gül, Hao Zhang, Folkert K. de Vries, Jasper van Veen, Kun Zuo, Vincent Mourik, Sonia Conesa-Boj, Michał P. Nowak, David J. van Woerkom, Marina Quintero-Pérez, Maja C. Cassidy, Attila Geresdi, Sebastian Koelling, Diana Car, Sébastien R. Plissard, Erik P.A.M. Bakkers, Leo P. Kouwenhoven

Topological superconductivity is a state of matter that can host Majorana modes, the building blocks of a topological quantum computer. Many experimental platforms predicted to show such a topological state rely on proximity-induced superconductivity. However, accessing the topological properties requires an induced hard superconducting gap, which is challenging to achieve for most material systems. We have systematically studied how the interface between an InSb semiconductor nanowire and a NbTiN superconductor affects the induced superconducting properties. Step by step, we improve the homogeneity of the interface while ensuring a barrier-free electrical contact to the superconductor and obtain a hard gap in the InSb nanowire. The magnetic field stability of NbTiN allows the InSb nanowire to maintain a hard gap and a supercurrent in the presence of magnetic fields (~ 0.5 Tesla), a requirement for topological superconductivity in one-dimensional systems. Our study provides a guideline to induce superconductivity in various experimental platforms such as semiconductor nanowires, two-dimensional electron gases and topological insulators, and holds relevance for topological superconductivity and quantum computation.

This chapter has been published in *Nano Letters* **17**, 2690 (2017).

4.1. Introduction

A topological superconductor can host non-Abelian excitations, the so-called Majorana modes forming the basis of topological quantum computation [1–6]. Both the non-Abelian property and the topological protection of Majoranas crucially rely on the energy gap provided by the superconducting pairing of electrons that separates the ground state from the higher energy excitations. For most material systems that can support such a topological state, pairing is artificially induced by proximity, where the host material is coupled to a superconductor in a hybrid device geometry [7–27]. Accessing the topological properties in hybrid devices requires a negligible density of states within the induced superconducting gap, *i.e.*, an induced hard gap, which can be attained by a homogeneous and barrier-free interface to the superconductor [28–32]. However, achieving such interfaces remains an outstanding challenge for many material systems, constituting a major bottleneck for topological superconductivity. Here we engineer a high-quality interface between semiconducting InSb nanowires and superconducting NbTiN resulting in an induced hard gap in the nanowire by improving the homogeneity of the hybrid interface while ensuring a barrier-free electrical contact to the superconductor. Our transport studies and materials characterization demonstrate that surface cleaning dictates the structural and electronic properties of the InSb nanowires, and determines the induced superconductivity together with the wetting of the superconductor on the nanowire surface. We show that both the induced gap and the supercurrent in the nanowire withstands magnetic fields (~ 0.5 Tesla), a requirement for topological superconductivity in one-dimensional systems.

InSb nanowires have emerged as a promising platform for topological superconductivity [7, 10, 11, 15, 16] owing to a large spin–orbit coupling [33, 34], a large g factor [35, 36], and a high mobility [36–39]. These ingredients, together with a high-quality interface to a magnetic field resilient s-wave superconductor, are necessary to maintain a finite topological gap in one dimension [4, 5, 40, 41]. The interface quality can be inferred using tunneling spectroscopy which resolves the induced superconducting gap for a tunnel barrier away from the interface. To date, tunneling spectroscopy studies on proximitized InSb nanowires have reported a significant density of states within the superconducting gap, a so-called soft gap, suggesting an inhomogeneous interface [7, 10, 11, 16]. These subgap states destroy the topological protection by allowing excitations with arbitrarily small energy. Soft gaps have been observed also in other hybrid systems for cases where tunneling spectroscopy is applicable [8, 12, 42, 43]. For other cases, interface inhomogeneity is indirectly inferred from a decreased excess current or supercurrent due to a deviation from Andreev transport [44], a common observation in hybrid systems [17, 18, 24]. A hard gap has recently been realized in epitaxial InAs–Al materials [29–32], and in Bi_2Se_3 [19] and Bi_2Te_3 [20, 21] epitaxially grown on $NbSe_2$, where the interface inhomogeniety can be minimized. However, these studies do not provide further insight into the soft gap problem in material systems for which either epitaxy remains a challenge or when a high structural quality does not guarantee a barrier-free interface (*e.g.* due to carrier depletion). Here we tackle the soft gap problem in InSb nanowire devices by focusing on the constituents of a hybrid device realization which are crucial for the interface.

4.2. Results

In general, realizing a hybrid device begins with surface preparation of the host material followed by the deposition of a superconductor. In host materials with low surface electron density or a small number of electronic subbands such as semiconductor nanowires, the correct surface preparation is of paramount importance to ensure a barrier-free coupling to the superconductor. Here we also adopt this procedure for our nanowires [45] whose native surface oxide forms an insulating layer that has to be removed. We describe the details of the nanowire growth, fabrication, and measurement setup in Supplementary Section 4.S.

Figure 4.1a and b show a completed device with two lithographically defined superconducting electrodes having a small separation (~ 150 nm) on an InSb nanowire. A degenerately doped silicon substrate acts as a global back gate, tuning the carrier density in the wire. The small electrode separation allows us to electrostatically define a tunnel barrier in the wire section between the electrodes by applying negative gate voltages. Figure 4.1c and e show the induced gaps measured by tunneling spectroscopy for two common realizations of an InSb nanowire hybrid device. For the device in Figure 4.1c, a sulfur-based solution [46] is used to clean the wire surface followed by evaporation of Ti/Al with Ti the wetting layer, whereas Figure 4.1e is from a device for which the wire surface is in situ cleaned using an argon plasma followed by sputtering of NbTiN. Figure 4.1d shows the conductance traces of the sulfur-Ti/Al device indicating a hard induced gap $2\Delta \sim 0.3$ meV for low gate voltages when decreased transmission suppresses Andreev reflection. In contrast, Figure 4.1f demonstrates that the argon-NbTiN device shows a soft induced gap even for the lowest gate voltages, but with a gap $2\Delta \sim 1$ meV inherited from NbTiN, a superconductor with a large gap and high critical field. Both device realizations present a challenge toward topological protection. In the first case, the magnetic field (~ 0.5 T) required to drive the wire into the topological state destroys the superconductivity of Al (Figure 4.S1). Al can withstand such fields when it is very thin (< 10 nm) in the field plane; however, such thin Al films contacting a nanowire have so far only been achieved by epitaxy [13, 14, 30]. In the NbTiN device prepared with argon cleaning, the subgap states render the topological properties experimentally inaccessible.

We now turn our attention to the surface of InSb nanowires prior to superconductor deposition. To determine the effects of surface cleaning on transport, we characterized long-channel nanowire devices with ~ 1 μm electrode separation where the channel surface is cleaned using different methods, along with control devices with pristine channels (details in Supplementary Section 4.S). Figure 4.2 shows the measured conductance through the nanowire as a function of gate voltage, with the traces representing an average over different devices and the shades indicating the standard deviation. We find that the argon-cleaned channel behaves strikingly different than sulfur-cleaned and pristine channels. First, the argon-cleaned channel does not pinch off, showing a finite conductance even for lowest gate voltages, indicating a deviation from a semiconducting gate response. Second, it shows a lower transconductance $\propto \mathrm{d}G/\mathrm{d}V_{\mathrm{gate}}$ compared to sulfur-cleaned and pristine channels indicating a low mobility. These observations are consistent with the formation of metallic In islands on the InSb surface after argon cleaning [47]. In contrast, the sulfur-cleaned channel shows a gate response similar to the pris-

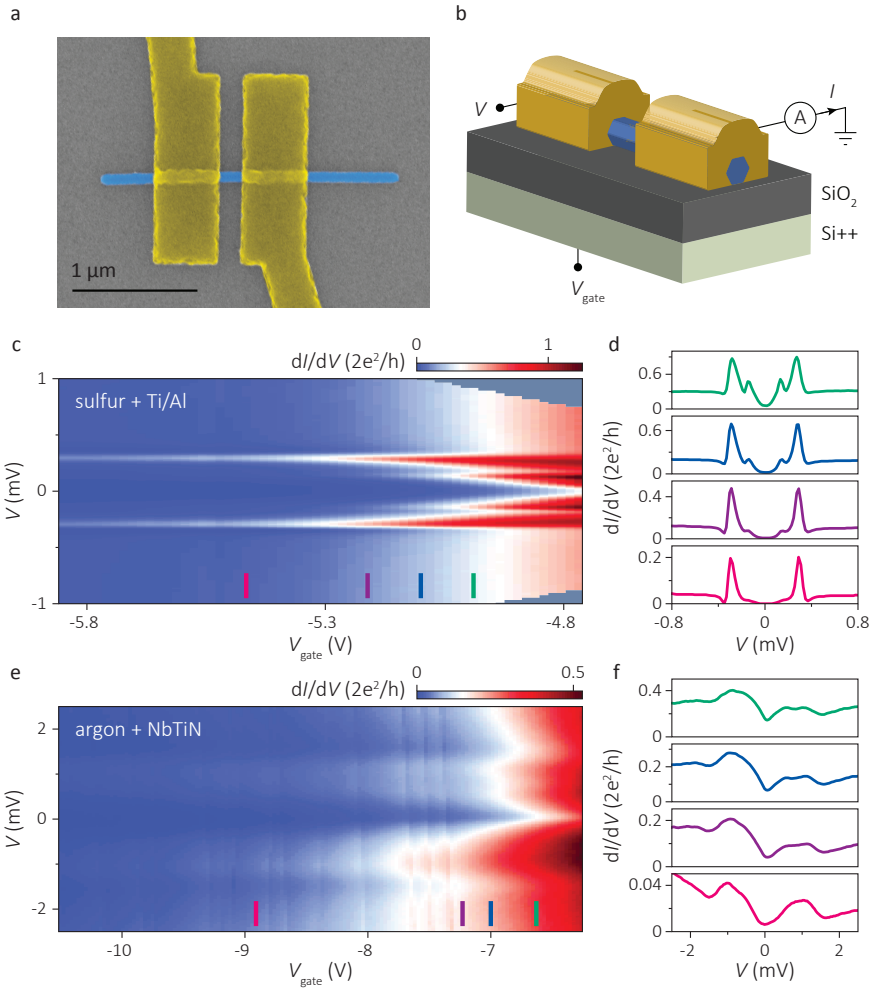

Figure 4.1 | InSb nanowire hybrid device and induced superconducting gaps for different device realizations. (a) Top-view false-color electron micrograph of a typical device consisting of an InSb nanowire (blue) with a diameter ~ 80 nm coupled to two superconducting electrodes (yellow) with ~ 150 nm separation. **(b)** Schematic of the devices and the measurement setup with bias voltage V, monitored current I, and the voltage V_{gate} applied on back gate (Si++ substrate) that is separated from the device by a 285 nm thick SiO_2 dielectric. **(c), (d)** Spectroscopy of a device realized using sulfur cleaning followed by evaporation of superconducting Ti/Al (5/130 nm) electrodes. $T = 250$ mK. Differential conductance $\mathrm{d}I/\mathrm{d}V$ is plotted as a function of bias voltage V for varying gate voltages V_{gate}. $\mathrm{d}I/\mathrm{d}V$ traces in (d) are vertical line cuts from (c) at gate voltages marked with colored bars. $\mathrm{d}I/\mathrm{d}V$ is symmetric around zero bias with two conductance peaks at $V \sim \pm 0.3$ mV seen for all gate voltages that result from the coherence peaks in the superconducting density of states at the edge of the induced gap Δ. For our device geometry with two superconducting electrodes $2\Delta \sim 0.3$ meV. For sufficiently low V_{gate}, where $\mathrm{d}I/\mathrm{d}V \ll 2e^2/h$ at above-gap bias ($V > 2\Delta$), tunnelling is weak, which suppresses the Andreev reflection probability revealing a hard induced gap. Larger gate voltages decrease the tunnel barrier height where increased Andreev reflection probability results in finite subgap conductance. **(e), (f)** Spectroscopy of a device realized using argon cleaning followed by sputtering of superconducting NbTiN (90 nm) electrodes. $T = 250$ mK. We find $2\Delta \sim 1$ meV, much larger than that of the Al-based InSb hybrid device shown above. $\mathrm{d}I/\mathrm{d}V$ traces in (f) show an above-gap conductance comparable to those in (d). The induced gap is soft with a non-vanishing subgap conductance even for the weak tunnelling regime at low V_{gate}, indicating a deviation from Andreev transport.

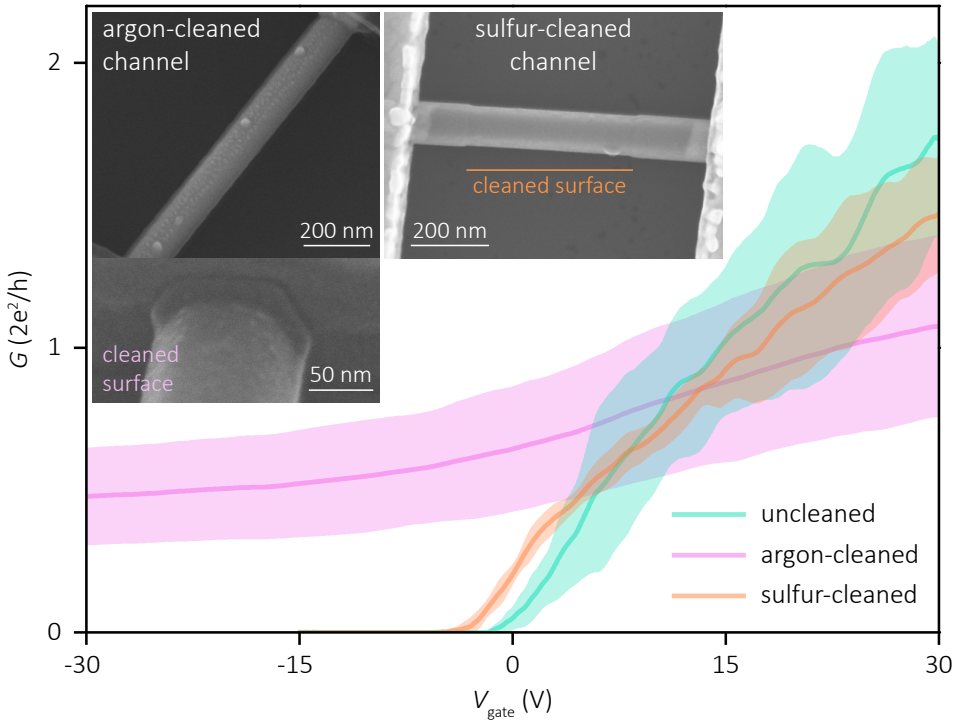

Figure 4.2 | Effects of different surface cleaning on transport properties. Gate voltage dependent conductance G of InSb nanowire devices with ~ 1 μm electrode separation (channel length) for argon-cleaned (pink), sulfur-cleaned (orange), and uncleaned pristine (cyan) channels. $T = 4$ K. Traces represent ensemble-averaged conductance over 6 (argon-cleaned), 3 (sulfur-cleaned), and 2 (uncleaned) different devices measured at bias voltage $V = 10$ mV, with the shades indicating the standard deviation (see the Supporting Information for the details of averaging). Argon-cleaned channels do not pinch off, a deviation from a semiconducting gate response, and show a low transconductance $\propto \mathrm{d}G/\mathrm{d}V_{\mathrm{gate}}$ indicating a low mobility. In contrast, sulfur-cleaned channels show a gate response similar to the pristine channel but with a shift of the threshold voltage toward negative values. Insets show high-resolution electron micrographs of argon- and sulfur-cleaned channels. Argon cleaning typically rounds the otherwise hexagonal cross section of the InSb nanowire (bottom image) and leaves a rough surface (top image). A sulfur cleaning yielding comparable contact resistances etches the InSb nanowire much less and leaves behind a smoother surface.

tine channel apart from a shift of the threshold voltage toward negative values. This behavior indicates a surface electron accumulation expected for III–V semiconductors treated with sulfur-based solutions [48–50]. A close inspection of the cleaned channels reveals clear differences in nanowire surface morphology after argon and sulfur cleaning (Figure 4.2 inset). While argon cleaning created a roughness easily discernible under high-resolution electron microscope for different plasma parameters, we find that sulfur cleaning, which removes ~ 5 nm of the wire, leaves a smoother InSb surface. TEM studies on the cleaned wire surface confirm this observation (Figure 4.S2). Comparable contact resistances between argon and sulfur cleaning were achievable (*e.g.* in Figure 4.1e and f) when the argon plasma significantly etches the nanowire surface (> 15 nm), while

different plasma parameters resulting in less etching gave consistently higher contact resistances. This indicates that a complete removal of the native oxide (~ 3 nm) does not guarantee a barrier-free interface to the superconductor for InSb nanowires, which could be related to the surface depletion of InSb previously reported for a (110) surface [51], the orientation of our nanowire facets. In the rest of the chapter we use sulfur cleaning to remove the native oxide on the nanowire surface prior to superconductor deposition.

Next, we investigate the wetting of the superconductor on the nanowire surface. Figure 4.3a shows the conductance averaged over different nanowire devices realized with and without a thin layer of NbTi (5 nm), a reactive metal deposited immediately before the NbTiN to ensure its wetting on the wire. The inclusion of a NbTi wetting layer substantially improves the contact resistance of the devices. Tunneling spectroscopy (Figure 3b-d) reveals the differences in superconducting properties of the devices with and without the wetting layer. Figure 4.3b shows an induced gap $2\Delta \sim 1$ meV for a device with NbTi wetting layer. Low gate voltages bring the device into the tunneling regime revealing a hard gap, shown in Figure 4.3c. In contrast, Figure 4.3d and e show that omitting the wetting layer results in no clearly identifiable induced gap and a tunneling conductance dominated by Coulomb blockade with irregular diamonds. Finally, to verify the importance of the wetting of the superconductor on the wire surface we realized InSb–Al nanowire devices without a Ti wetting layer. These devices also showed very high contact resistances, while the inclusion of Ti wetting layer gave low contact resistances and a finite supercurrent (Figure 4.S3), in addition to a hard gap shown in Figure 4.1c and d. In Supplementary Section 4.S we comprehensively discuss our observations related to the improvement due to inclusion of a wetting layer.

The devices prepared with sulfur cleaning and NbTi/NbTiN electrodes in Figure 4.3 did not show a supercurrent, a requirement for a nanowire-based topological quantum bit [52–55]. We attribute the lack of a supercurrent to a residual interface barrier effective at small bias. This could be related to the ex situ nature of sulfur cleaning, leaving the wire surface exposed to ambient which cannot exclude adsorbents at the interface. To improve the small bias response of our devices, we perform an additional in situ argon cleaning of sufficiently low power to avoid a damage to the InSb nanowire surface. After including this low-power argon cleaning, we find a high yield of devices showing a finite supercurrent measured at 250 mK (Figure 4.S4). For another chip with 18 nanowire devices but measured at 50 mK, we find a clear supercurrent for all devices (Figure 4.S5) while obtaining an induced gap $2\Delta \sim 1$ meV or larger (Figure 4.S6 and 4.S9).

Finally we study the magnetic field response of the optimized hybrid devices combining sulfur cleaning followed by an in situ low-power argon cleaning, and NbTi/NbTiN superconducting electrodes. Figure 4.4a and b show the differential conductance for varying gate voltages at zero magnetic field measured at 50 mK (details in Figure 4.S6). We find a hard gap $2\Delta \sim 1.5$ meV which confirms the noninvasiveness of our low-power cleaning. The extracted conductance suppression at small bias compared to the above-gap conductance at large bias is ~ 100 (Figure 4.S7). Next, we choose a gate voltage where the device is in the tunneling regime (orange trace in Figure 4.4b) and perform spectroscopy for increasing magnetic fields along the wire axis, shown in Figure 4.4c. In Figure 4.4d we plot the conductance traces taken at different magnetic fields showing an induced gap which remains hard up to ~ 0.5 T (see Figure 4.S8 for a logarithmic plot). In-

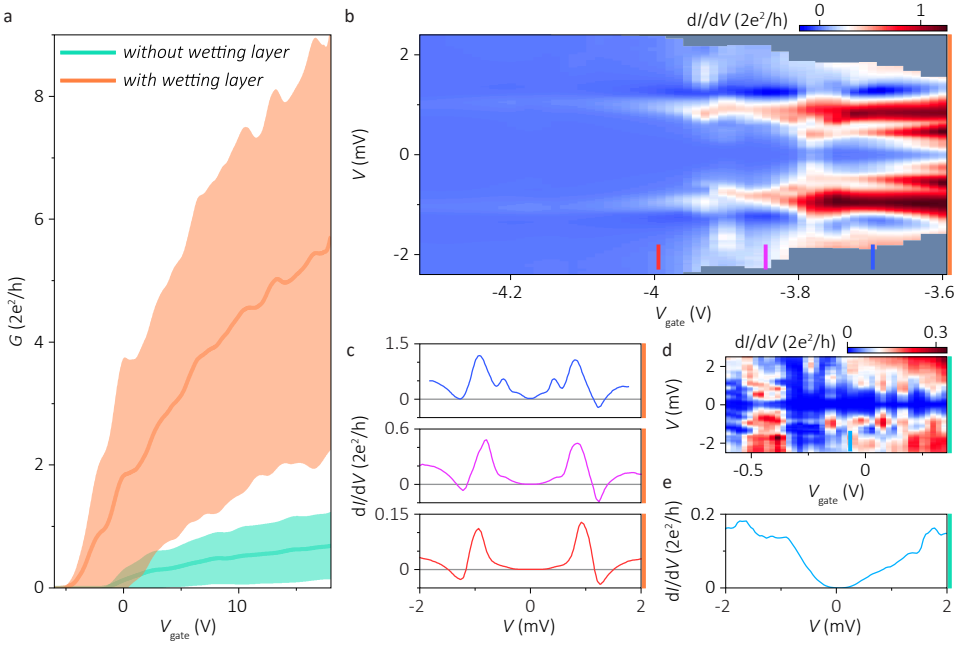

Figure 4.3 | Effects of wetting layer on the transport and superconducting properties. **(a)** Gate voltage dependent conductance G of InSb nanowires devices with ~ 150 nm electrode separation realized with and without including a NbTi (5 nm) wetting layer between the nanowire and NbTiN (90 nm) electrodes. Native oxide on the nanowire surface is removed by sulfur cleaning prior to the deposition of the electrodes. Traces represent ensemble-averaged conductance over 4 (NbTi/NbTiN) and 7 (NbTiN) different devices measured at a bias voltage $V = 10$ mV, with the shades indicating the standard deviation (see the Supporting Information for the details of averaging). Inclusion of a NbTi wetting layer decreases the average contact resistance (including both contacts) from ~ 100 kΩ to ~ 1.6 kΩ (see the Supporting Information for the extraction of contact resistance). **(b), (c)** Spectroscopy of a device realized with NbTi/NbTiN electrodes. Differential conductance $\mathrm{d}I/\mathrm{d}V$ is plotted as a function of bias voltage V for varying gate voltages V_{gate}. $\mathrm{d}I/\mathrm{d}V$ traces in (c) are vertical line cuts from (b) at gate voltages marked with colored bars. $\mathrm{d}I/\mathrm{d}V$ is symmetric in bias with two peaks at $V \sim \pm 1$ mV seen for all gate voltages from which we find $2\Delta \sim 1$ meV. For low V_{gate} and away from quantum dot resonances the subgap conductance vanishes, revealing a hard induced gap. Larger gate voltages decrease the tunnel barrier height, where increased Andreev reflection probability results in finite subgap conductance. **(d)** Spectroscopy of a device realized with NbTiN electrodes without a NbTi wetting layer. The tunneling conductance is dominated by Coulomb blockade with irregular diamonds. An induced gap cannot be clearly identified. **(e)** A vertical line cut from (d) at $V_{\mathrm{gate}} \sim -0.08$ V (indicated by a blue bar) with a conductance similar to the middle panel in (c). $\mathrm{d}I/\mathrm{d}V$ is not symmetric in bias and coherence peaks are not visible. All data in this figure taken at $T = 250$ mK.

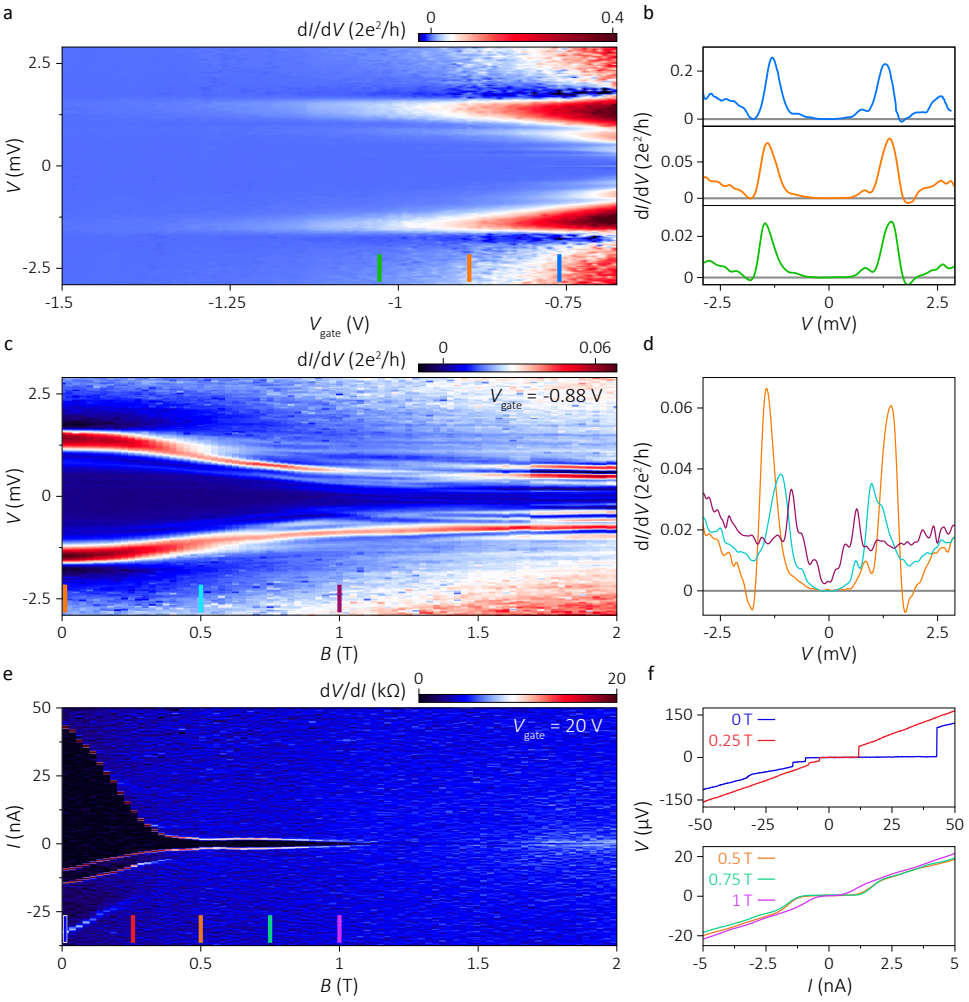

Figure 4.4 | Tunneling spectroscopy and magnetic field response of InSb nanowire hybrid devices with engineered interface. (a), (b) Spectroscopy of a device realized with NbTi/NbTiN electrodes using sulfur cleaning followed by an in situ low-power argon cleaning. Differential conductance $\mathrm{d}I/\mathrm{d}V$ is plotted as a function of bias voltage V for varying gate voltages V_{gate}. $\mathrm{d}I/\mathrm{d}V$ traces in (b) are vertical line cuts from (a) at gate voltages marked with colored bars. $\mathrm{d}I/\mathrm{d}V$ is symmetric in bias with two peaks at $V \sim \pm 1.5$ mV seen for all gate voltages from which we find $2\Delta \sim 1.5$ meV. The induced gap is hard with vanishing subgap conductance in the tunneling regime. **(c), (d)** $\mathrm{d}I/\mathrm{d}V$ of the same device is plotted as a function of bias voltage V for an increasing magnetic field B along the nanowire. Gate voltage is set to $V_{\mathrm{gate}} = -0.88$ V, the same as in the middle panel in (b). $\mathrm{d}I/\mathrm{d}V$ traces in (d) are vertical line cuts from (c) at magnetic fields marked with colored bars. The induced gap remains hard up to ~ 0.5 T. Increasing fields decrease the induced gap size and increase the subgap conductance but induced superconductivity persists up to 2 T where $\mathrm{d}I/\mathrm{d}V$ shows a gap feature with suppressed conductance at small bias and symmetrically positioned coherence peaks. **(e)** Differential resistance $\mathrm{d}V/\mathrm{d}I$ of an identical device is plotted as a function of bias current I for an increasing magnetic field B along the nanowire. Dark regions with vanishing resistance indicate the supercurrent which remains finite up to 1 T. Gate voltage $V_{\mathrm{gate}} = 20$ V. **(f)** Current-voltage traces from (e) at magnetic fields marked with colored bars. We find a switching current of ~ 40 nA at zero magnetic field, which decreases to ~ 10 nA at 0.25 T, and to ~ 0.5 nA at 1 T. Both devices in this figure have an electrode separation of ~ 150 nm. Data taken at $T = 50$ mK.

creasing fields decrease the induced gap size and increase the subgap conductance, but a gap feature can be identified up to 2 T revealing the large critical field of NbTiN. Figure 4.4e and f show the critical current of another device as a function of magnetic field, measured at a large gate voltage when the nanowire is highly conducting (details in Figure 4.S9). We find a critical current of ~ 40 nA at zero magnetic field which remains finite up to greater than 1 T. The nonmonotonous magnetic-field evolution of the critical current can be accounted for using a model which includes the Zeeman effect, spin–orbit coupling, and a realistic nanowire geometry in the few-channel, quasi-ballistic regime—the transport regime of our devices [56].

In conclusion, we have developed a method of obtaining a hard induced gap and supercurrent in InSb nanowires in the presence of magnetic fields (~ 0.5 Tesla) by combining a noninvasive nanowire surface cleaning together with a wetting layer between the nanowire and the NbTiN superconductor. Our results provide a guideline for inducing superconductivity in semiconductor nanowires, two-dimensional electron gases and topological insulators, and hold relevance for topological superconductivity in various material systems.

4.S. Supplementary Information

Nanowire growth and device fabrication. InSb nanowires have been grown by Au-catalyzed Vapor-Liquid-Solid mechanism in a Metal Organic Vapor Phase Epitaxy reactor. The InSb nanowire crystal direction is [111] zinc blende, free of stacking faults and dislocations [45]. Nanowires are deposited one-by-one using a micro-manipulator [57] on a p-Si++ substrate covered with 285 nm thick SiO_2 serving as a dielectric for back gate. Superconductor deposition process starts with resist development followed by oxygen plasma cleaning. For sulfur cleaning, the chip is immersed in a Sulfur-rich ammonium sulfide solution diluted by water (with a ratio of 1:200) at 60°C for half an hour [46]. At all stages care is taken to expose the solution to air as little as possible. Ti/Al contacts are e-beam evaporated at a base pressure $< 10^{-7}$ mbar. In situ argon plasma cleaning and NbTiN deposition is performed in an AJA International ATC 1800 sputtering system with a base pressure ~ 10^{-9} Torr. For devices without sulfur cleaning, argon cleaning is performed using an argon plasma typically at a pressure of 3 mTorr and a power of 100 Watts applied for 150 seconds, but different plasma parameters removing a similar thickness of InSb from the nanowire surface (> 15 nm) gave similar transport properties. For devices with sulfur cleaning we used a much milder argon plasma at a pressure of 10 mTorr and a power of 25 Watts applied for ~ 5 seconds. For NbTiN deposition a $Nb_{0.7}Ti_{0.3}$ wt. % target with a diameter of 3 inches is used. Reactive sputtering resulting in (NbTi) NbTiN films was performed in an Ar/N process gas with (0) 8.3 at. % nitrogen content at a pressure of 2.5 mTorr using a dc magnetron sputter source at a power of 250 Watts. An independent characterization of the NbTiN films gave a critical temperature of 13.5 K for 90 nm thick films with a resistivity of 114 $\mu\Omega$·cm and a compressive stress on Si substrate.

Fabrication details of the long-channel devices in Figure 4.2. For the InSb nanowire devices with sulfur-cleaned channels, the cleaning of the channel is performed after a complete fabrication of the electrodes contacting the nanowire. For the devices whose

transport data is presented, sulfur cleaning is applied to the entire channel, while the inset shows a partially cleaned channel to illustrate the mild etching of the wire. For the nanowire devices with argon-cleaned channels, the cleaning of the channel is performed before the fabrication of the contact electrodes. However, we obtained a similar result when argon cleaning was applied after fabricating the contacts. For all long-channel devices we used argon cleaning to remove the native oxide on the nanowire surface prior to contact deposition.

Measurement setup. All the data in this study is measured using RC, copper powder, and π filters thermalized at different temperatures. Differential conductance measurements are performed using standard ac lock-in techniques. Nanowire devices are kept in vacuum during low temperature measurements.

Details of ensemble averaging. Conductance is averaged over different nanowire devices for each value of gate voltage. Devices within an ensemble are fabricated simultaneously on a single substrate, have identical geometries, and are measured during the same cool down.

Extraction of contact resistance. We extract contact resistances by fitting the conductance measured as a function of gate voltage using the method described in Ref. [37]. Here we leave the product of capacitance and mobility as a free fit parameter which is not taken into consideration.

Discussion of the wetting layer. Throughout our study we have tried various etching techniques (HF, lactic acid, sulfur solution, He ion beam, Ar plasma) in combination with different contact materials (Ti, Al, V, Cr - evaporation; Al, NbTi, NbTiN, MoRe - sputtering). Our observations rule out a work function (W) related explanation for the improvement due to inclusion of a wetting layer: Ti ($W = 4.33$ eV) [58] and Cr ($W = 4.5$ eV) [58] gives significantly lower contact resistances on our wires than Al ($W = 4.06 - 4.26$ eV) [58]—known for its low work function. (See Ref. [36] for Cr/Au contacts on our wires.) Consistent observation of the improvement due to wetting layer both for evaporation (Al) and for reactive sputtering (NbTiN) suggests that the mechanism of improvement is independent of the details of the deposition environment, such as nitrogen plasma. We further note that sputtered Al contacts also result in low contact transparency with large contact resistances (no difference observed between evaporated and sputtered Al contacts without a wetting layer). Finally, a Ti wetting layer provides improvement for Al contacts on InAs nanowires as well [29]—consistent with our observations. However, it is possible to realize transparent contacts of Al on InAs when the Al–InAs interface is homogeneous (epitaxial) [29]. This suggests that the nucleation of the Al film deposited on the wire is a key factor which determines the transparency.

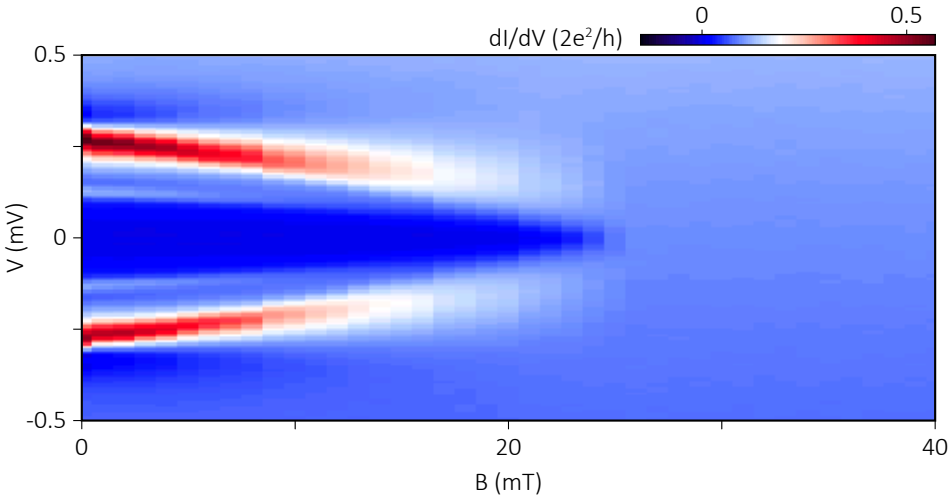

Figure 4.S1 | Magnetic field response of the induced gap in InSb nanowire hybrid device with Ti/Al electrodes. Differential conductance $\mathrm{d}I/\mathrm{d}V$ is plotted as a function of bias voltage V for increasing magnetic field B along the nanowire axis. The nanowire device is in the tunneling regime with $\mathrm{d}I/\mathrm{d}V \ll 2e^2/h$ for above-gap bias ($V > 2\Delta$). At zero magnetic field $\mathrm{d}I/\mathrm{d}V$ shows two conductance peaks at $V \sim \pm 0.3$ mV symmetric around zero bias giving $2\Delta \sim 0.3$ meV. Increasing the magnetic field decreases the size of the superconducting gap Δ which completely vanishes at ~ 25 mT. The device shows no superconductivity at larger magnetic fields. Device realized by sulfur cleaning. Ti/Al electrodes have a thickness of 5/130 nm and a separation of ~ 150 nm on the nanowire. $T = 50$ mK.

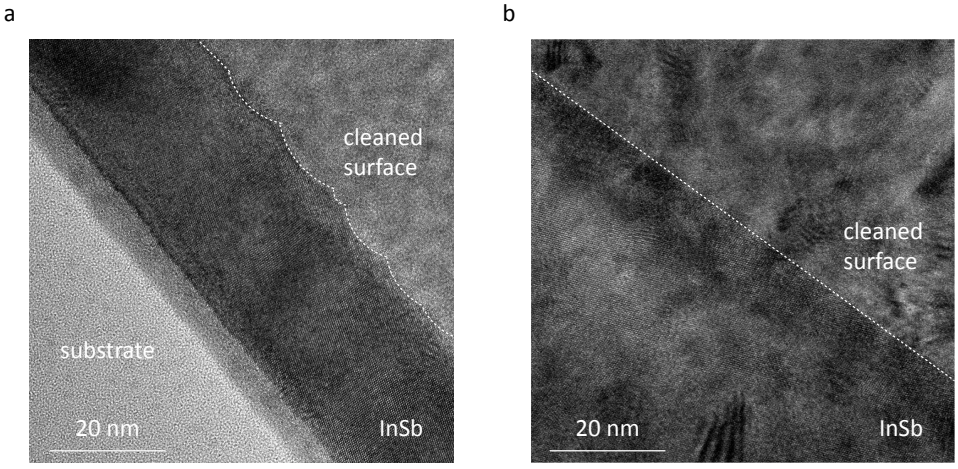

Figure 4.S2 | Cross-sectional transmission electron micrographs of the nanowire surface cleaned using different methods. The cuts were performed along the nanowire axis. **(a)** InSb nanowire surface after argon plasma cleaning. Argon cleaning leaves a rough nanowire surface. Nanowire appears thinner due to substantial etching. **(b)** InSb nanowire surface after sulfur cleaning followed by a low-power argon cleaning (see main text for details). Sulfur cleaning leaves a smoother nanowire surface.

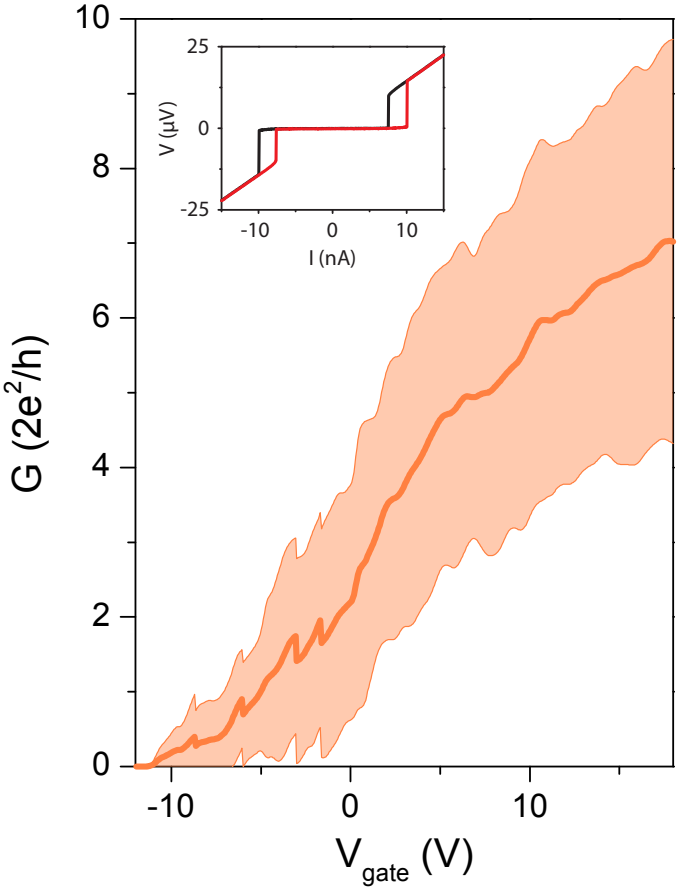

Figure 4.S3 | Additional transport properties of InSb nanowire hybrid devices with Ti/Al electrodes. Conductance G of InSb nanowire devices is plotted as a function of gate voltage V_{gate}. The trace represents ensemble-averaged conductance over 6 different devices on a single chip and the shade indicates the standard deviation. Taken at a bias voltage $V = 10$ mV. Average contact resistance (including both contacts) is ~ 1 kΩ. Inset shows voltage drop V as a function of bias current I for one of the 6 devices. We find a clear supercurrent up to ~ 10 nA. Red trace shows the current-voltage response when the bias current is swept in positive direction, black trace the negative direction. Gate voltage is set to $V_{\text{gate}} = 9$ V. Ti/Al electrodes have a thickness of 5/130 nm and a separation of ~ 150 nm on the nanowire. All data in this figure taken at $T = 250$ mK.

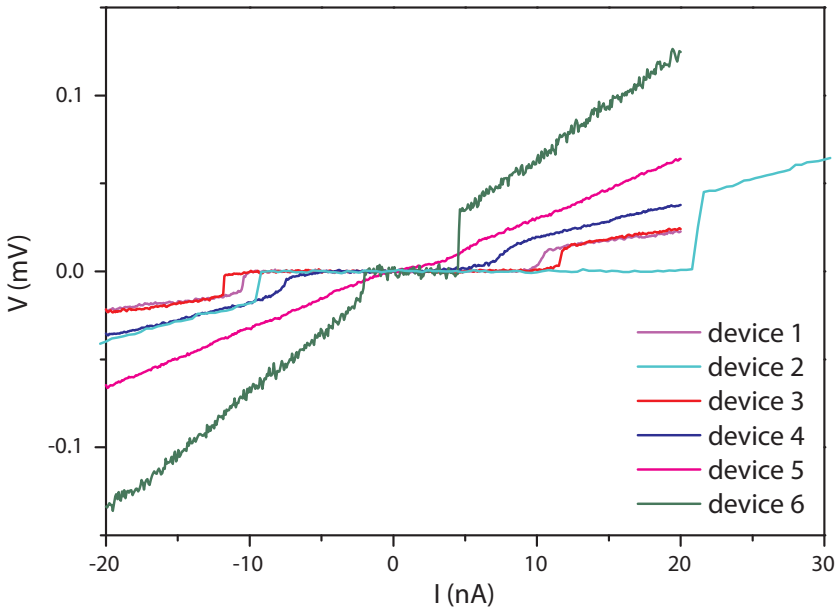

Figure 4.S4 | Supercurrent in InSb nanowire hybrid devices with NbTi/NbTiN electrodes. Devices realized using sulfur cleaning followed by an in situ low-power argon cleaning. $T = 250$ mK. Voltage drop V is plotted as a function of bias current I for different devices on a single chip with 8 devices in total. An in situ low-power argon cleaning improves the small bias response allowing to resolve a supercurrent for a high yield of devices. Gate voltage is set to $V_{\text{gate}} = 18$ V. NbTi/NbTiN electrodes have a thickness of 5/90 nm and a separation of ~ 150 nm on the nanowire.

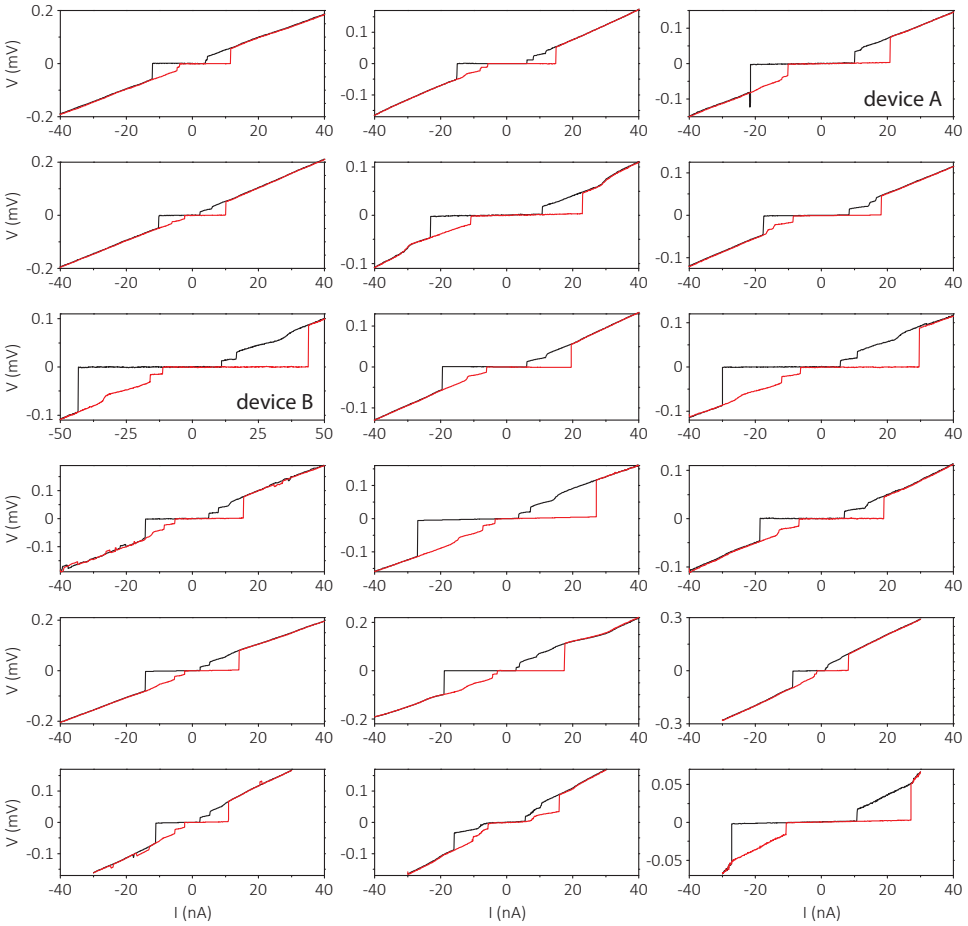

Figure 4.S5 | Supercurrent in InSb nanowire hybrid devices with NbTi/NbTiN electrodes at T = 50 mK. Devices realized using sulfur cleaning followed by an in situ low-power argon cleaning. Voltage drop V is plotted as a function of bias current I for all devices on a single chip. We find a clear supercurrent in every device. Red traces show the current-voltage response when the bias current is swept in positive direction, black traces the negative direction. We relate the origin of the hysteresis to electron heating [59]. Gate voltage is set to $V_{\text{gate}} = 20$ V. NbTi/NbTiN electrodes have a thickness of 5/90 nm and a separation of ~ 150 nm on the nanowire. Data in Figure 4.4a-d is taken from Device A, data in Figure 4.4e,f taken from Device B.

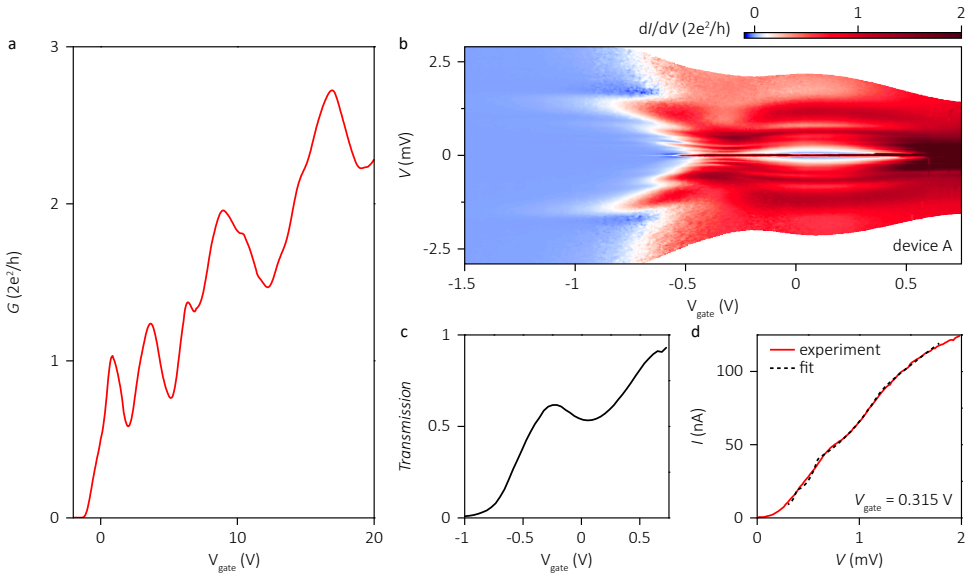

Figure 4.S6 | Additional transport properties of InSb nanowire hybrid device with engineered interface (device A). All data in this figure is taken from device A, the device in Figure 4.4a-d. **(a)** Conductance G of InSb nanowire device is plotted as a function of gate voltage V_{gate}, taken at a bias voltage $V = 10$ mV. Extracted contact resistance (including both contacts) $\sim 1.6\,\text{k}\Omega$. **(b)** Differential conductance $\text{d}I/\text{d}V$ is plotted as a function of bias voltage V for a large gate voltage V_{gate} range. **(c)** Transmission T extracted from (b) by fitting the measured current I using Averin-Bardas model [60, 61]. Best fit is obtained for a single channel transport through the nanowire. Transmission reaches ~ 0.9 giving a lower bound on contact transparency assuming a single channel transport. We note that our model does not account for the observed finite contact transparencies and conductance resonances, decreasing the certainty of our estimate. **(d)** The measured current I and the corresponding fit is plotted for $V_{\text{gate}} = 0.315$ V.

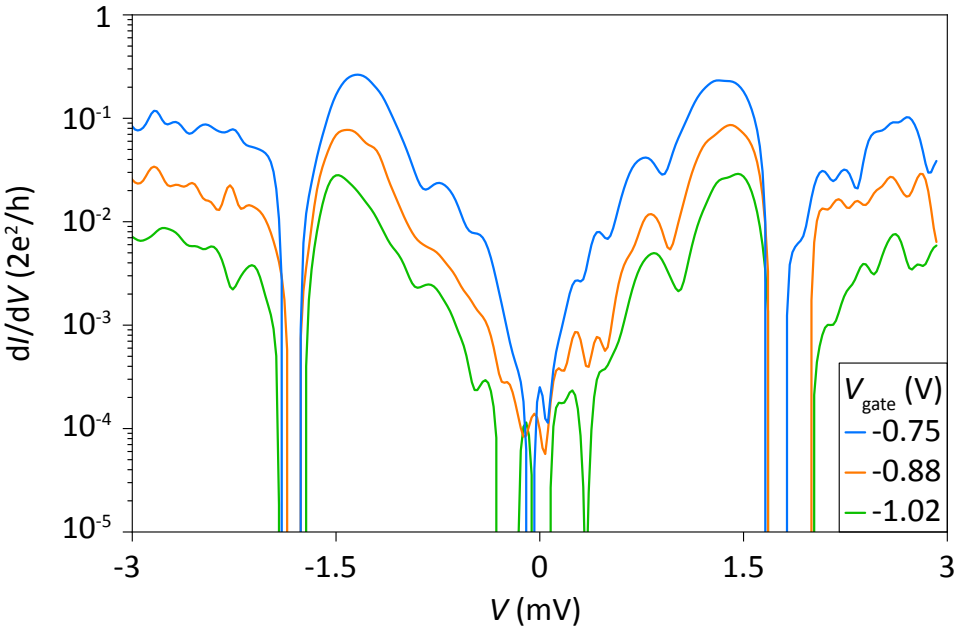

Figure 4.S7 | Figure 4.4b replotted in logarithmic conductance scale. Differential conductance $\mathrm{d}I/\mathrm{d}V$ is plotted as a function of bias voltage V for varying gate voltages V_{gate}. The extracted conductance suppression at small bias compared to the above-gap conductance at large bias is ~ 100.

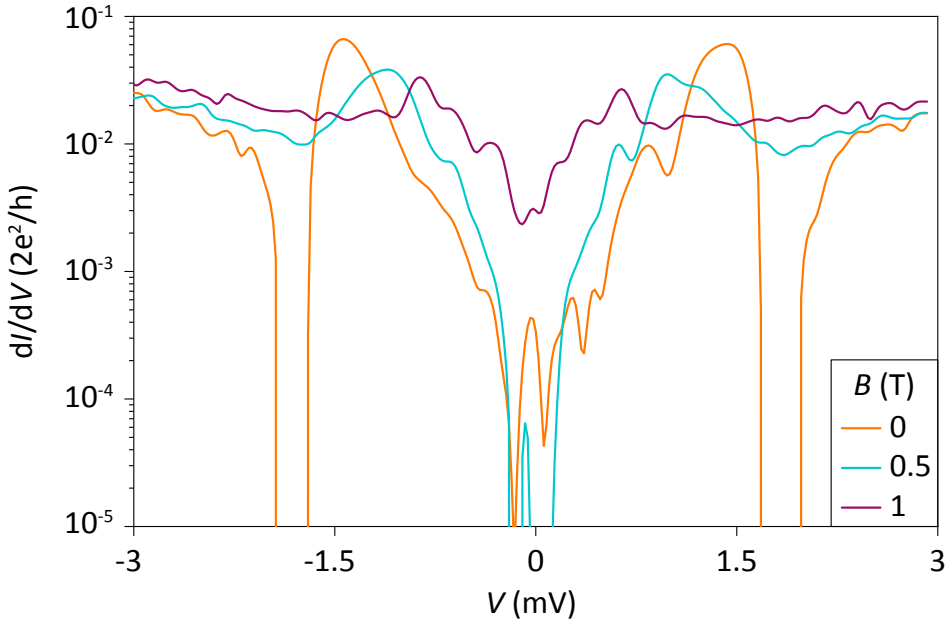

Figure 4.S8 | Figure 4.4d replotted in logarithmic conductance scale. Differential conductance $\mathrm{d}I/\mathrm{d}V$ is plotted as a function of bias voltage V for varying magnetic fields B along the wire axis. The induced gap remains hard up to ~ 0.5 T.

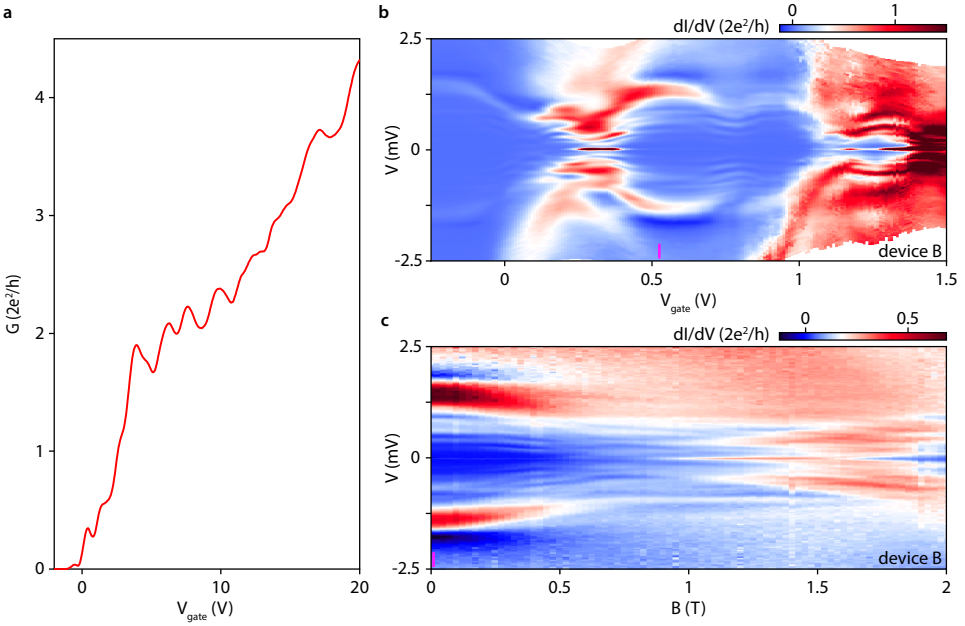

Figure 4.S9 | Additional transport properties of InSb nanowire hybrid device with engineered interface (device B). All data in this figure is taken from device B, the device in Figure 4.4e,f. **(a)** Conductance G of InSb nanowire device is plotted as a function of gate voltage V_{gate}, taken at a bias voltage $V = 10$ mV. Extracted contact resistance (including both contacts) ~ 1.2 kΩ. **(b)** Differential conductance $\mathrm{d}I/\mathrm{d}V$ is plotted as a function of bias voltage V for varying gate voltages V_{gate}. Differential conductance shows quantum dot features similar to those previously reported for InSb nanowires [62]. Further, we find subgap conductance peaks running through consecutive Coulomb valleys which we attribute to Andreev bound states in the wire section underneath the superconducting electrodes [14]. For our device geometry with a back gate controlling both the conductance in the wire section between the electrodes as well as the occupation in the wire section underneath the electrodes, it is not possible to tune the device away from the subgap states while maintaining the tunnelling regime necessary for spectroscopy. **(c)** Differential conductance $\mathrm{d}I/\mathrm{d}V$ is plotted as a function of bias voltage V for an increasing magnetic field B along the nanowire. V_{gate} ~ 0.5 V indicated with a pink bar in (b). Increasing magnetic fields bring the subgap states to lower energies resulting in a finite subgap conductance for $B > 0.3$ Tesla, similar to a previous report [14] but at a relatively lower magnetic field.

Acknowledgement

We thank S. Goswami and J. Shen for stimulating discussions and critical reading of the manuscript, and D.B. Szombati for assistance in device fabrication. This work has been supported by the Netherlands Organisation for Scientific Research (NWO), Foundation for Fundamental Research on Matter (FOM), European Research Council (ERC), Office of Naval Research (ONR N00014-16-1-2270), and Microsoft Corporation Station Q.

Author contributions

ÖG, FKdV, KZ, and VM developed the noninvasive surface cleaning and the inclusion of wetting layer. ÖG, HZ, and JvV optimized the noninvasive surface cleaning. SCB did the TEM analysis. MPN did the theoretical analysis. DJvW contributed to device fabrication. MQP and MCC optimized the NbTiN films. AG contributed to the data analysis. SK prepared the lamellae for TEM analysis. DC, SRP, and EPAMB grew the InSb nanowires. ÖG wrote the manuscript with contributions from all authors. LPK supervised the project.

References

[1] Read, N.; Green, D. *Phys. Rev. B* **2000**, *61*, 10267

[2] Kitaev, A. Y. *Phys.-Usp.* **2001**, *44*, 131–136

[3] Fu, L.; Kane, C. L. *Phys. Rev. Lett.* **2008**, *100*, 096407

[4] Oreg, Y.; Refael, G.; von Oppen, F. *Phys. Rev. Lett.* **2010**, *105*, 177002

[5] Lutchyn, R. M.; Sau, J. D.; Sarma, S. D. *Phys. Rev. Lett.* **2010**, *105*, 077001

[6] Alicea, J.; Oreg, Y.; Refael, G.; von Oppen, F.; Fisher, M. P. *Nat. Phys.* **2011**, *7*, 412–417

[7] Mourik, V.; Zuo, K.; Frolov, S. M.; Plissard, S.; Bakkers, E.; Kouwenhoven, L. *Science* **2012**, *336*, 1003–1007

[8] Das, A.; Ronen, Y.; Most, Y.; Oreg, Y.; Heiblum, M.; Shtrikman, H. *Nat. Phys.* **2012**, *8*, 887–895

[9] Rokhinson, L. P.; Liu, X.; Furdyna, J. K. *Nat. Phys.* **2012**, *8*, 795–799

[10] Deng, M. T.; Yu, C. L.; Huang, G. Y.; Larsson, M.; Caroff, P.; Xu, H. Q. *Nano Lett.* **2012**, *12*, 6414–6419

[11] Churchill, H. O. H.; Fatemi, V.; Grove-Rasmussen, K.; Deng, M. T.; Caroff, P.; Xu, H. Q.; Marcus, C. M. *Phys. Rev. B* **2013**, *87*, 241401

[12] Finck, A. D. K.; Van Harlingen, D. J.; Mohseni, P. K.; Jung, K.; Li, X. *Phys. Rev. Lett.* **2013**, *110*, 126406

[13] Albrecht, S.; Higginbotham, A.; Madsen, M.; Kuemmeth, F.; Jespersen, T.; Nygård, J.; Krogstrup, P.; Marcus, C. *Nature* **2016**, *531*, 206–209

[14] Deng, M. T.; Vaitiekenas, S.; Hansen, E. B.; Danon, J.; Leijnse, M.; Flensberg, K.; Nygård, J.; Krogstrup, P.; Marcus, C. M. *Science* **2016**, *354*, 1557–1562

[15] Zhang, H.; Gül, Ö.; Conesa-Boj, S.; Zuo, K.; Mourik, V.; de Vries, F. K.; van Veen, J.; van Woerkom, D. J.; Nowak, M. P.; Wimmer, M. et al. **2016**, arXiv:1603.04069

[16] Chen, J.; Yu, P.; Stenger, J.; Hocevar, M.; Car, D.; Plissard, S. R.; Bakkers, E. P. A. M.; Stanescu, T. D.; Frolov, S. M. **2016**, arXiv:1610.04555

[17] Hart, S.; Ren, H.; Wagner, T.; Leubner, P.; Mühlbauer, M.; Brüne, C.; Buhmann, H.; Molenkamp, L. W.; Yacoby, A. *Nat. Phys.* **2014**, *10*, 638–643

[18] Pribiag, V. S.; Beukman, A. J.; Qu, F.; Cassidy, M. C.; Charpentier, C.; Wegscheider, W.; Kouwenhoven, L. P. *Nat. Nanotechnol.* **2015**, *10*, 593–597

[19] Wang, M.-X.; Liu, C.; Xu, J.-P.; Yang, F.; Miao, L.; Yao, M.-Y.; Gao, C. L.; Shen, C.; Ma, X.; Chen, X. et al. *Science* **2012**, *336*, 52–55

[20] Xu, J.-P.; Liu, C.; Wang, M.-X.; Ge, J.; Liu, Z.-L.; Yang, X.; Chen, Y.; Liu, Y.; Xu, Z.-A.; Gao, C.-L. et al. *Phys. Rev. Lett.* **2014**, *112*, 217001

[21] Xu, J.-P.; Wang, M.-X.; Liu, Z. L.; Ge, J.-F.; Yang, X.; Liu, C.; Xu, Z. A.; Guan, D.; Gao, C. L.; Qian, D. et al. *Phys. Rev. Lett.* **2015**, *114*, 017001

[22] Williams, J. R.; Bestwick, A. J.; Gallagher, P.; Hong, S. S.; Cui, Y.; Bleich, A. S.; Analytis, J. G.; Fisher, I. R.; Goldhaber-Gordon, D. *Phys. Rev. Lett.* **2012**, *109*, 056803

[23] Wiedenmann, J.; Bocquillon, E.; Deacon, R. S.; Hartinger, S.; Herrmann, O.; Klapwijk, T. M.; Maier, L.; Ames, C.; Brüne, C.; Gould, C. et al. *Nat. Commun.* **2016**, *7*, 10303

[24] Bocquillon, E.; Deacon, R. S.; Wiedenmann, J.; Leubner, P.; Klapwijk, T. M.; Brüne, C.; Ishibashi, K.; Buhmann, H.; Molenkamp, L. W. *Nat. Nanotechnol.* **2017**, *12*, 137–143

[25] Wan, Z.; Kazakov, A.; Manfra, M. J.; Pfeiffer, L. N.; West, K. W.; Rokhinson, L. P. *Nat. Commun.* **2015**, *6*, 7426

[26] Pientka, F.; Keselman, A.; Berg, E.; Yacoby, A.; Stern, A.; Halperin, B. I. *Phys. Rev. X* **2017**, **7**, 021032

[27] Hell, M.; Leijnse, M.; Flensberg, K. *Phys. Rev. Lett.* **2017**, *118*, 107701

[28] Takei, S.; Fregoso, B. M.; Hui, H.-Y.; Lobos, A. M.; Sarma, S. D. *Phys. Rev. Lett.* **2013**, *110*, 186803

[29] Chang, W.; Albrecht, S.; Jespersen, T.; Kuemmeth, F.; Krogstrup, P.; Nygård, J.; Marcus, C. *Nat. Nanotechnol.* **2015**, *10*, 232–236

[30] Krogstrup, P.; Ziino, N.; Chang, W.; Albrecht, S.; Madsen, M.; Johnson, E.; Nygård, J.; Marcus, C.; Jespersen, T. *Nat. Mater.* **2015**, *14*, 400–406

[31] Kjaergaard, M.; Nichele, F.; Suominen, H.; Nowak, M.; Wimmer, M.; Akhmerov, A.; Folk, J.; Flensberg, K.; Shabani, J.; Palmstrøm, C. et al. *Nat. Commun.* **2016**, *7*, 12841

[32] Shabani, J.; Kjaergaard, M.; Suominen, H. J.; Kim, Y.; Nichele, F.; Pakrouski, K.; Stankevic, T.; Lutchyn, R. M.; Krogstrup, P.; Feidenhans'l, R. et al. *Phys. Rev. B* **2016**, *93*, 155402

[33] van Weperen, I.; Tarasinski, B.; Eeltink, D.; Pribiag, V. S.; Plissard, S. R.; Bakkers, E. P. A. M.; Kouwenhoven, L. P.; Wimmer, M. *Phys. Rev. B* **2015**, *91*, 201413

[34] Kammhuber, J.; Cassidy, M. C.; Pei, F.; Nowak, M. P.; Vuik, A.; Gül, Ö.; Car, D.; Plissard, S. R.; Bakkers, E. P. A. M.; Wimmer, M.; Kouwenhoven, L. P. **2017**, arXiv:1701.06878

[35] van Weperen, I.; Plissard, S. R.; Bakkers, E. P. A. M.; Frolov, S. M.; Kouwenhoven, L. P. *Nano Lett.* **2012**, *13*, 387–391

[36] Kammhuber, J.; Cassidy, M. C.; Zhang, H.; Gül, Ö.; Pei, F.; de Moor, M. W. A.; Nijholt, B.; Watanabe, K.; Taniguchi, T.; Car, D. et al. *Nano Lett.* **2016**, *16*, 3482–3486

[37] Gül, Ö.; van Woerkom, D. J.; van Weperen, I.; Car, D.; Plissard, S. R.; Bakkers, E. P. A. M.; Kouwenhoven, L. P. *Nanotechnology* **2015**, *26*, 215202

[38] Li, S.; Kang, N.; Fan, D.; Wang, L.; Huang, Y.; Caroff, P.; Xu, H. *Sci. Rep.* **2016**, *6*, 24822

[39] Gill, S.; Damasco, J.; Car, D.; Bakkers, E. P. A. M.; Mason, N. *Appl. Phys. Lett.* **2016**, *109*, 233502

[40] Potter, A. C.; Lee, P. A. *Phys. Rev. B* **2011**, *83*, 184520

[41] Sau, J. D.; Tewari, S.; Sarma, S. D. *Phys. Rev. B* **2012**, *85*, 064512

[42] Irie, H.; Todt, C.; Kumada, N.; Harada, Y.; Sugiyama, H.; Akazaki, T.; Muraki, K. *Phys. Rev. B* **2016**, *94*, 155305

[43] Su, Z.; Zarassi, A.; Nguyen, B.-M.; Yoo, J.; Dayeh, S. A.; Frolov, S. M. **2016**, arXiv:1610.03010

[44] Blonder, G.; Tinkham, M.; Klapwijk, T. *Phys. Rev. B* **1982**, *25*, 4515

[45] Car, D.; Wang, J.; Verheijen, M. A.; Bakkers, E. P. A. M.; Plissard, S. R. *Adv. Mater.* **2014**, *26*, 4875–4879

[46] Suyatin, D.; Thelander, C.; Björk, M.; Maximov, I.; Samuelson, L. *Nanotechnology* **2007**, *18*, 105307

[47] Bouslama, M.; Jardin, C.; Ghamnia, M. *Vacuum* **1995**, *46*, 143–146

[48] King, P.; Veal, T. D.; Lowe, M. J.; McConville, C. F. *J. Appl. Phys.* **2008**, *104*, 083709

[49] Petrovykh, D.; Yang, M.; Whitman, L. *Surf. Sci.* **2003**, *523*, 231–240

[50] Ho, J. C.; Ford, A. C.; Chueh, Y.-L.; Leu, P. W.; Ergen, O.; Takei, K.; Smith, G.; Majhi, P.; Bennett, J.; Javey, A. *Appl. Phys. Lett.* **2009**, *95*, 072108

[51] Gobeli, G.; Allen, F. *Phys. Rev.* **1965**, *137*, A245

[52] Hyart, T.; van Heck, B.; Fulga, I.; Burrello, M.; Akhmerov, A.; Beenakker, C. *Phys. Rev. B* **2013**, *88*, 035121

[53] Plugge, S.; Rasmussen, A.; Egger, R.; Flensberg, K. *New J. Phys.* **2017**, *19*, 012001

[54] Vijay, S.; Fu, L. *Phys. Rev. B* **2016**, *94*, 235446

[55] Karzig, T.; Knapp, C.; Lutchyn, R.; Bonderson, P.; Hastings, M.; Nayak, C.; Alicea, J.; Flensberg, K.; Plugge, S.; Oreg, Y. et al. *Phys. Rev. B* **2017**, *95*, 235305

[56] Zuo, K.; Mourik, V.; Szombati, D. B.; Nijholt, B.; van Woerkom, D. J.; Geresdi, A.; Chen, J.; Ostroukh, V. P.; Akhmerov, A. R.; Plissard, S. R. et al. **2017**, arXiv:1706.03331

[57] Flöhr, K.; Liebmann, M.; Sladek, K.; Günel, H. Y.; Frielinghaus, R.; Haas, F.; Meyer, C.; Hardtdegen, H.; Schäpers, T.; Grützmacher, D. et al. *Rev. Sci. Instrum.* **2011**, *82*, 113705

[58] Haynes, W. M. (ed.) CRC Handbook of Chemistry and Physics, **2017**, 97th Edition (Internet Version), CRC Press/Taylor & Francis

[59] Courtois, H.; Meschke, M.; Peltonen, J. T.; Pekola, J. P. *Phys. Rev. Lett.* **2008**, *101*, 067002

[60] Averin, D.; Bardas, A. *Phys. Rev. Lett.* **1995**, *75*, 1831

[61] Kjaergaard, M.; Suominen, H. J.; Nowak, M. P.; Akhmerov, A. R.; Shabani, J.; Palmstrøm, C. J.; Nichele, F.; Marcus, C. M. *Phys. Rev. Applied* **2017**, *7*, 034029

[62] Li, S.; Kang, N.; Caroff, P.; Xu, H. Q. *Phys. Rev. B* **2017**, *95*, 014515

5

Ballistic superconductivity in semiconductor nanowires

Hao Zhang*, Önder Gül*, Sonia Conesa-Boj, Michał P. Nowak, Michael Wimmer, Kun Zuo, Vincent Mourik, Folkert K. de Vries, Jasper van Veen, Michiel W.A. de Moor, Jouri D.S. Bommer, David J. van Woerkom, Diana Car, Sébastien R. Plissard, Erik P.A.M. Bakkers, Marina Quintero-Pérez, Maja C. Cassidy, Sebastian Koelling, Srijit Goswami, Kenji Watanabe, Takashi Taniguchi, Leo P. Kouwenhoven

Semiconductor nanowires have opened new research avenues in quantum transport owing to their confined geometry and electrostatic tunability. They have offered an exceptional testbed for superconductivity, leading to the realization of hybrid systems combining the macroscopic quantum properties of superconductors with the possibility to control charges down to a single electron. These advances brought semiconductor nanowires to the forefront of efforts to realize topological superconductivity and Majorana modes. A prime challenge to benefit from the topological properties of Majoranas is to reduce the disorder in hybrid nanowire devices. Here, we show ballistic superconductivity in InSb semiconductor nanowires. Our structural and chemical analyses demonstrate a high-quality interface between the nanowire and a NbTiN superconductor which enables ballistic transport. This is manifested by a quantized conductance for normal carriers, a strongly enhanced conductance for Andreev-reflecting carriers, and an induced hard gap with a significantly reduced density of states. These results pave the way for disorder-free Majorana devices.

This chapter has been published in *Nature Communications* **8**, 16025 (2017).
*These authors contributed equally to this study.

5.1. Introduction

Majorana modes are zero-energy quasiparticles emerging at the boundary of a topological superconductor [1–3]. Following proposals for their detection in a semiconductor nanowire coupled to a superconductor [4, 5], several electron transport experiments reported characteristic Majorana signatures [6–14]. The prime challenge to strengthen these signatures and unravel the predicted topological properties of Majoranas is to reduce the remaining disorder in this hybrid system. Disorder can mimic zero-energy signatures of Majoranas [15–19], and results in states within the induced superconducting energy gap [20], the so-called soft gap, which renders the topological properties experimentally inaccessible [21, 22]. The soft gap problem is attributed to the inhomogeneity of the hybrid interface [20, 23–25] and has been overcome by a recent demonstration of epitaxial growth of Al superconductor on InAs nanowires [23], yielding a hard gap – a strongly reduced density of states within the induced superconducting gap. However, the Al–InAs nanowire system still contains residual disorder showing up in transport as unintentional quantum dots [13, 23], a common observation in many previous instances of hybrid nanowire devices [9, 18, 19]. As an alternative material system, we have further developed the combination of InSb nanowires with NbTiN as our preferred choice of superconductor [6]. InSb is in general cleaner (i.e. higher electron mobility [26–29]) than InAs. Moreover, InSb has a ~ 5 times larger g-factor, bringing down the required external magnetic field needed to induce the topological phase transition. Our preference for NbTiN relies on its high critical magnetic field exceeding 10 Tesla.

Here, we show ballistic superconductivity in InSb semiconductor nanowires. Our structural and chemical analyses demonstrate a high-quality interface between the InSb nanowire and a NbTiN superconductor. The high-quality interface enables ballistic transport manifested by a quantized conductance for normal carriers, and a strongly enhanced conductance for Andreev-reflecting carriers at energies below the superconducting gap. Our numerical analysis indicates a mean free path of several μm, implying ballistic transport of Andreev pairs in the proximitized nanowire. Finally, tunneling conductance reveals an induced hard gap with a significantly reduced density of states. These results constitute a substantial improvement in induced superconductivity in semiconductor nanowires, and pave the way for disorder-free Majorana devices.

5.2. Results

5.2.1. Hybrid nanowire devices and their structural analysis

We report on five devices with different geometries all showing consistent results. An overview of all the devices is given in Supplementary Figure 5.S1. Figure 5.1a and b show a nanowire device consisting of a normal contact (Au), a nanowire (InSb) and a superconducting contact (NbTiN). This device was first measured at low temperature showing high-quality electron transport (data discussed below). After, the device was sliced open (using focused ion beam) and inspected sideways in a transmission electron microscope (TEM). The hexagonal facet structure of the nanowire is clearly visible (Figure 5.1c and Supplementary Figure 5.S2). Except for the bottom facet that rests on the substrate, the polycrystalline superconductor covers the nanowire all around without any visible voids.

The precise procedure for contact realization is extremely important (see Ref. [25]).

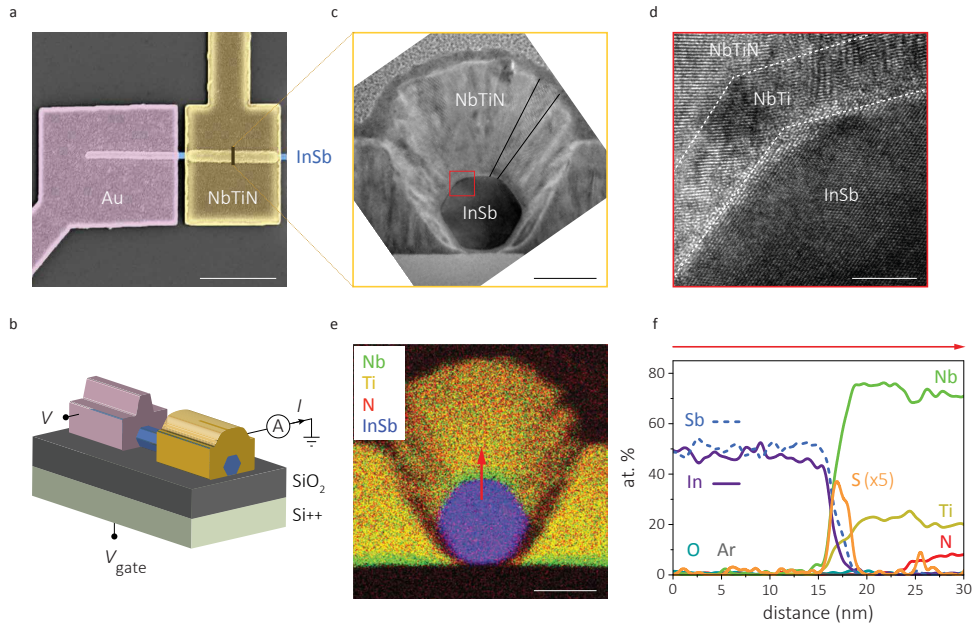

Figure 5.1 | TEM analysis of a typical device. **a,** Top-view, false-colour electron micrograph of device A. Scale bar: 1 μm. Normal metal contact is Cr/Au (10 nm/125 nm) and superconducting contact is NbTi/NbTiN (5 nm/85 nm). Contact spacing is ~ 100 nm. **b,** Device schematic and measurement setup. **c,** Low-magnification high-resolution TEM (HRTEM) cross-sectional image from the device (see Methods Section 5.3). Scale bar: 50 nm. The cut was performed perpendicular to the nanowire axis, indicated by the dark bar in **a**. InSb nanowire exhibits a hexagonal cross-section surrounded by {220} planes. The NbTiN on the pre-layer NbTi crystallizes as cone-like elongated grains, indicated by the thin black lines. Corresponding fast Fourier transform confirms the polycrystalline character of the NbTiN region (Supplementary Figure 5.S2b). **d,** HRTEM image near the interface (red square in **c**) shows that our cleaning procedure only minimally etches the wire and the InSb crystalline properties are preserved after the deposition. Scale bar: 5 nm. **e,** Energy-dispersive X-ray (EDX) compositional map of the device cross-section. Scale bar: 50 nm. **f,** EDX line scan taken across the interface as indicated by the red arrow in **e**. The Sulfur content is multiplied by 5 for clarity. The system is oxygen and argon free (contact deposition is performed in an Ar plasma environment).

First, the native oxide at the InSb surface is wet-etched using a sulfur-based solution followed by an argon etch of sufficiently low-power to avoid damaging the InSb surface (see Methods Section 5.3). The inclusion of sulfur at the interface results in band bending with electron accumulation near the surface of InSb [30] (see Supplementary Figure 5.S3). Superconducting film deposition starts with NbTi, a reactive metal whose inclusion as a wetting layer is crucial to create a good electrical contact. Figure 5.1d shows that our cleaning procedure only minimally etches the wire and the InSb crystalline properties are preserved after the deposition (details in Supplementary Figure 5.S2). We detect a thin segregation layer (~ 2 nm) between the polycrystalline NbTi and single crystalline InSb. The chemical analysis (Figure 5.1e and f) shows a material composition in agreement with our deposition procedure. More importantly, the inclusion of sulfur is clearly visible at the interface whereas the original native oxide is completely absent.

5.2.2. Ballistic Transport

The high-quality structural properties in Figure 5.1 result in largely improved electronic properties over the previous instances of hybrid nanowire devices. Figure 5.2a shows the differential conductance $\mathrm{d}I/\mathrm{d}V$ while varying the bias voltage V between the normal and superconducting contacts, and stepping the gate voltage V_{gate} applied to the global back gate (Figure 5.1b). We first of all note that throughout the entire gate voltage range in Figure 5.2 we do not observe signs of the formation of unintentional quantum dots or any other localization effects resulting from potential fluctuations. Instead, we observe conductance plateaus at $2e^2/h$ for all devices, typical for ballistic transport

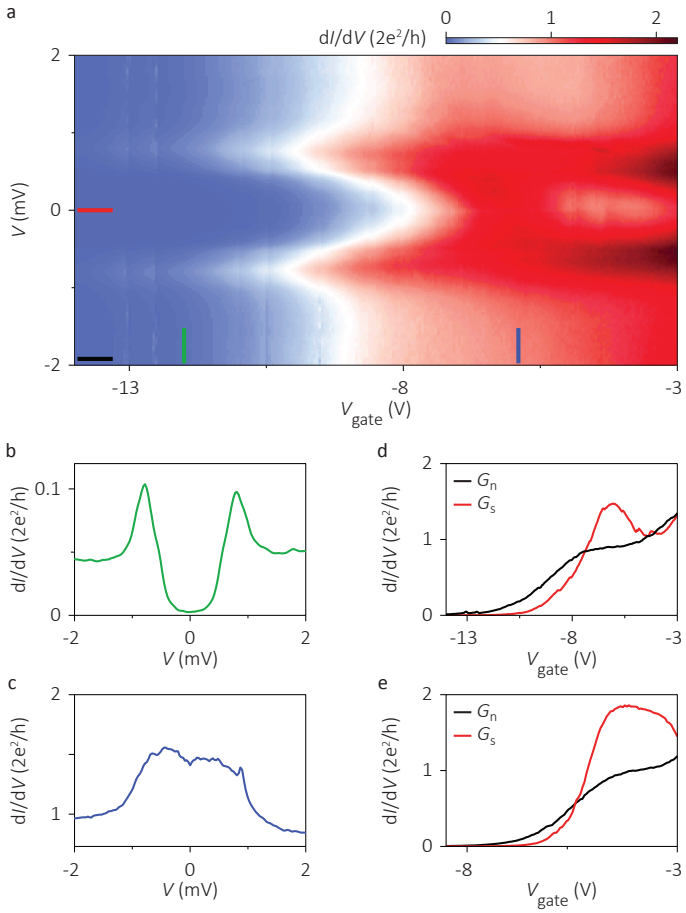

Figure 5.2 | Ballistic transport at zero magnetic field. a, Differential conductance, $\mathrm{d}I/\mathrm{d}V$, as a function of bias voltage, V, and gate voltage, V_{gate} for device B. **b,** Vertical line cut from **a** in tunnelling regime (green trace, gate voltage = −12 V). **c,** Vertical line cut from **a** on the conductance plateau (blue trace, gate voltage = −5.9 V). **d,** Horizontal line cuts from **a** showing above-gap (G_{n}, black, $|V| = 2$ mV) and subgap (G_{s}, red, $V = 0$ mV) conductance. **e,** Above-gap (black) and subgap (red) conductance for device C, where G_{s} enhancement reaches $1.9 \times 2e^2/h$.

and a clear signature of disorder-free devices. For a sufficiently negative gate voltage the non-covered nanowire section between normal and superconducting contacts is depleted and serves as a tunnel barrier. A vertical line cut from this regime is plotted in Figure 5.2b, showing a trace typical for an induced superconducting gap with a strong conductance suppression for small V. The extracted gap value is $\Delta^* = 0.8$ meV. Increasing V_{gate} first lowers and then removes the tunnel barrier completely. A vertical line cut from this open regime is plotted in Figure 5.2c. In this case, the conductance for small V is enhanced compared to the value above ~ 1 mV. Note that the range in V showing an enhanced conductance in Figure 5.2c corresponds to the same range showing the induced gap in Figure 5.2b. The enhancement results from Andreev processes where an incoming electron reflects as a hole at the normal conductor–superconductor interface generating a Cooper pair [23, 24, 31, 32]. This Andreev process effectively doubles the charge being transported from e to $2e$ enhancing the subgap conductance. In Figure 5.2c the observed enhancement is by a factor ~ 1.5.

The Andreev enhancement is also visible in horizontal line cuts as shown in Figure 5.2d. The above-gap conductance (black trace) taken for $|V| = 2$ mV represents the conductance for normal carriers, G_{n}. The subgap conductance, G_{s}, near $V = 0$ (Figure 5.2d, red trace) shows an Andreev enhancement in the plateau region. Figure 5.2e shows a similar trace from another device where the enhancement in G_{s} reaches $1.9 \times 2e^2/h$, very close to the theoretical limit: an enhancement factor of 2 in the case of a perfect interface. Finally, we note the dip in subgap conductance G_{s} following the Andreev enhancement, observed both in Figure 5.2d and e. The combined enhancement and dip structure provides a handle for estimating the remaining disorder by a comparison to theory, as discussed below.

5.2.3. Theoretical simulation

We construct a tight binding model of our devices (Figure 5.3a) and numerically calculate the conductance using the Kwant package [33] (see Methods Section 5.3 for details). In Figure 5.3b we plot the conductance traces obtained from the simulation for different disorder strength corresponding to varying mean free paths l_{e}. The calculated subgap conductance reproduces the dip structure observed in the experiment. We find that the dip is caused by mixing between the first and the second subband due to residual disorder (see Supplementary Figure 5.S4). Even for weak disorder, subband mixing is strongly enhanced near the opening of the next channel, due to the van Hove singularity at the subband bottom. Hence, the Andreev conductance will generically exhibit a dip close to the next conductance step, instead of a perfect doubling. Figure 5.3c shows the measured subgap conductance G_{s} and above-gap conductance G_{n} for a device with a particularly flat plateau. Comparing Figure 5.3b and c, we find good agreement for a mean free path of several μm. This implies ballistic transport of Andreev pairs in the proximitized wire section underneath the superconductor, whose length far exceeds the length of the non-covered wire between the contacts (see also Supplementary Figure 5.S5). Andreev enhancement allows for extracting mean free paths greatly exceeding the non-covered wire section since the subgap conductance is sensitive to even minute disorder in the proximitized wire section—a new finding of our study. This sensitivity is due to the quadratic dependence of the subgap conductance on the transmission probability (in-

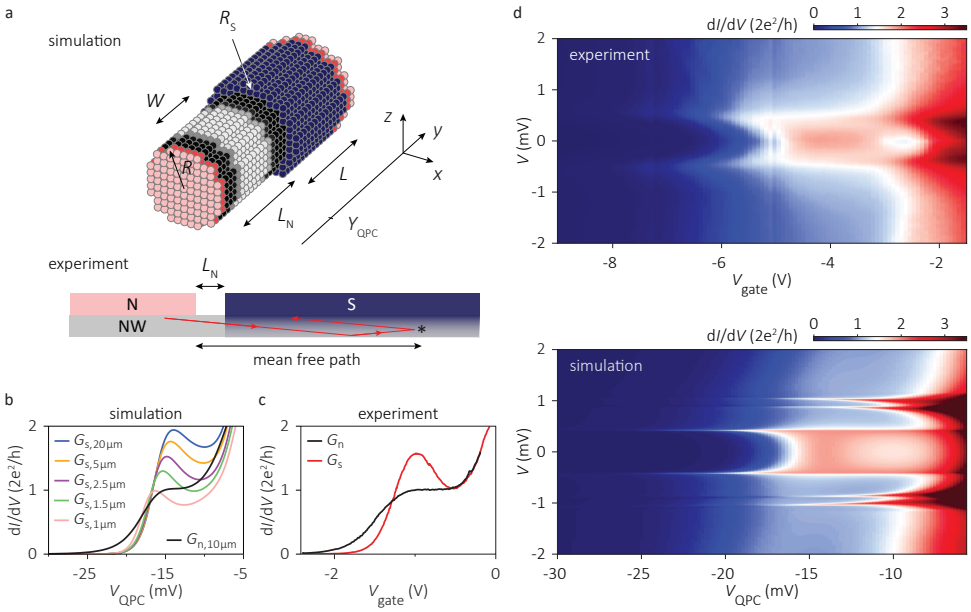

Figure 5.3 | Theoretical simulation. a, Theoretical model (top): A cylindrical nanowire (black, gray, white) with length $L_N + L$ (100 nm + 800 nm), where the latter part is partially coated by a superconductor leaving the bottom surface uncovered. (Scheme shows $L = 100$ nm for clarity.) The wire radius R is 40 nm and the superconducting film has a thickness $R_s = 10$ nm. (Our wire radius varies from device to device between 30 and 50 nm, and we have confirmed that our simulations give similar results within this range.) The wire is terminated from both sides with infinite leads (pink). Front lead is normal, back lead is normal/superconductor. Each little circle represents a three dimensional mesh site with a size of 7 nm. White circles depict a potential barrier with a width $W = 60$ nm in the uncovered wire section forming a quantum point contact (QPC). Gray circles represent the smoothness of the barrier which is set to 5 nm. Experimental geometry (bottom): Cross-sectional schematic shows the nanowire (NW), the normal contact (N), and the superconducting contact (S). Superconductivity is induced in the nanowire section underneath the superconducting contact. Transport is ballistic through a proximitized wire section, whose length far exceeds L_N, the length of the non-covered wire between the contacts. **b,** Numerical simulation for devices with different mean free paths (see Supplementary Figure 5.S5). Black trace is for G_n corresponding to a mean free path 10 μm, the rest are for G_s corresponding to a mean free path ranging from 1 μm (pink) to 20 μm (blue). **c,** Above-gap (black) and subgap (red) conductance for device D. **d, e,** Comparison between the measurement (device C) and the simulation of a ballistic device with $l_e = 10$ μm. The induced superconducting gap edges for higher subbands, visible in the simulation as four symmetric peaks outside the gap around $V \sim \pm 1$ mV, are not observed in the experiment (see Methods Section 5.3 for details).

troduced below). In Figure 5.3d and e we compare a conductance measurement similar to the one in Figure 5.2a with the simulation of a ballistic device. The overall agreement indicates a very low disorder strength for our devices.

5.2.4. Hard superconducting gap

The theory for electronic transport from a normal conductor via a quantum point contact to a superconductor was developed by Beenakker [31]. The subgap conductance is described by Andreev reflections [32], and for a single subband given by $G_s = 4e^2/h \times$

$T^2/(2-T)^2$. The gate voltage dependent transmission probability T can be extracted from the measured above-gap conductance, given by $G_n = 2e^2/h \times T$. Figure 5.4a shows excellent agreement between the calculated and measured subgap conductance up to the point where the measured Andreev enhancement is reduced due to subband mixing. The highest transmission probability obtained from Andreev enhancement sets a lower bound on the interface transparency. Our typical enhancement factor of 1.5 (Figure 5.2d and 5.3c) implies an interface transparency ~ 0.93 and our record value of 1.9 (Figure 5.2e) gives a transparency larger than 0.98 (see Measurement setup and data analysis in Methods Section 5.3).

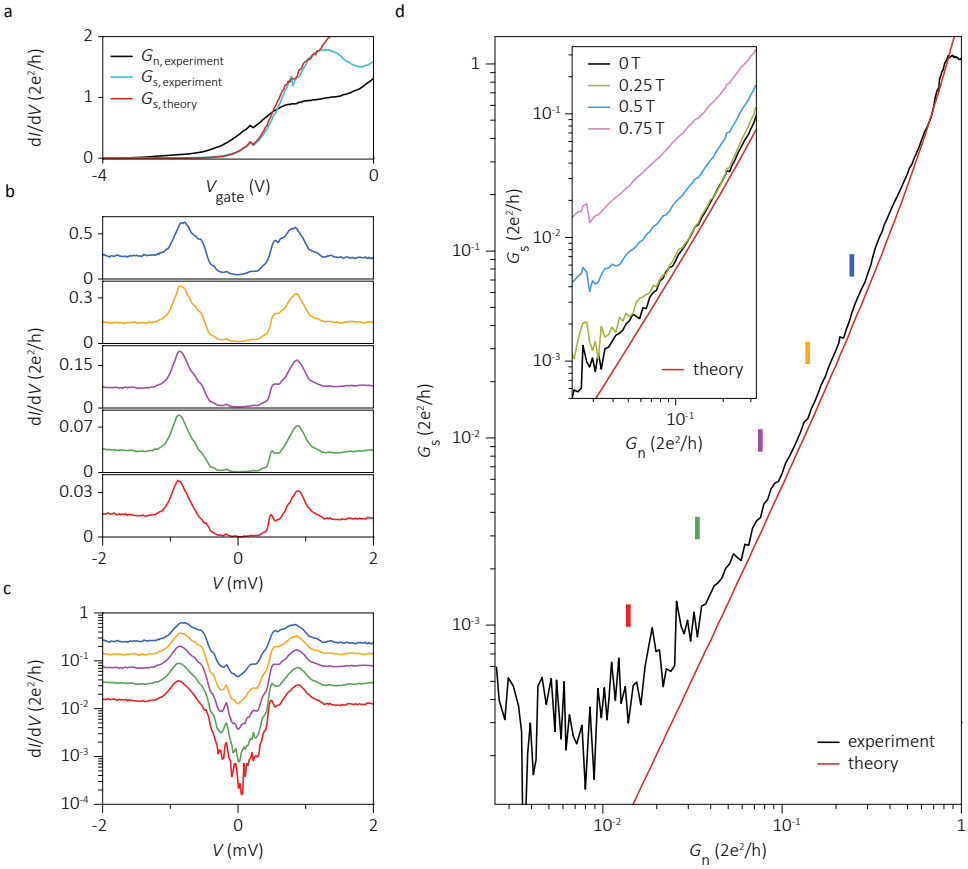

Figure 5.4 | Hard gap and Andreev transport. a, Above-gap (black) and subgap (blue) conductance for device E. Red curve is a theory prediction based on single channel Andreev reflection, agreeing perfectly with experimental data without any fitting parameter up to the dip on the right side of the plateau where the second channel starts conducting. **b, c,** Five typical gap traces corresponding to the five colour bars indicated in **d** plotted on a linear and logarithmic scale. The subgap conductance is suppressed by a factor up to 50 for the lowest conductance (red trace). **d,** Subgap conductance G_s as a function of above-gap conductance G_n for device A. Red curve is the theory prediction assuming only Andreev processes. Inset shows G_s versus G_n taken at different magnetic fields.

The comparison between G_s versus G_n can be continued into the regime of an increasing tunnel barrier. Figure 5.4b and c show traces of dI/dV for successively lower conductances. The subgap conductance suppression reaches $G_s/G_n \sim 1/50$, a value comparable to the results obtained with epitaxial Al [23]. A comparison between the measured subgap conductance and Beenakker's theory (without any fit parameters) is shown in Figure 5.4d. The excellent agreement over three orders of magnitude in conductance implies that the subgap conductance is very well described by Andreev processes and no other transport mechanisms are involved [23, 24]. The lowest conductance ($\sim 5 \cdot 10^{-4} \times 2e^2/h$) reaches our measurement limit, causing the deviation from theory. The inset to Figure 5.4b shows how the subgap conductance increases when applying a magnetic field. Finally, in Supplementary Figure 5.S6 we show the magnetic field dependence of the induced gap and Andreev enhancement for a magnetic field along the nanowire axis. We again find a subgap conductance increasing with magnetic field, and an Andreev enhancement vanishing at a magnetic field (< 1 Tesla) smaller than the critical field of our NbTiN film. We speculate that the increasing subgap conductance and the decreasing Andreev enhancement are due to vortex formation in our NbTiN film, a type-II superconductor. Future studies should be directed towards developing a quantitative description of such magnetic field-induced deviation from Andreev transport, whose understanding plays a crucial role in realizing a topological quantum bit based on semiconductor nanowires.

5.3. Methods

5.3.1. Nanowire growth and device fabrication

InSb nanowires have been grown by Au-catalyzed Vapor-Liquid-Solid mechanism in a Metal Organic Vapor Phase Epitaxy reactor. The InSb nanowire crystal direction is [111] zinc blende, free of stacking faults and dislocations [34]. Nanowires are deposited one-by-one using a micro-manipulator [35] on a substrate covered with 285 nm thick SiO_2 serving as a gate dielectric for back gated devices. For local gated device D, extra set of bottom gates are patterned on the substrate followed by transfer of h-BN (~ 30 nm thick) onto which nanowires are deposited. The contact deposition process starts with resist development followed by oxygen plasma cleaning. Then, the chip is immersed in a sulfur-rich ammonium sulfide solution diluted by water (with a ratio of 1:200) at 60 °C for half an hour [36]. At all stages care is taken to expose the solution to air as little as possible. For normal metal contacts [27], the chip is placed into an evaporator. A 30 second Helium ion milling is performed in-situ before evaporation of Cr/Au (10 nm/125 nm) at a base pressure < 10^{-7} mbar. For superconducting contacts [25], the chip is mounted in a sputtering system. After 5 seconds of in-situ Ar plasma etching at a power of 25 Watts and an Ar pressure of 10 mTorr, 5 nm NbTi is sputtered followed by 85 nm NbTiN.

5.3.2. Measurement setup and data analysis

All the data in this article is measured in a dilution refrigerator with a base temperature around 50 mK using several stages of filtering. The determination of the Andreev enhancement factor depends sensitively on the contact resistance subtracted from the measured data. In all our analysis we only subtract a fixed-value series resistance of

0.5 kΩ solely to account for the contact resistance of the normal metal lead. This value is smaller than the lowest contact resistance we have ever obtained for InSb nanowire devices [27], which makes the values for the interface transparency a lower bound.

5.3.3. Structure characterization

The cross-section and lamella for TEM investigations were prepared by focused ion beam (FIB). FIB milling was carried out with a FEI Nova Nanolab 600i Dualbeam with a Ga ion beam following the standard procedure [37]. We used electron induced Co and Pt deposition for protecting the region of interest and a final milling step at 5 kV to limit damage to the lamella. High-resolution TEM (HRTEM) and scanning TEM analyses were conducted using a JEM ARM200F aberration-corrected TEM operated at 200 kV. For the chemical analysis, energy-dispersive X-ray (EDX) measurements were carried out using the same microscope equipped with a 100 mm^2 EDX silicon drift detector (SSD).

5.3.4. Characterization of NbTiN

Our NbTiN films are deposited using an ultrahigh vacuum AJA International ATC 1800 sputtering system (base pressure ~ 10^{-9} Torr). We used a $Nb_{0.7}Ti_{0.3}$ wt. % target with a diameter of 3 inches. Reactive sputtering resulting in nitridized NbTiN films was performed in an Ar/N_2 process gas with 8.3 at. % N_2 content at a pressure of 2.5 mTorr using a DC magnetron sputter source at a power of 250 Watts. An independent characterization of the NbTiN films gave a critical temperature of 13.3 K for 90 nm thick films with a resistivity of 126 $\mu\Omega$·cm and a compressive stress on Si substrate.

5.3.5. Details of the theoretical simulation

The system is described by the spin-diagonal Bogoliubov-de Gennes Hamiltonian

$$H = \left(\frac{\hbar^2\mathbf{k}^2}{2m^*} - \mu + V(x,y,z)\right)\tau_z + \Delta(x,y,z)\tau_x \tag{5.1}$$

acting on the spinor $\Psi = (\psi_{e+}, \psi_{e-}, \psi_{h-}, -\psi_{h+})^T$. The Pauli matrices act on the electron-hole degree of freedom. Potential in the nanowire is described by $V(x,y,z) = \tilde{V}_{\mathrm{qpc}}(y) + V_D(x,y,z)$, where $\tilde{V}_{\mathrm{qpc}}(y)$ describes a quantum point contact given by

$$\tilde{V}_{\mathrm{qpc}}(y) = -\frac{eV_{\mathrm{QPC}}}{2}\left[\tanh\frac{y - Y_{\mathrm{QPC}} + W/2}{\lambda} - \tanh\frac{y - Y_{\mathrm{QPC}} - W/2}{\lambda}\right].$$

Here Y_{QPC} is the centre position of the barrier (Figure 5.3a). Barrier width is $W = 60$ nm, and the barrier height is controlled by V_{QPC}. The softness of the barrier is given by λ which we take 5 nm. $V_D(x,y,z)$ accounts for disorder, which is modelled as a spatially varying potential with random values from a uniform distribution within a range $[-U_0, U_0]$ where amplitude $U_0 = \sqrt{3\pi/l_e m^{*2} a^3}$ is set by mean free path l_e.

We approximate the superconductor covering the wire by a layer of non-zero Δ for $(x^2 + z^2) > R$ and $y > L_N$ and $z > -R$. The huge wave vector difference in the superconductor and semiconductor cannot be captured in a numerical simulation of a three-dimensional device. Hence, to capture the short coherence length in the superconductor, we take a superconducting shell of thickness $R_S = 10$ nm and $\Delta = 200$ meV. We then

tune the induced gap to be close to the experimental value (~ 0.5 meV) by reducing the hopping between the semiconductor and the superconductor by a factor of 0.8.

The transport properties of the system are calculated using Kwant package [33] with the Hamiltonian in eq. (5.1) discretized on a 3D mesh with spacing $a = 7$ nm and infinite input (normal) and output (normal/superconducting) leads. For a given V_{QPC} and excitation energy ε we obtain the scattering matrix of the system from which we subsequently extract electron $r_e(\varepsilon)$ and hole $r_h(\varepsilon)$ reflection submatrices. Finally, we calculate thermally averaged conductance for injection energy $E = -eV$ according to

$$G(E) = \int d\varepsilon \mathscr{G}(\varepsilon) \left(-\frac{\partial f(E,\varepsilon)}{\partial \varepsilon} \right),$$

where the Fermi function

$$f(E,\varepsilon) = \frac{1}{e^{(\varepsilon - E)/k_b T} + 1}$$

and $\mathscr{G}(\varepsilon) = N - \|r_e(\varepsilon)\|^2 + \|r_h(\varepsilon)\|^2$. We assume chemical potential to be $\mu = 30$ meV, which gives $N = 3$ spin-degenerate modes in the leads. The presented results are obtained for $T = 70$ mK and InSb effective mass $m^* = 0.014 m_e$.

5

Data availability

All data is available at doi.org/10.4121/uuid:fdeb81ab-1478-4682-9f48-dec1c83242bd [38]. The code used for the simulations is available upon request.

Acknowledgments

We thank A.R. Akhmerov, O.W.B. Benningshof, A. Geresdi, J. Kammhuber and A.J. Storm for discussions and assistance. This work has been supported by the Netherlands Organisation for Scientific Research (NWO), Foundation for Fundamental Research on Matter (FOM), European Research Council (ERC), and Microsoft Corporation Station Q.

Author contributions

H.Z. and Ö.G. fabricated the devices, performed the measurements, and analyzed the data. S.C.-B. performed the TEM analysis. M.P.N. and M.W. performed the numerical simulations. K.Z., V.M., F.K.d.V., J.v.V., M.W.A.d.M., J.D.S.B., D.J.v.W., M.Q.-P., M.C.C. and S.G. contributed to the experiments. D.C., S.P. and E.P.A.M.B. grew the InSb nanowires. S.K. prepared the lamellae for the TEM analysis. K.W. and T.T. synthesized the h-BN crystals. L.P.K. supervised the project. All authors contributed to the writing of the manuscript.

5.S. Supplementary Information

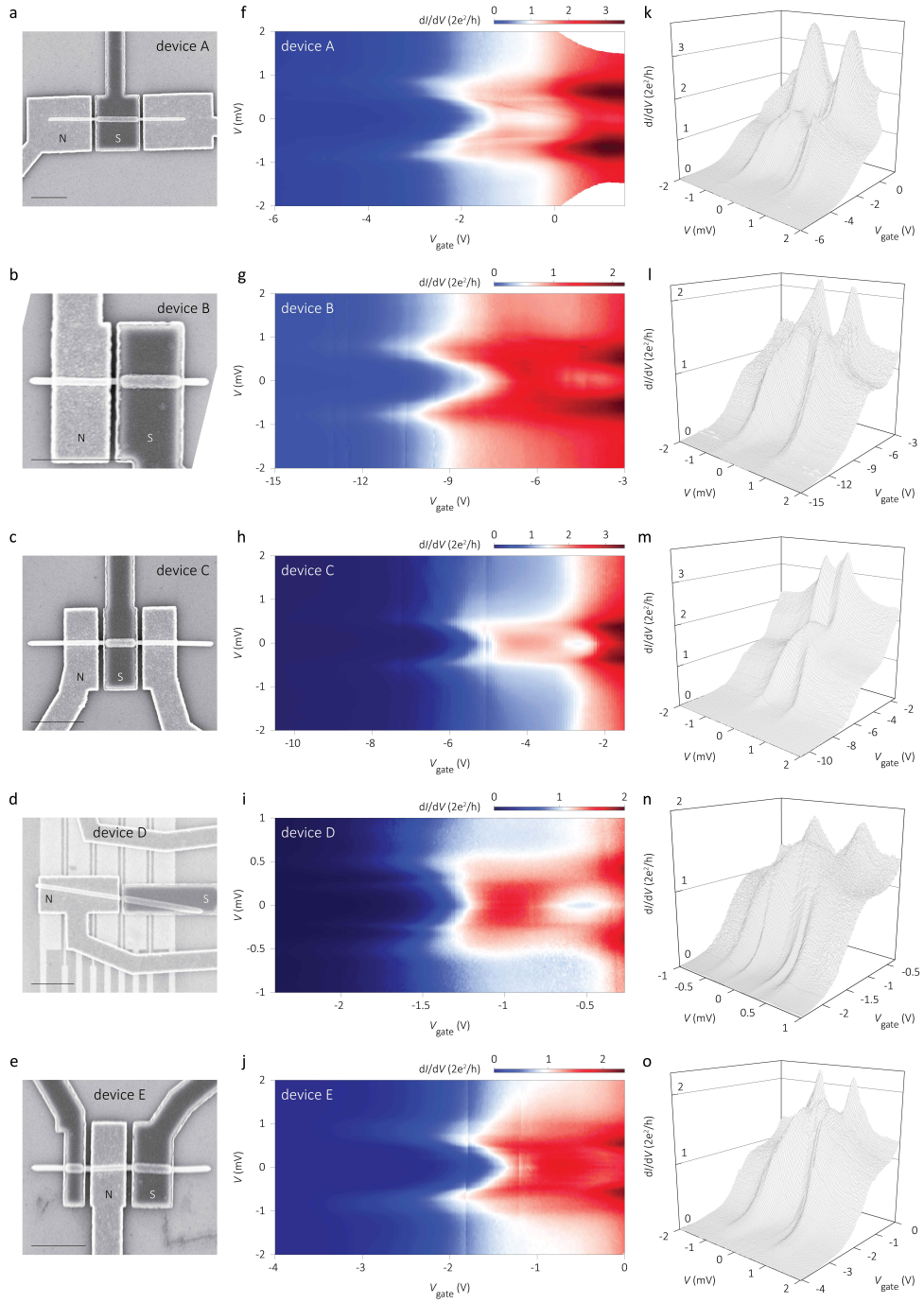

Figure 5.S1 | Electron micrographs and ballistic transport for all devices. a-e, Electron micrographs of all presented devices. N indicates the normal metal lead, S the superconducting lead. For three terminal devices, unlabelled leads are kept floated throughout the measurements. Scale bars for all images indicate 1 μm. Data in Figure 3c (main text) is taken by sweeping the local gate underneath the uncovered wire section (see device D in panel d). **f-j,** Differential conductance of all devices in colour scale as a function of bias and gate voltage at zero magnetic field. **k-o,** Same as **f-j** but the differential conductance is on the vertical axis. All devices show quantized conductance, Andreev enhancement and an induced superconducting gap of 0.9 mV (A), 0.8 mV (B), 0.6 mV (C), and 0.52mV (D), 0.85 mV (E). Unintentional quantum dots are absent in all devices. Correspondence with the figures in main text: data in Figures 5.1 and 5.4b-d taken on device A, Figures 5.2a-d on device B, Figures 5.2e and 5.3d on device C, Figure 5.3c on Device D, Figure 5.4a on device E.

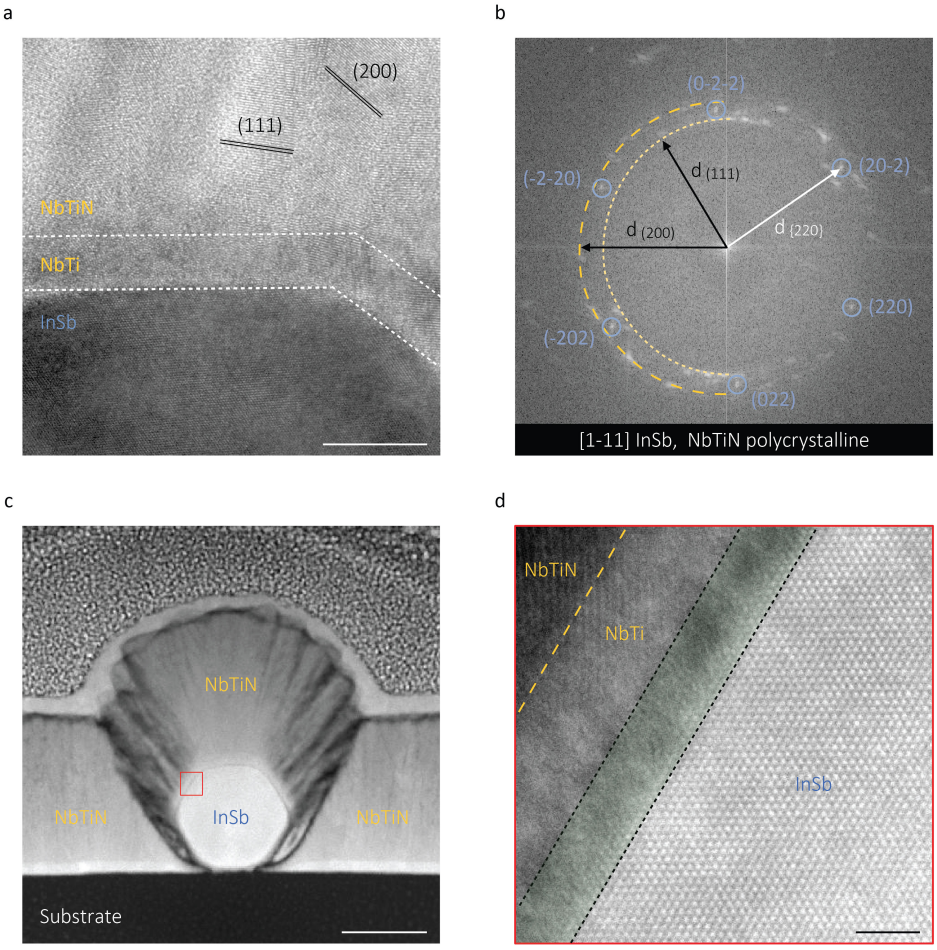

Figure 5.S2 | Structure characterization and high-angle annular dark field analysis of the InSb-NbTi-NbTiN interface. **a,** High-resolution TEM cross-sectional image obtained by aligning the InSb nanowire along the zone axis in the [111] orientation. Scale bar: 10 nm. **b,** Fast Fourier transform (FFT) corresponding to **a** revealing the presence of both InSb and NbTiN. The NbTiN contribution leads to the formation of several Bragg spots on concentric rings, which provides evidence of the existence of several grains with different orientations in the original image. Each ring with different radius corresponds to a particular value of the interplanar spacing, i.e., it is the result of the reflections associated to a specific family of planes. Two different d-spacings have been identified and measured: $d_{(111)} = 0.249$ nm and $d_{(200)} = 0.213$ nm. They are indicated with yellow dashed lines in **b**. From these values, it is possible to determine the NbTiN lattice parameter which we obtain to be 0.430 nm. On the other hand, the six {220} reflections, indicated by a blue circle in the FFT, arise from the InSb region. From the calculated interplanar value of $d_{\{220\}} = 0.230$ nm we can estimate the InSb lattice parameter to be around 0.649 nm. The obtained lattice parameters for both NbTiN and InSb are in good agreement with the respective values reported in the literature. **c,** High-angle annular dark field (HAADF) scanning transmission electron microscopy (STEM) image of the device cross-section. Scale bar: 50 nm. **d,** Atomic resolution HAADF-STEM image of the interface for the region marked by the red square in **c**. Scale bar: 2 nm. The highlighted area in green indicates the 2 nm deep NbTi segregation into the InSb core. This effect is in good agreement with the EDX line scan, see Figure 5.1f, which shows the NbTi region to be segregated 2 nm deep into the InSb core on the {220} facets.

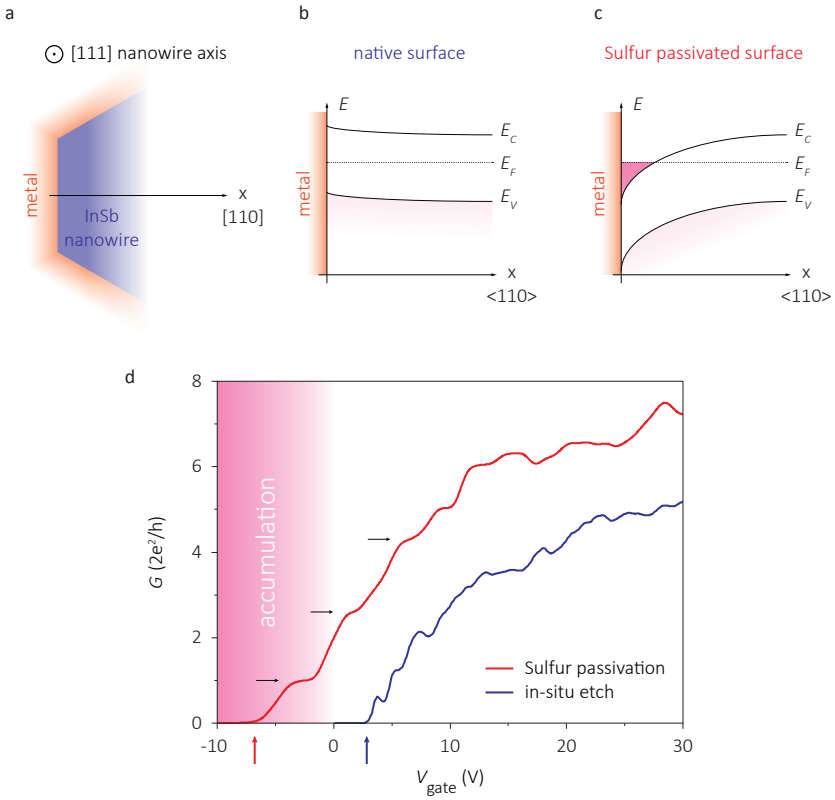

Figure 5.S3 | Inclusion of Sulfur creates surface accumulation by band bending. a, A schematic of the device cross-section showing both the nanowire and the contact metal. Nanowire axis is along [111] and the hexagonal facets have <110> orientation. **b,** Band diagram for an InSb surface with <110> orientation. Fermi level at the surface lies closer to the valence band [30]. **c,** Band diagram for an InSb surface with <110> orientation passivated with Sulfur-based solution. Inclusion of Sulfur at the surface counteracts the depletion and pins the Fermi level in the conduction band. This creates an electron-rich nanowire surface. **d,** Gate voltage response of nanowire devices with different contact preparation. A finite conductance for negative gate voltages indicates electron accumulation, highlighted in pink. Blue curve is taken from a device with contacts prepared using in-situ Ar plasma etch, red curve from a device with contacts prepared using Sulfur passivation. Both devices have identical geometries with a channel length of 150 nm. Devices with Sulfur passivated contact areas exhibit a negative threshold voltage (red arrow), in contrast to the devices with in-situ plasma etched contact areas (blue arrow). This typical characteristic measured on hundreds of nanowire devices indicates the doping effect of Sulfur inclusion at the InSb nanowire surface. Black arrows indicate the 1st, the 3rd, and the 5th quantized conductance plateau [27]. Upper plateaus appear at lower conductance values due to a finite contact resistance which is not subtracted from the conductance traces shown here. We also find that Sulfur passivated contacts show lower contact resistances than in-situ etched contacts, which can be seen from the difference in saturation conductance of both traces at high gate voltages.

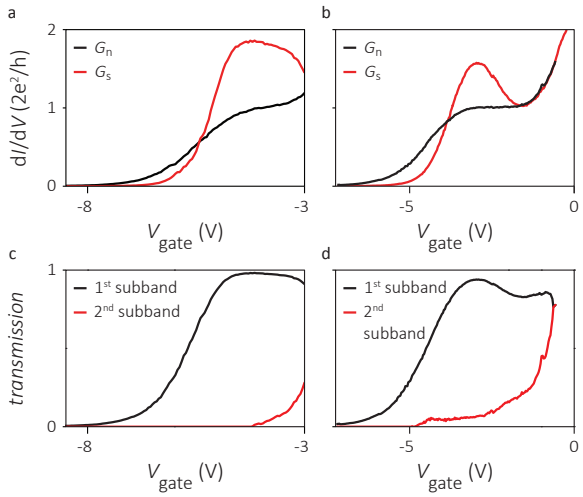

Figure 5.S4 | Subband mixing. **a, b,** The panels show the measured data, **a** from Figure 5.2e and **b** from Figure 5.3c. **c, d,** The panels show the transmission T of the first two subbands extracted from **a** and **b**, respectively, using $G_n = 2e^2/h\sum T_i$ and $G_s = 4e^2/h\sum T_i^2/(2-T_i)^2$. When the transmission of the second subband becomes finite, the conductance modes mix, decreasing the Andreev enhancement. This effect shows up as a dip in G_s when plotted as a function of gate voltage V_{gate}.

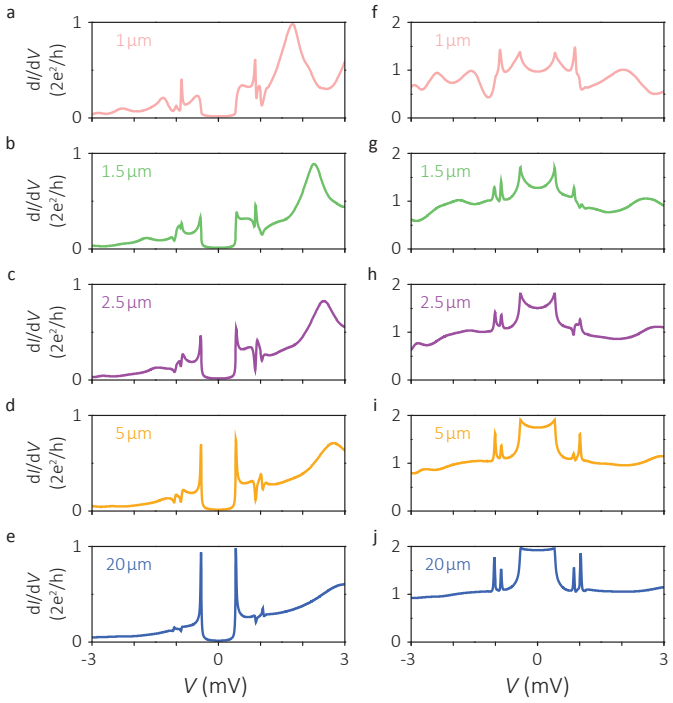

Figure 5.S5 | Simulated conductance for varying mean free paths. a-e, The tunnelling conductance for different disorder strengths with mean free path l_e ranging from 1 μm to 20 μm. **f-j,** The conductance in the plateau regime for different disorder strengths with mean free path l_e ranging from 1 μm to 20 μm. For short l_e, the Andreev enhancement is lower than that observed in our measurements and disorder-induced conductance fluctuations dominate the conductance for above-gap bias which we do not observe in our measurements. A good correspondence with the measurements is found for $l_e > 2.5\,\mu$m. We note that the details of the peak-dip structure in the Andreev conductance depend on several additional parameters of the system (e.g. barrier smoothness or disorder realization). In contrast, we find the conductance fluctuations above the gap to depend mainly on disorder strength, so that the combined analysis can be used as an estimate for the mean free path. The four symmetric peaks outside the gap around $V \sim \pm 1$ mV indicate the induced superconducting gap for the higher two subbands (three subbands are occupied in total). Asymmetric conductance for different bias polarity is due to energy dependent transmission through the tunnel barrier, i.e., for positive bias V, effective QPC potential is lower.

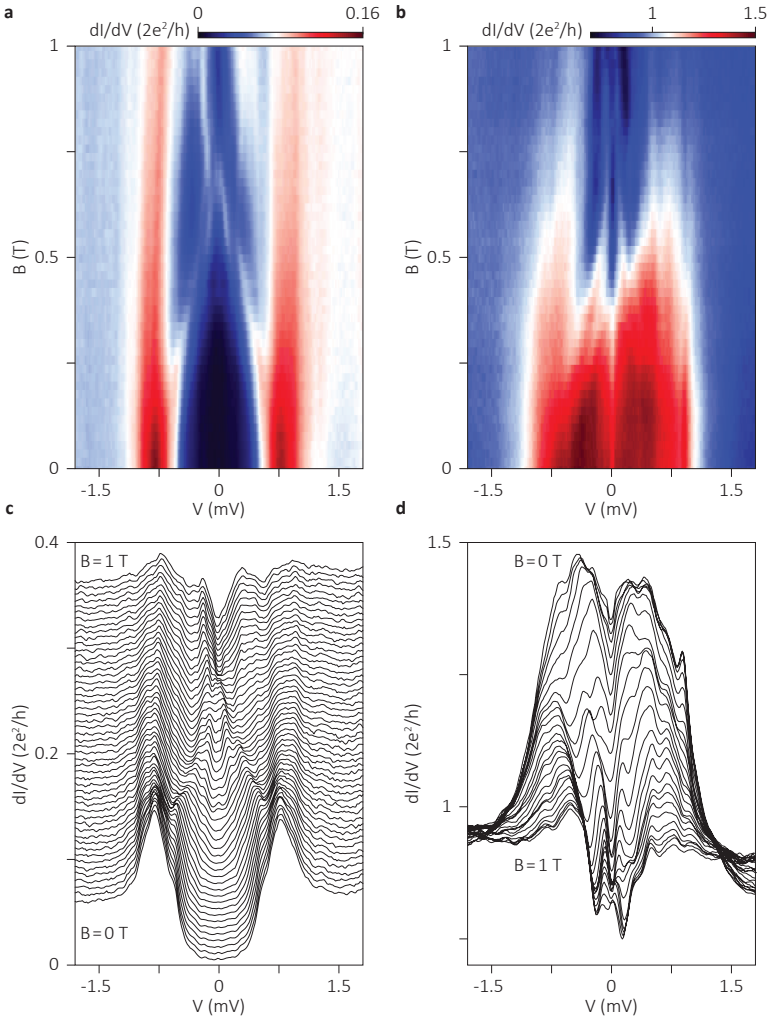

Figure 5.S6 | Magnetic field dependence of the induced gap and Andreev enhancement. a, Differential conductance $\mathrm{d}I/\mathrm{d}V$ of device B as a function of magnetic field B along the nanowire when the device is in the tunneling regime (gate voltage = −12 V). We find an induced superconducting gap of 0.8 mV at zero magnetic field. Increasing magnetic fields increase the subgap conductance but a gap feature can be identified at least up to 1 Tesla, indicating that the NbTiN leads are still superconducting. **b,** Differential conductance $\mathrm{d}I/\mathrm{d}V$ of the same device as a function of magnetic field B (along the wire axis) when the device is in the plateau regime (gate voltage = −6 V). At zero magnetic field, we find an enhancement of conductance up to a factor of ∼ 1.5 for subgap energies due to Andreev reflection. Increasing magnetic fields have a negligible effect on the above-gap conductance. In contrast, the Andreev enhancement is suppressed at 1 Tesla, a magnetic field at which the NbTiN leads are still superconducting. **c,** Line cuts from the data in **a** with vertical offsets $0.006 \times 2e^2/h$. **d,** Line cuts from the data in **b** without offset.

References

[1] Read, N. & Green, D. Paired states of fermions in two dimensions with breaking of parity and time-reversal symmetries and the fractional quantum Hall effect. *Phys. Rev. B* **61**, 10267 (2000)

[2] Kitaev, A. Y. Unpaired Majorana fermions in quantum wires. *Phys. Usp.* **44**, 131–136 (2001)

[3] Fu, L. & Kane, C. L. Superconducting proximity effect and Majorana fermions at the surface of a topological insulator. *Phys. Rev. Lett.* **100**, 096407 (2008)

[4] Lutchyn, R. M., Sau, J. D. & Das Sarma, S. Majorana fermions and a topological phase transition in semiconductor-superconductor heterostructures. *Phys. Rev. Lett.* **105**, 077001 (2010)

[5] Oreg, Y., Refael, G. & von Oppen, F. Helical liquids and Majorana bound states in quantum wires. *Phys. Rev. Lett.* **105**, 177002 (2010)

[6] Mourik, V., Zuo, K., Frolov, S. M., Plissard, S. R., Bakkers, E. P. A. M. & Kouwenhoven, L. P. Signatures of Majorana fermions in hybrid superconductor-semiconductor nanowire devices. *Science* **336**, 1003–1007 (2012)

[7] Das, A., Ronen, Y., Most, Y., Oreg, Y., Heiblum, M. & Shtrikman, H. Zero-bias peaks and splitting in an Al-InAs nanowire topological superconductor as a signature of Majorana fermions. *Nature Phys.* **8**, 887–895 (2012)

[8] Rokhinson, L. P., Liu, X. & Furdyna, J. K. The fractional a.c. Josephson effect in a semiconductor–superconductor nanowire as a signature of Majorana particles. *Nat. Phys.* **8**, 795–799 (2012)

[9] Deng, M. T., Yu, C. L., Huang, G. Y., Larsson, M., Caroff, P. & Xu, H. Q. Anomalous zero-bias conductance peak in a Nb–InSb nanowire–Nb hybrid device. *Nano Lett.* **12**, 6414–6419 (2012)

[10] Churchill, H. O. H. *et al.* Superconductor-nanowire devices from tunneling to the multichannel regime: Zero-bias oscillations and magnetoconductance crossover. *Phys. Rev. B* **87**, 241401 (2013)

[11] Finck, A. D. K., Van Harlingen, D. J., Mohseni, P. K., Jung, K. & Li, X. Anomalous modulation of a zero-bias peak in a hybrid nanowire-superconductor device. *Phys. Rev. Lett.* **110**, 126406 (2013)

[12] Albrecht, S. M. *et al.* Exponential protection of zero modes in Majorana islands. *Nature* **531**, 206–209 (2016)

[13] Deng, M. T. *et al.* Majorana bound state in a coupled quantum-dot hybrid-nanowire system. *Science* **354**, 1557–1562 (2016)

[14] Chen, J. *et al.* Experimental phase diagram of a one-dimensional topological superconductor. Preprint at arxiv.org/abs/1610.04555 (2016)

[15] Liu, J., Potter, A. C., Law, K. T. & Lee, P. A. Zero-bias peaks in the tunneling conductance of spin-orbit-coupled superconducting wires with and without Majorana end-states. *Phys. Rev. Lett.* **109**, 267002 (2012)

[16] Pikulin, D. I., Dahlhaus, J. P., Wimmer, M., Schomerus, H. & Beenakker, C. W. J. A zero-voltage conductance peak from weak antilocalization in a Majorana nanowire. *New J. Phys.* **14**, 125011 (2012)

[17] Bagrets, D. & Altland, A. Class D spectral peak in Majorana quantum wires. *Phys. Rev. Lett.* **109**, 227005 (2012)

[18] Lee, E. J. H., Jiang, X., Aguado, R., Katsaros, G., Lieber, C. M. & De Franceschi, S. Zero-Bias anomaly in a nanowire quantum dot coupled to superconductors. *Phys. Rev. Lett.* **109**, 186802 (2012)

[19] Lee, E. J. H., Jiang, X., Houzet, M., Aguado, R., Lieber, C. M. & De Franceschi, S. Spin-resolved Andreev levels and parity crossings in hybrid superconductor-semiconductor nanostructures. *Nat. Nanotech.* **9**, 79–84 (2014)

[20] Takei, S., Fregoso, B. M., Hui, H.-Y., Lobos, A. M. & Das Sarma, S. Soft superconducting gap in semiconductor Majorana nanowires. *Phys. Rev. Lett.* **110**, 186803 (2013)

[21] Cheng, M., Lutchyn, R. M. & Das Sarma, S. Topological protection of Majorana qubits. *Phys. Rev. B* **85**, 165124 (2012)

[22] Rainis, D. & Loss, D. Majorana qubit decoherence by quasiparticle poisoning. *Phys. Rev. B* **85**, 174533 (2012)

[23] Chang, W. *et al.* Hard gap in epitaxial semiconductor–superconductor nanowires. *Nat. Nanotech.* **10**, 232–236 (2015)

[24] Kjaergaard, M. *et al.* Quantized conductance doubling and hard gap in a two-dimensional semiconductor–superconductor heterostructure. *Nat. Commun.* **7**, 12841 (2016)

[25] Gül, Ö. *et al.* Hard superconducting gap in InSb nanowires. *Nano Lett.* **17**, 2690–2696 (2017)

[26] Gül, Ö. *et al.* Towards high mobility InSb nanowire devices. *Nanotechnology* **26**, 215202 (2015)

[27] Kammhuber, J. *et al.* Conductance quantization at zero magnetic field in InSb nanowires. *Nano Lett.* **16**, 3482–3486 (2016)

[28] Li, S. *et al.* Coherent charge transport in ballistic InSb nanowire Josephson junctions. *Sci. Rep.* **6**, 24822 (2016)

[29] Gill, S. T., Damasco, J., Car, D., Bakkers, E. P. A. M., & Mason, N. Hybrid superconductor-quantum point contact devices using InSb nanowires. *Appl. Phys. Lett.* **109**, 233502 (2016)

[30] Gobeli, G. W. & Allen, F. G. Photoelectric properties of cleaved GaAs, GaSb, InAs, and InSb surfaces; comparison with Si and Ge. *Phys. Rev.* **137**, A245 (1965)

[31] Beenakker, C. W. J. Quantum transport in semiconductor-superconductor microjunctions. *Phys. Rev. B* **46**, 12841 (1992)

[32] Blonder, G. E., Tinkham, M. & Klapwijk, T. M. Transition from metallic to tunneling regimes in superconducting microconstrictions: Excess current, charge imbalance, and supercurrent conversion. *Phys. Rev. B* **25**, 4515 (1982)

[33] Groth, C. W., Wimmer, M., Akhmerov, A. R. & Waintal, X. Kwant: a software package for quantum transport. *New J. Phys.* **16**, 063065 (2014)

[34] Car, D., Wang, J., Verheijen, M. A., Bakkers, E. P. A. M. & Plissard, S. R. Rationally designed single-crystalline nanowire networks. *Adv. Mater.* **26**, 4875–4879 (2014)

[35] Flöhr, K. *et al.* Manipulating InAs nanowires with submicrometer precision. *Rev. Sci. Instrum.* **82**, 113705 (2011)

[36] Suyatin, D. B., Thelander, C., Björk, M. T., Maximov, I. & Samuelson, L. Sulfur passivation for ohmic contact formation to InAs nanowires. *Nanotechnology* **18**, 105307 (2007)

[37] Giannuzzi, L. A., Drown, J. L., Brown, S. R., Irwin, R. B. & Stevie, F. A. Applications of the FIB lift-out technique for TEM specimen preparation. *Microsc. Res. Tech.* **41**, 285–290 (1998)

[38] Zhang, H. *et al.* Ballistic superconductivity in semiconductor nanowires. 4TU.ResearchData doi.org/10.4121/uuid:fdeb81ab-1478-4682-9f48-dec1c83242bd (2017)

6

Ballistic Majorana nanowire devices

Önder Gül*, Hao Zhang*, Jouri D.S. Bommer*, Michiel W.A. de Moor, Diana Car, Sébastien R. Plissard, Erik P.A.M. Bakkers, Attila Geresdi, Kenji Watanabe, Takashi Taniguchi, Leo P. Kouwenhoven

Majorana modes are zero-energy excitations of a topological superconductor that exhibit non-Abelian statistics [1–3]. Following proposals for their detection in a semiconductor nanowire coupled to an s-wave superconductor [4, 5], several tunneling experiments reported characteristic Majorana signatures [6–14]. Reducing disorder has been a prime challenge for these experiments because disorder can mimic the zero-energy signatures of Majoranas [15–20], and renders the topological properties inaccessible [21–24]. Here, we show characteristic Majorana signatures in InSb nanowire devices exhibiting clear ballistic transport properties. Application of a magnetic field and spatial control of carrier density using local gates generates a zero bias peak that is rigid over a large region in the parameter space of chemical potential, Zeeman energy, and tunnel barrier potential. The reduction of disorder allows us to resolve separate regions in the parameter space with and without a zero bias peak, indicating topologically distinct phases. These observations are consistent with the Majorana theory in a ballistic system [25], and exclude for the first time the known alternative explanations that invoke disorder [15–19] or a nonuniform chemical potential [20].

This chapter has been submitted to *Nature Nanotechnology*.
*These authors contributed equally to this study.

6.1. Introduction

Semiconductor nanowires are the primary contender for realizing a topological quantum bit (qubit) based on Majorana modes [26]. Their confined geometry together with the highly tunable electronic properties readily allow for localizing Majoranas, engineering the coupling between Majoranas, and finally controlling the coupling between the topological superconductor and the external circuity. These requirements for the implementation of a Majorana qubit are challenging to achieve in other Majorana systems such as 2D and 3D topological insulators. Moreover, various basic networks [27, 28] and high-quality interfaces to different superconductors [22–24] have already been realized in semiconductor nanowires, fulfilling the further requirements for Majorana qubits [21, 26]. However, despite these advances in materials, alternative explanations have been proposed for the characteristic Majorana signatures. Most alternative explanations invoke bulk or interface disorder [15–19] or a nonuniform chemical potential along the wire [20]. Notable examples are weak antilocalization [17], Kondo effect [18], and Andreev levels [19, 20], all shown to result in transport signatures mimicking those attributed to Majoranas. Here, we show characteristic Majorana signatures in nanowire devices that exhibit ballistic transport, ruling out all known disorder- or nonuniformity-based explanations for the first time.

6.2. Results

Figure 6.1a shows the measured device consisting of an InSb nanowire (green) contacted with a grounded NbTiN superconductor (purple), and normal metal leads (yellow). The local bottom gate electrodes are separated from the nanowire by a boron nitride flake and are operated individually to allow for spatial control of the carrier density in the nanowire. We have realized our devices following our recently developed nanofabrication recipe which results in a high-quality InSb–NbTiN interface, a hard induced superconducting gap, and ballistic transport in the proximitized nanowire (see Ref. [23] and [24], and Methods). All measurements are performed in a dilution refrigerator with an electron temperature of ~ 50 mK. The data is taken by applying a bias voltage V between the normal metal lead and the superconductor indicated by N and S, respectively, and monitoring the current flow. The other normal lead is kept floating.

Figure 6.1b shows the differential conductance $\mathrm{d}I/\mathrm{d}V$ while varying V, and stepping the voltage applied to the barrier gate. Importantly, we find no signs of formation of quantum dots or any other localization effects. Vertical line cuts at the gate voltages indicated with colored bars are shown in Figure 6.1c. Figure 6.1c (bottom) is from the tunneling regime of the device where a sufficiently negative voltage on barrier gate locally depletes the noncovered nanowire section, and creates a tunnel barrier between the normal lead and the superconductor. In this regime we find an induced superconducting gap with a strong conductance suppression for subgap bias. The extracted gap value is $\Delta^* = 0.65$ meV. Increasing the voltage on barrier gate first lowers the tunnel barrier and then removes it completely. Figure 6.1c (top) is from the regime in which the noncovered nanowire section admits a single fully-transmitting transport channel. In this regime the subgap conductance is strongly enhanced due to Andreev reflection compared to the large-bias (above-gap) conductance of $2e^2/h$. The extracted enhancement factor > 1.5

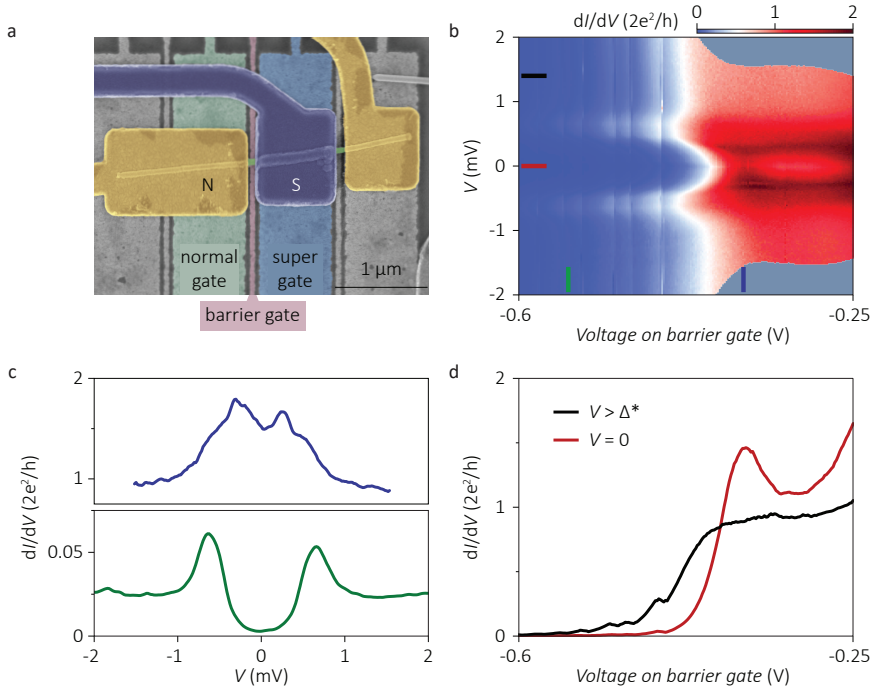

Figure 6.1 | Hybrid device and ballistic transport properties. a, False-color electron micrograph of the measured device. The InSb nanowire (green) is contacted by a grounded NbTiN superconductor (purple) and two Au normal metal leads (yellow). The nanowire has a diameter of ~ 80 nm. The local bottom gates (normal, barrier, and super gate) are separated from the nanowire by a boron nitride flake (~ 30 nm) and are operated individually. Two-terminal measurements are performed between N and S, while the other normal lead is floating. **b,** Differential conductance $\mathrm{d}I/\mathrm{d}V$ as a function of bias voltage V, and voltage on barrier gate (the other gate electrodes are grounded). Vertical lines at certain gate voltages are due to slow fluctuations in the electrostatic environment. **c,** Vertical line cuts from **b** at the gate voltages marked with colored bars. Top panel shows the $\mathrm{d}I/\mathrm{d}V$ from the transport regime in which the current is carried by a single fully-transmitting channel. We find an enhancement of conductance at small bias by more than a factor of 1.5 compared to the large-bias conductance of $2e^2/h$. Bottom panel is from the tunneling regime in which the current is carried by a single channel with low transmission. We extract an induced superconducting gap $\Delta^* = 0.65$ meV. **d,** Horizontal line cuts from **b** at the bias voltages marked with colored bars. Subgap conductance ($V = 0$) shows an enhancement reaching $1.5 \times 2e^2/h$ when the large-bias conductance ($V = 1.4\,\mathrm{mV} > \Delta^*$) has a quantized value of $2e^2/h$.

implies a contact interface transparency > 0.93 [24]. Figure 6.1d shows the horizontal line cuts from Figure 6.1b at the bias voltages indicated with colored bars. For a bias $V > \Delta^*$ we find a quantized conductance plateau at $2e^2/h$, a clear signature of a ballistic device. For zero bias voltage the strong Andreev enhancement is evident in the plateau region followed by a dip in conductance due to channel mixing [24]. From the absence of quantum dots, the observed induced gap with a strongly reduced subgap density of states, high interface transparency, and quantized conductance, we conclude a very low disorder strength for our device, consistent with our recent findings [24].

We now turn to the tunneling regime of the device where Majorana modes are char-

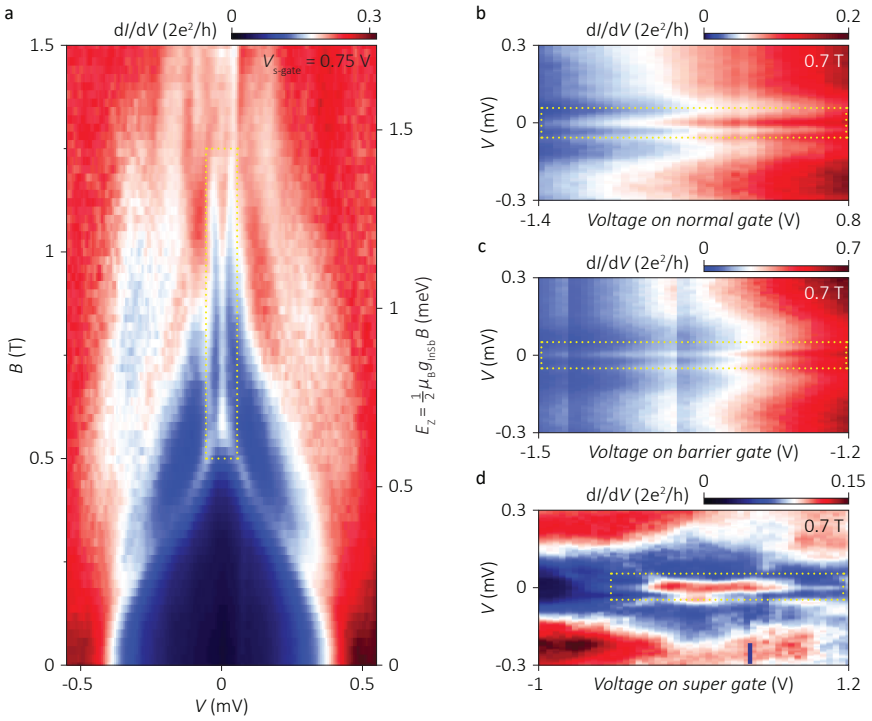

Figure 6.2 | Zero bias peak and its dependence on magnetic field and local gate voltages. a, Differential conductance $\mathrm{d}I/\mathrm{d}V$ as a function of bias voltage V, and an external magnetic field B along the nanowire axis for $V_{\mathrm{s-gate}} = 0.75$ V. The magnetic field closes the induced gap at 0.55 T and generates a zero bias peak which persists up to 1.2 T. The right axis scales with Zeeman energy E_z assuming a g factor of 40 obtained independently [29, 30]. (Voltage on normal and barrier gate: 0 V and −1.4 V) **b,** $\mathrm{d}I/\mathrm{d}V$ as a function of V and voltage on normal gate. The voltage on normal gate changes the conductance by more than a factor of 5 but does not affect the presence of the zero bias peak. **c,** $\mathrm{d}I/\mathrm{d}V$ as a function of V and voltage on barrier gate. The voltage on barrier gate changes the conductance by nearly an order of magnitude but does not affect the presence of zero bias peak. **d,** $\mathrm{d}I/\mathrm{d}V$ as a function of V and voltage on super gate. The zero bias peak persists for a finite gate voltage range. The blue bar indicates the voltage on super gate in **a**, **b** and **c**. Voltage on tunnel gate is adjusted to keep the overall conductance the same when sweeping the voltage on super gate.

acterized by a zero bias peak. To drive the nanowire device into the topological phase, we apply a magnetic field B along the wire axis and tune the voltage applied to the super gate ($V_{\mathrm{s-gate}}$) which controls μ, the chemical potential in the nanowire section underneath the superconductor. Figure 6.2a shows that an increasing B closes the induced gap at 0.55 T and generates a zero bias peak rigidly bound to $V = 0$ up to 1.2 T (line cuts in Suppl. Figure 6.S1a). The gap closure is expected to occur for a Zeeman energy $E_z \gtrsim \Delta^*$. From linear interpolation we find $g \gtrsim 40$ which matches our independent measurements [29, 30]. Converting the B axis into a Zeeman energy E_z scale (right vertical axis), we find that the zero bias peak is bound to zero over 0.75 meV, a range in Zeeman energy that is 30 times larger than the peak width (the full width at half maximum, FWHM ~ 20 μeV, see Suppl. Figure 6.S1c and Suppl. Figure 6.S4). This excludes a level crossing as the origin for our zero bias peak [18]. We note that all our devices show a

significant increase of subgap density of states for the magnetic fields required for topological phase transition. This behavior is likely due to vortex formation or a short mean free path [31] in our NbTiN film, and is a subject of our future studies. The formation of vortices is speculated to create a dissipation channel [25], the leading hypothetical mechanism that limits our zero bias peak height from reaching the quantized value of $2e^2/h$. An unambiguous observation of a zero bias peak quantization remains an outstanding challenge for Majorana experiments in semiconductor nanowires.

The origin of zero bias peak can be spatially resolved by varying the voltages applied to individual gates. Figure 6.2b shows that the presence of the zero bias peak is not affected when gating the wire section underneath the normal contact which changes the conductance by more than a factor of 5 (see also Suppl. Figure 6.S1d). Extending the same analysis to the noncovered wire section yields the same result (Figure 6.2c), i.e., changing the tunnel barrier conductance by nearly an order of magnitude does not split the zero bias peak, nor makes it disappear (see also Suppl. Figure 6.S1e). In contrast, Figure 6.2d shows that the zero bias peak is present over a finite range in voltage applied to the super gate (line cuts in Suppl. Figure 6.S1f). This indicates that proper tuning of μ is essential for the appearance of the zero bias peak. The observation of a zero bias peak that does not split when changing the tunnel barrier conductance (Figure 6.2c) excludes Kondo effect [18] and crossing of Andreev levels [19] as the origin of our zero bias peak. Most importantly, it rules out an explanation provided by recent theory work [20] demonstrating trivial Andreev levels localized near the noncovered wire section that are bound to zero energy for varying E_z and μ, but quickly split to finite energies for varying tunnel barrier strength. Here we demonstrate for the first time a zero bias peak rigidly bound to $V = 0$ over a changing tunnel barrier conductance—a behavior observed in all devices (Suppl. Figure 6.S5-6.S7). From the combined analysis (Figure 6.2b-d) we conclude that the zero bias peak originates in the wire section underneath the superconductor, consistent with a Majorana interpretation.

In a Majorana nanowire [4, 5], the existence of a topological phase strictly requires an external magnetic field with a finite component perpendicular to the spin–orbit field B_{so}, see Figure 6.3a. An external field along the wire fulfills this requirement, shown in Figure 6.2a. In contrast, Figure 6.3b shows that an external magnetic field parallel to B_{so} does not generate a zero bias peak for the same gate settings in Figure 6.2a. Figure 6.3c shows the dependence of the zero bias peak on the direction of the external field. The zero bias peak is limited to an angle range where the external field is mostly aligned with the wire, perpendicular to B_{so} (see Suppl. Figure 6.S2 for a measurement in a larger angle range). We observe a low conductance region around the zero bias peak, indicating the induced gap. Orienting the magnetic field away from the wire axis and more towards B_{so} closes the induced gap and splits the zero bias peak. This is indicated by the vertical line cuts from Figure 6.3c at marked angles, shown in Figure 6.3d. A gap closing is expected for the critical angle φ_c given by the projection rule [32, 33] $E_z \sin(\varphi_c) = \Delta^*$. From the observed gap $\Delta^* = 175\,\mu$eV at $B = 0.575$ T and a g factor of 40, we obtain $\varphi_c = 15°$, agreeing well with observed value of $\varphi_c \sim 10°$ (a reduction in φ_c is expected due to orbital effect of the external magnetic field [34]). Finally, in Suppl. Figure 6.S2 we show that increasing B decreases φ_c, a behavior consistent with the projection rule.

We now turn our attention to an identical device but with a longer proximitized wire

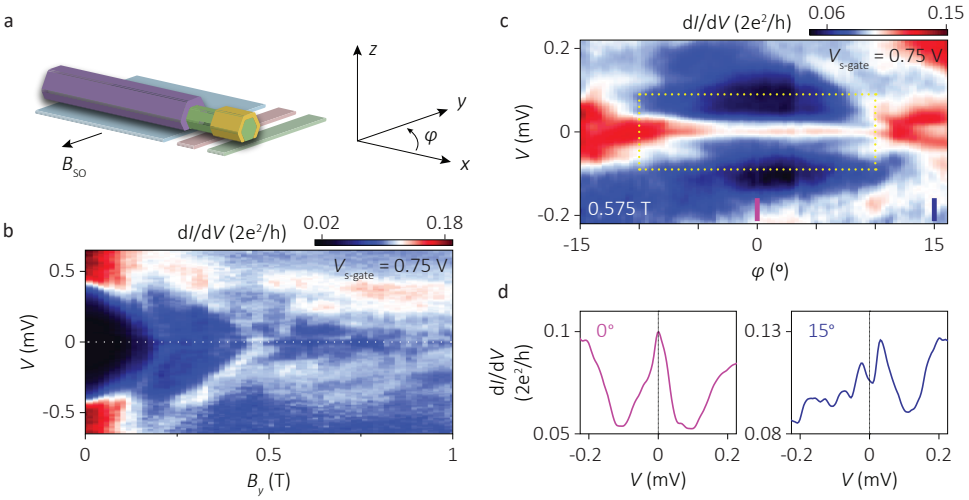

Figure 6.3 | Dependence of zero bias peak on magnetic field orientation. **a,** Orientation of the nanowire device. The wire is along x and the spin–orbit field B_{SO} is along y. The substrate plane is spanned by x and y. φ is the angle between the x axis and the orientation of the external magnetic field in the plane of the substrate. **b,** Differential conductance dI/dV as a function of bias voltage V, and an external magnetic field along the y axis. Application of a magnetic field along B_{SO} closes the induced gap but does not generate a zero bias peak. **c,** dI/dV as a function of V, and in-plane rotation of the magnetic field with a magnitude of 0.575 T. The zero bias peak appears in an angle range in which the external magnetic field is mostly aligned with the wire. We attribute the low conductance region around the zero bias peak to the induced gap. Orienting the magnetic field away from the wire axis and more towards B_{SO} closes the induced gap and splits the zero bias peak (see line cuts in **d**). **d,** Vertical line cuts from **c** at the angles indicated with colored bars. For $\varphi = 0°$ the zero bias peak is present, which is split for $\varphi = -15°$.

section (1.2 μm, see Suppl. Figure 6.S3a). Figure 6.4a-c show an induced gap $\Delta^* = 0.9$ meV at zero magnetic field, significantly larger than the device in Figure 6.1-6.3. As a result, the induced gap closes at a higher magnetic field (~ 1 T). The zero bias peak is visible and unsplit over a range of at least 1.3 T, corresponding to a Zeeman energy scale > 1.5 meV. The FWHM is around 0.07 meV yielding a ratio ZBP-range/FWHM $\gtrsim 20$ (Suppl. Figure 6.S4). A disorder-free Majorana theory model with parameters extracted from this device (geometry, induced gap, spin–orbit coupling, temperature) finds perfect agreement between simulation [25] and our data (Figure 6.4a). Suppl. Figure 6.S3b and c shows that the zero bias peak position is robust against a change in conductance when varying the voltage applied to the normal and the barrier gate, ruling out the trivial Andreev-level explanation [20] consistent with our earlier discussion (Figure 6.2b and c). In contrast to normal and barrier gate, the voltage applied to the super gate changes the onset and the end of the zero bias peak in magnetic field. Figure 6.4d shows that for $V_{s-gate} = -10$ V the zero bias peak appears at a higher magnetic field compared to Figure 6.4a where $V_{s-gate} = -7$ V (1.66 T vs. 1.22 T). We have extended this analysis for $-10\,\text{V} \leq V_{s-gate} \leq 0\,\text{V}$ and marked the magnetic field values at which the zero bias peak starts and ends (Suppl. Figure 6.S3d). The resulting phase diagram is shown in Figure 6.4e. For large negative voltages applied to the super gate, we find a region in which the zero bias peak persists for large ranges of magnetic field and V_{s-gate}, indicating the

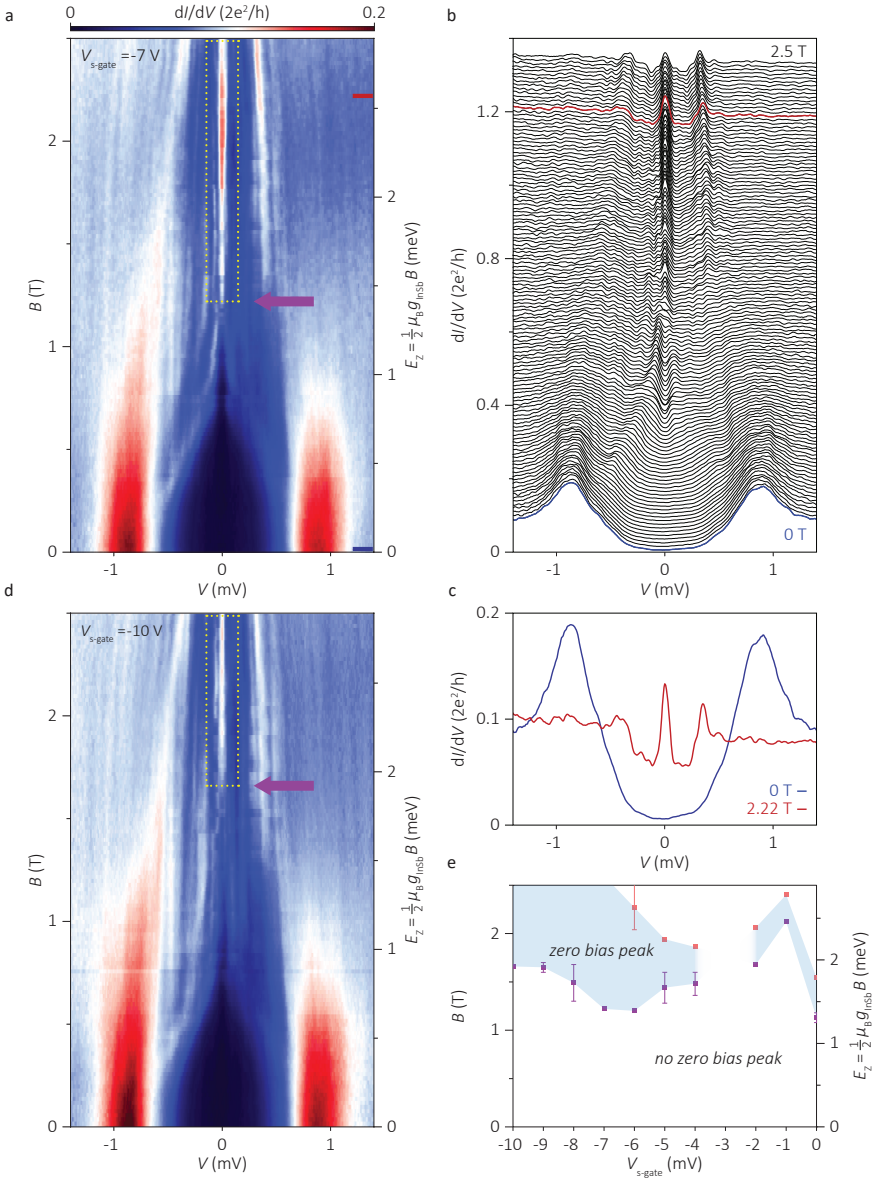

Figure 6.4 | Zero bias peak and phase diagram. **a,** Differential conductance $\mathrm{d}I/\mathrm{d}V$ of another device measured as a function of bias voltage V, and an external magnetic field B along the nanowire axis. We find an induced gap $\Delta^* = 0.9$ meV at zero magnetic field. Increasing the magnetic field closes the induced gap at ~1 T and generates a zero bias peak that persists up to at least 2.5 T. The right axis scales with Zeeman energy E_z assuming $g_{\mathrm{InSb}} = 40$ obtained independently [29, 30]. The purple arrow at 1.22 T indicates the onset of the zero bias peak. **b,** Line cuts from **a** with $0.01 \times 2e^2/h$ offset. **c,** Line cuts from **a** and **b** at 0 and 2.22 T. **d,** Same as **a** but with a different super gate voltage $V_{\mathrm{s-gate}} = -10$ V. For this super gate voltage, the onset of the zero bias peak is at a larger magnetic field of 1.66 T, as marked by a purple arrow. **e,** Phase diagram constructed by the onset and the end of the zero bias peak in magnetic field for different super gate voltages. The purple squares denote the onset, pink the end. For $V_{\mathrm{s-gate}} = -3$ V no zero bias peak is observed.

topological phase. We attribute the appearance of a trivial phase at large magnetic fields above the topological phase to multi-channel occupation in the proximitized wire section [20, 25]. A precise knowledge of the phase boundaries requires theory including finite-size effects [35], the orbital effect of the magnetic field [34], and an accurate electrostatic modeling of the device [36], and will be addressed in future studies.

In conclusion, the presented experiments demonstrate zero bias peaks over an extended range in Zeeman energy and gate voltage in devices that show clear ballistic transport properties, and reveal the distinct phases in the topology of Majorana wires. These observations exclude all known alternative explanations for our zero bias peaks that are based on disorder.

Methods

Nanowire growth and device fabrication. InSb nanowires have been grown by Au-catalyzed Vapor-Liquid-Solid mechanism in a Metal Organic Vapor Phase Epitaxy reactor. The InSb nanowires are zinc blende, along [111] crystal direction, and are free of stacking faults and dislocations [37]. As-grown nanowires are deposited one-by-one using a micro-manipulator [38] on a substrate patterned with local gates covered by a ~ 30 nm thick hBN dielectric. The contact deposition process starts with resist development followed by oxygen plasma cleaning. Then, the chip is immersed in a sulfur-rich ammonium sulfide solution diluted by water (with a ratio of 1:200) at 60°C for half an hour [39]. At all stages care is taken to expose the solution to air as little as possible. For normal metal contacts [29, 30], the chip is placed into an evaporator. A 30 second helium ion milling is performed in situ before evaporation of Cr/Au (10 nm/125 nm) at a base pressure $< 10^{-7}$ mbar. For superconducting contacts [23, 24], the chip is mounted in a sputtering system. After 5 seconds of in situ argon plasma etching at a power of 25 Watts and a pressure of 10 mTorr, 5 nm NbTi is sputtered followed by 85 nm NbTiN.

Acknowledgments

We thank A.R. Akhmerov, O.W.B. Benningshof, M.C. Cassidy, S. Goswami, J. Kammhuber, V. Mourik, M. Quintero-Pérez, J. Shen, M. Wimmer, D.J. van Woerkom, and K. Zuo for discussions and assistance. This work has been supported by the Netherlands Organisation for Scientific Research (NWO), European Research Council (ERC), and Microsoft Corporation Station Q.

Author contributions

Ö.G., H.Z., and J.D.S.B fabricated the devices, performed the measurements, and analyzed the data. M.W.A.d.M. contributed to the device fabrication. D.C., S.P. and E.P.A.M.B. grew the InSb nanowires. A.G. contributed to the experiments. K.W. and T.T. synthesized the hBN crystals. L.P.K. supervised the project. Ö.G., H.Z., and J.D.S.B co-wrote the paper. All authors commented on the manuscript.

6.S. Supplementary Information

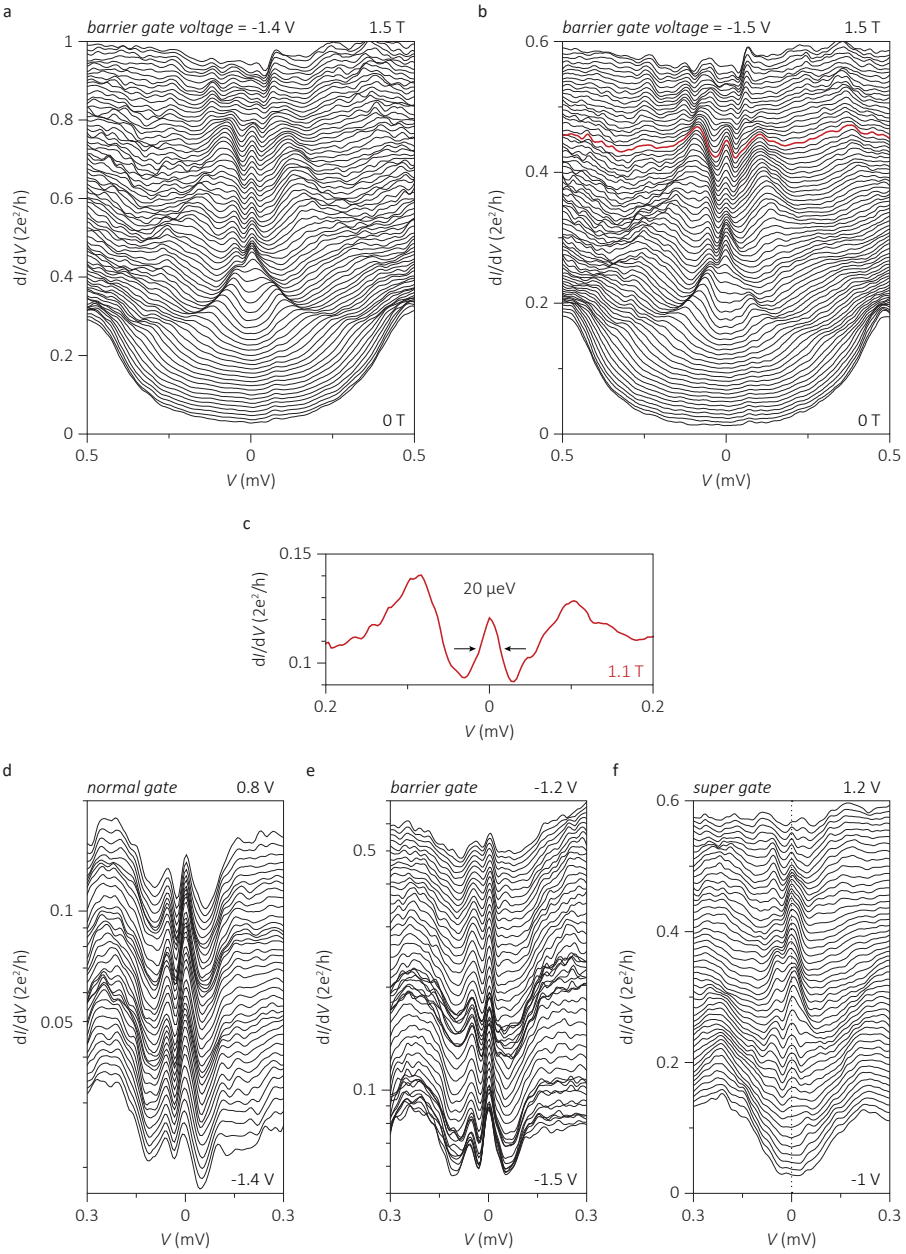

Figure 6.S1 | Line cuts from Figure 6.2. a, Line cuts from Figure 6.2a with $0.01 \times 2e^2/h$ offset. An increasing magnetic field closes the induced gap at 0.55 T and generates a zero bias peak up to 1.2 T. **b,** Same as **a** but for a larger tunnel barrier strength. Offset: $0.006 \times 2e^2/h$. **c,** Line cut from 1.1 T. We find the full width at half maximum of the zero bias peak to be 20 μeV. **d,** Line cuts from Figure 6.2b in logarithmic scale (without offset). A variation in voltage on the normal gate ($-1.4\,\mathrm{V} \leq V_{\mathrm{n-gate}} \leq 0.8\,\mathrm{V}$) changes the conductance by more than a factor of 5, but does not remove the zero bias peak. **e,** Line cuts from Figure 6.2c in logarithmic scale (without offset). A variation in voltage on the barrier gate ($-1.5\,\mathrm{V} \leq V_{\mathrm{b-gate}} \leq -1.2\,\mathrm{V}$) changes the conductance by nearly an order of magnitude, but does not remove the zero bias peak. **f,** Line cuts from Figure 6.2d with $0.006 \times 2e^2/h$ offset. A variation in voltage on the super gate ($-1\mathrm{V} \leq V_{\mathrm{s-gate}} \leq 1.2\,\mathrm{V}$) affects the presence of the zero bias peak, which is stable for a finite gate voltage range.

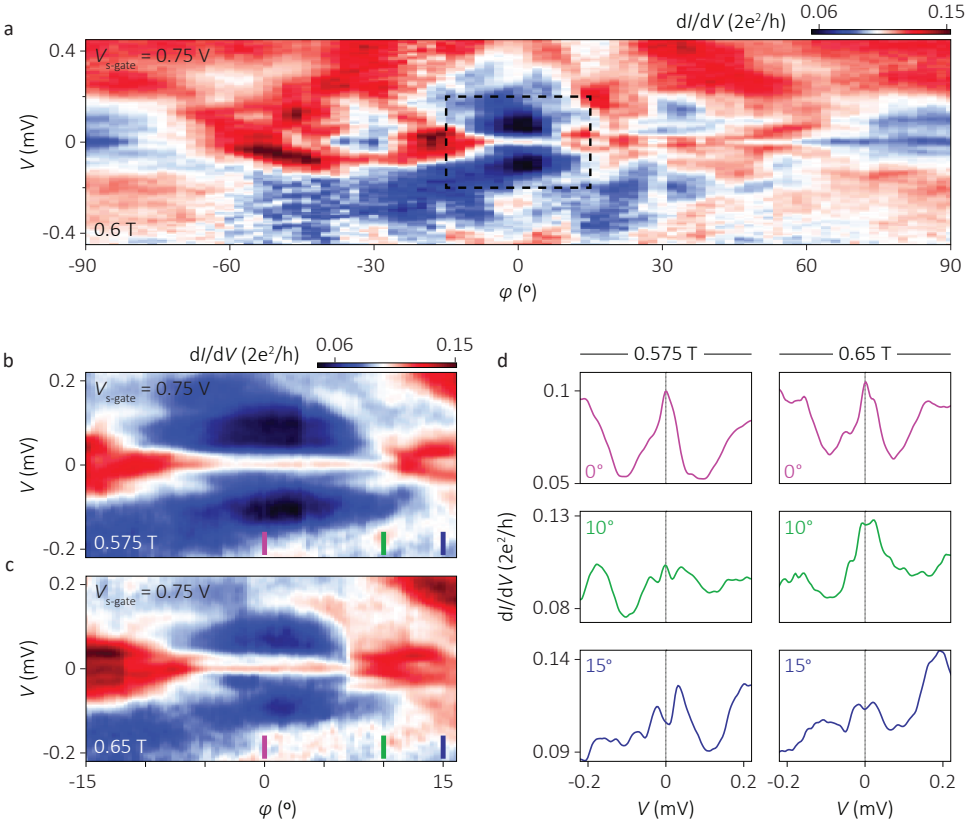

Figure 6.S2 | Dependence of the zero bias peak on the orientation of an in-plane magnetic field. **a,** Differential conductance $\mathrm{d}I/\mathrm{d}V$ as a function of bias voltage V, and in-plane rotation of the magnetic field with a magnitude of 0.6 T. $\varphi = 0°$ corresponds to an external field along the wire, $\varphi = \pm 90°$ to an external field parallel to the spin–orbit field B_{so}. The zero bias peak is present in an angle range ($|\varphi| < 10°$) when the external magnetic field is mostly aligned with the wire. We observe a low conductance region around the zero bias peak, indicating the induced gap. Orienting the magnetic field away from the wire axis and more towards B_{so} closes the induced gap and splits the zero bias peak. We do not observe a stable zero bias peak for $|\varphi| > 10°$ in the entire angle range. The dashed square indicates the angle range shown in Figure 6.3c. **b, c,** $\mathrm{d}I/\mathrm{d}V$ as a function of V, and in-plane rotation of the magnetic field with two different magnitudes. Increasing the magnetic field decreases the angle range of the zero bias peak (compare **b** and **c**). **d,** Vertical line cuts from **b** and **c** at the angles indicated with colored bars. Top panels: For $\varphi = 0°$ the zero bias peak is present for both magnetic field magnitudes. Bottom panels: For $\varphi = 15°$ no zero bias peak is present for both magnitudes. Middle panels: For $\varphi = 10°$ the zero bias peak is present only for 0.575 T, while is split for 0.65 T.

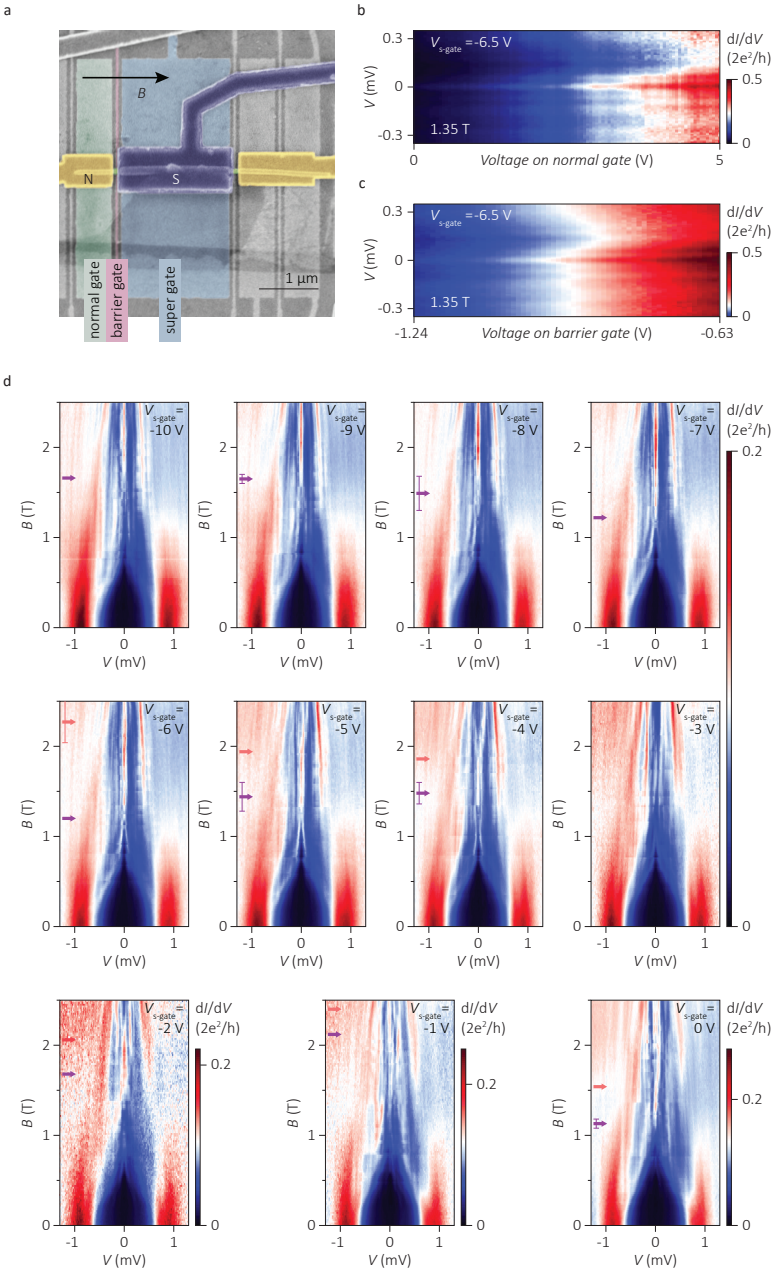

Figure 6.S3 | Zero bias peak in a large range of magnetic field and local gate voltages. a, False-color electron micrograph of the measured device. **b, c,** Differential conductance $\mathrm{d}I/\mathrm{d}V$ as a function of bias voltage V, and voltages on normal and barrier gate, respectively. A variation in each gate voltage changes the conductance by an order of magnitude, but does not affect the presence of the zero bias peak. **d,** $\mathrm{d}I/\mathrm{d}V$ as a function of V and an external magnetic field B along the nanowire axis, measured at different voltages on super gate ($-10\,\mathrm{V} \leq V_{\mathrm{s-gate}} \leq 0\,\mathrm{V}$). A variation in $V_{\mathrm{s-gate}}$ changes the magnetic field range in which the zero bias peak appears. The purple (pink) arrows indicate the onset (end) of the zero bias peak in external magnetic field. When changing the super gate voltage, we adjust the tunnel gate voltage to keep the overall conductance the same.

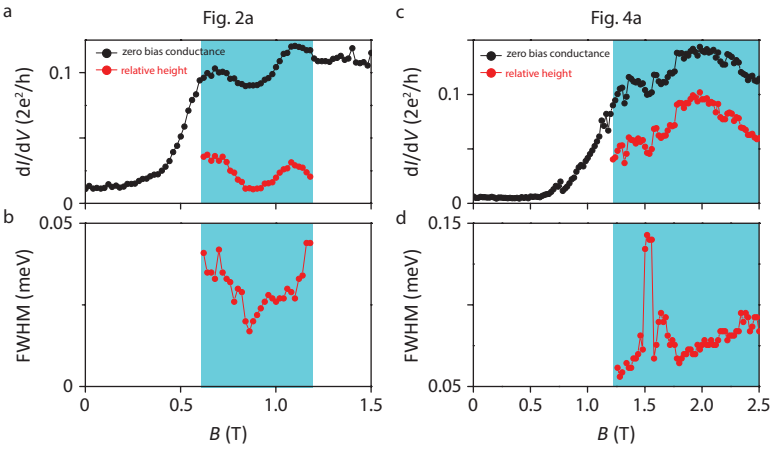

Figure 6.S4 | Zero bias peak height and width. **a,** The absolute and the relative height of the zero bias peak extracted from Figure 6.2a. The difference between the absolute and the relative height is the subgap conductance around zero bias for each magnetic field. **b,** The full width at half maximum (FWHM) of the zero bias peak extracted from Figure 6.2a. **c, d,** Same as **a** and **b** but for the zero bias peak from Figure 6.4a.

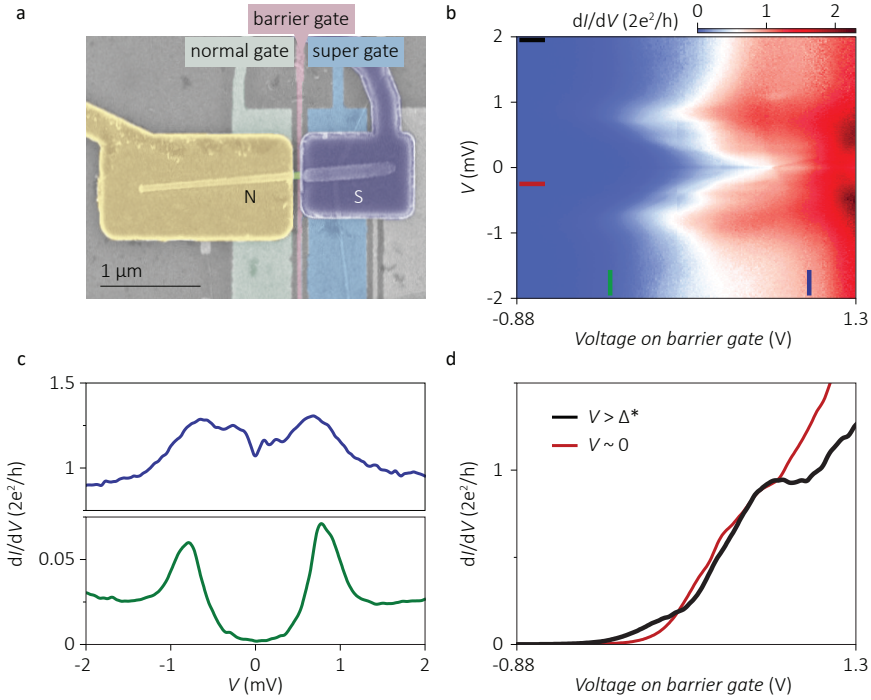

Figure 6.S5 | Additional device 1 - ballistic transport properties. **a,** False-color electron micrograph of the measured device. **b,** Differential conductance $\mathrm{d}I/\mathrm{d}V$ as a function of bias voltage V, and voltage on barrier gate. **c,** Vertical line cuts from **b** at the gate voltages marked with colored bars. Top panel shows the $\mathrm{d}I/\mathrm{d}V$ from the transport regime in which the current is carried by a single fully-transmitting channel. We find an enhancement of conductance at small bias by a factor of 1.25 compared to the large-bias conductance of $2e^2/h$. Bottom panel is from the tunneling regime. We extract an induced superconducting gap $\Delta^* = 0.75$ meV. **d,** Horizontal line cuts from **b** at the bias voltages marked with colored bars. Large-bias conductance ($V = 2\,\mathrm{mV} > \Delta^*$) shows a quantized plateau of $2e^2/h$. The subgap conductance ($V = -0.25\,\mathrm{mV}$) is enhanced within the gate voltage range in which the large-bias conductance is quantized. We excluded a series resistance of 0.5 kΩ, solely to account for the contact resistance of the normal lead [3, 4].

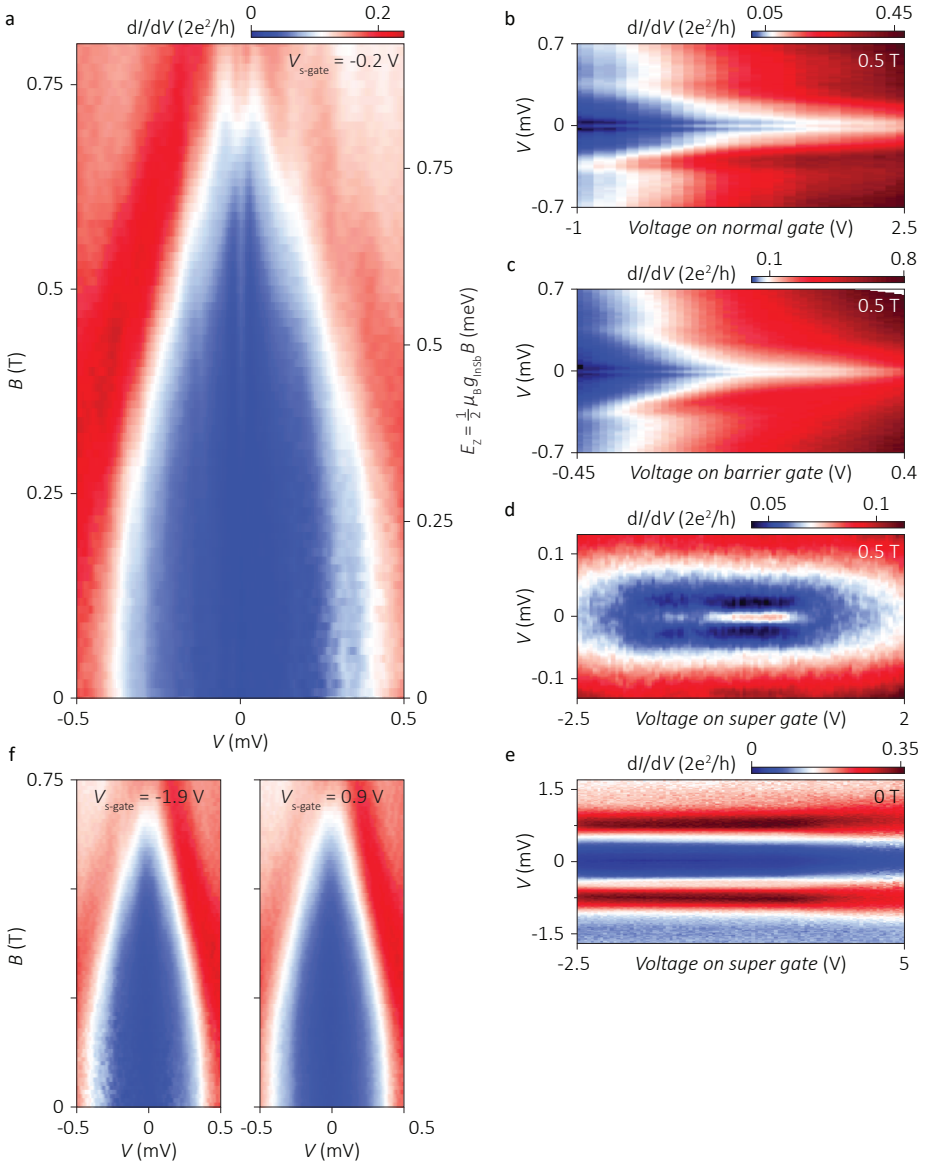

Figure 6.S6 | Additional device 1 - zero bias peak in a large range of magnetic field and local gate voltages. **a,** Differential conductance $\mathrm{d}I/\mathrm{d}V$ as a function of bias voltage V, and an external magnetic field B along the nanowire axis. Application of a magnetic field generates a zero bias peak at 0.3 T. The zero bias peak persists up to 0.7 T and splits for larger magnetic fields. The right axis scales with Zeeman energy E_z assuming a g factor of 40. **b,** $\mathrm{d}I/\mathrm{d}V$ as a function of V and voltage on the normal gate. The voltage on the normal gate changes the conductance by a factor of 10 but does not affect the presence of the zero bias peak. **c,** $\mathrm{d}I/\mathrm{d}V$ as a function of V and voltage on the barrier gate. The voltage on the barrier gate changes the conductance by a factor of 20 but does not affect the presence of the zero bias peak. **d,** $\mathrm{d}I/\mathrm{d}V$ as a function of V and voltage on the super gate. The zero bias peak is stable for a finite range of voltages on the super gate. **e,** Same as **d** but at zero magnetic field. No zero bias peak is present. **f,** Same as **a** but for different voltages on the super gate ($V_{\mathrm{s-gate}}$). No zero bias peak is present for the measured magnetic field range for $V_{\mathrm{s-gate}} = -1.9\,\mathrm{V}$ and $V_{\mathrm{s-gate}} = 0.9\,\mathrm{V}$, consistent with **d**.

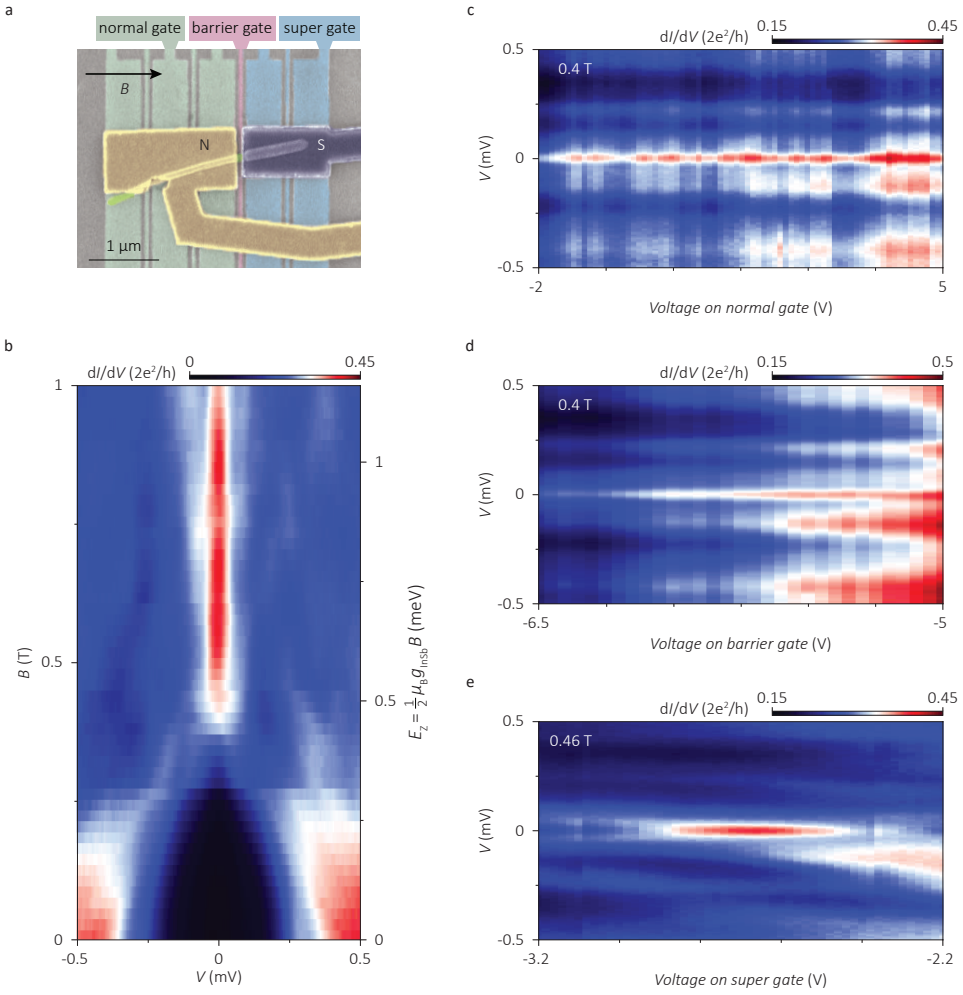

Figure 6.S7 | Additional device 2 - zero bias peak in a large range of magnetic field and local gate voltages. **a,** False-color electron micrograph of the measured device. **b,** Differential conductance $\mathrm{d}I/\mathrm{d}V$ as a function of bias voltage V and magnetic field B. Increasing the magnetic field closes the gap and generates a zero bias peak which persists up to at least 1 T. The right axis scales with Zeeman energy assuming $g_{\mathrm{InSb}} = 40$. Gate voltages are fixed at $V_{\mathrm{n-gate}} = 1\,\mathrm{V}$, $V_{\mathrm{b-gate}} = -5.5\,\mathrm{V}$, and $V_{\mathrm{s-gate}} = -2.8\,\mathrm{V}$ for normal, barrier, and super gate, respectively. **c,** $\mathrm{d}I/\mathrm{d}V$ as a function of V, and normal gate voltage $V_{\mathrm{n-gate}}$. A large variation in $V_{\mathrm{n-gate}}$ can modulate the overall conductance but it does not remove the zero bias peak. Taken at $B = 0.4\,\mathrm{T}$, $V_{\mathrm{b-gate}} = -5.5\,\mathrm{V}$, and $V_{\mathrm{s-gate}} = -2.85\,\mathrm{V}$. **d,** $\mathrm{d}I/\mathrm{d}V$ as a function of V, and barrier gate voltage. Changing the tunnel barrier conductance by more than a factor of 3 does not split the zero bias peak, nor makes it disappear. Taken at $V_{\mathrm{n-gate}} = 2.5\,\mathrm{V}$ and $V_{\mathrm{s-gate}} = -2.85\,\mathrm{V}$. **e,** $\mathrm{d}I/\mathrm{d}V$ as a function of V, and super gate voltage $V_{\mathrm{s-gate}}$. The zero bias peak is stable over a finite range in $V_{\mathrm{s-gate}}$. Taken at $V_{\mathrm{n-gate}} = 1\,\mathrm{V}$ and $V_{\mathrm{b-gate}} = -5.5\,\mathrm{V}$.

References

[1] Read, N. & Green, D. Paired states of fermions in two dimensions with breaking of parity and time-reversal symmetries and the fractional quantum Hall effect. *Phys. Rev. B* **61,** 10267 (2000)

[2] Kitaev, A. Y. Unpaired Majorana fermions in quantum wires. *Phys. Usp.* **44,** 131-136 (2001)

[3] Fu, L. & Kane, C. L. Superconducting proximity effect and Majorana fermions at the surface of a topological insulator. *Phys. Rev. Lett.* **100,** 096407 (2008)

[4] Lutchyn, R. M., Sau, J. D. & Das Sarma, S. Majorana fermions and a topological phase transition in semiconductor-superconductor heterostructures. *Phys. Rev. Lett.* **105,** 077001 (2010)

[5] Oreg, Y., Refael, G. & von Oppen, F. Helical liquids and Majorana bound states in quantum wires. *Phys. Rev. Lett.* **105,** 177002 (2010)

[6] Mourik, V. et al. Signatures of Majorana fermions in hybrid superconductor-semiconductor nanowire devices. *Science* **336,** 1003-1007 (2012)

[7] Das, A. et al. Zero-bias peaks and splitting in an Al-InAs nanowire topological superconductor as a signature of Majorana fermions. *Nature Phys.* **8,** 887-895 (2012)

[8] Rokhinson, L. P., Liu, X. & Furdyna, J. K. The fractional a.c. Josephson effect in a semiconductor–superconductor nanowire as a signature of Majorana particles. *Nature Phys.* **8,** 795-799 (2012)

[9] Deng, M. T. et al. Anomalous zero-bias conductance peak in a Nb–InSb nanowire–Nb hybrid device. *Nano Lett.* **12,** 6414-6419 (2012)

[10] Churchill, H. O. H. et al. Superconductor-nanowire devices from tunneling to the multichannel regime: Zero-bias oscillations and magnetoconductance crossover. *Phys. Rev. B* **87,** 241401(R) (2013)

[11] Finck, A. D. K., Van Harlingen, D. J., Mohseni, P. K., Jung, K. & Li, X. Anomalous modulation of a zero-bias peak in a hybrid nanowire-superconductor device. *Phys. Rev. Lett.* **110,** 126406 (2013)

[12] Albrecht, S. M. et al. Exponential protection of zero modes in Majorana islands. *Nature* **531,** 206-209 (2016)

[13] Deng, M. T. et al. Majorana bound state in a coupled quantum-dot hybrid-nanowire system. *Science* **354,** 1557-1562 (2016)

[14] Chen, J. et al. Experimental phase diagram of a one-dimensional topological superconductor. arXiv:1610.04555 (2016)

[15] Liu, J., Potter, A. C., Law, K. T. & Lee, P. A. Zero-bias peaks in the tunneling conductance of spin-orbit-coupled superconducting wires with and without Majorana end-states. *Phys. Rev. Lett.* **109,** 267002 (2012)

[16] Bagrets, D. & Altland, A. Class D spectral peak in Majorana quantum wires. *Phys. Rev. Lett.* **109,** 227005 (2012)

[17] Pikulin, D. I., Dahlhaus, J. P., Wimmer, M., Schomerus, H. & Beenakker, C. W. J. A zero-voltage conductance peak from weak antilocalization in a Majorana nanowire. *New J. Phys.* **14,** 125011 (2012)

[18] Lee, E. J. H. et al. Zero-Bias anomaly in a nanowire quantum dot coupled to superconductors. *Phys. Rev. Lett.* **109,** 186802 (2012)

[19] Lee, E. J. H. et al. Spin-resolved Andreev levels and parity crossings in hybrid superconductor-semiconductor nanostructures. *Nature Nanotech.* **9,** 79-84 (2014)

[20] Liu, C.-X., Sau, J. D., Stanescu, T. D. & Das Sarma, S. Andreev bound states versus Majorana bound states in quantum dot-nanowire-superconductor hybrid structures: Trivial versus topological zero-bias conductance peaks. arXiv:1705.02035 (2017)

[21] Takei, S., Fregoso, B. M., Hui, H.-Y., Lobos, A. M. & Das Sarma, S. Soft superconducting gap in semiconductor Majorana nanowires. *Phys. Rev. Lett.* **110,** 186803 (2013)

[22] Chang, W. et al. Hard gap in epitaxial semiconductor–superconductor nanowires. *Nature Nanotech.* **10,** 232-236 (2015)

[23] Gül, Ö. et al. Hard superconducting gap in InSb nanowires. *Nano Lett.* **17,** 2690-2696 (2017)

[24] Zhang, H. et al. Ballistic superconductivity in semiconductor nanowires. *Nature Commun.* **8,** 16025 (2017)

[25] Liu, C.-X., Sau, J. D. & Das Sarma, S. Role of dissipation in realistic Majorana nanowires. *Phys. Rev. B* **95,** 054502 (2017)

[26] Beenakker, C. W. J. Search for Majorana fermions in superconductors. *Annu. Rev. Condens. Matter Phys.* **4,** 113-136 (2013)

[27] Plissard, S. R. et al. Formation and electronic properties of InSb nanocrosses. *Nature Nanotech.* **8,** 859-864 (2013)

[28] Gooth, J. et al. Ballistic one-dimensional InAs nanowire cross-junction interconnects. *Nano Lett.* **17,** 2596-2602 (2017)

[29] Kammhuber, J. et al. Conductance quantization at zero magnetic field in InSb nanowires. *Nano Lett.* **16,** 3482-3486 (2016)

[30] Kammhuber, J. et al. Conductance through a helical state in an InSb nanowire. arXiv:1701.06878 (2017)

[31] Cole, W. S., Sau, J. D. & Das Sarma, S. Proximity effect and Majorana bound states in clean semiconductor nanowires coupled to disordered superconductors. *Phys. Rev. B* **94,** 150505(R) (2017)

[32] Osca, J., Ruiz, D., & Serra, L. Effects of tilting the magnetic field in one-dimensional Majorana nanowires. *Phys. Rev. B* **89,** 245405 (2014)

[33] Rex, S. & Sudbø, A. Tilting of the magnetic field in Majorana nanowires: critical angle and zero-energy differential conductance. *Phys. Rev. B* **90,** 115429 (2014)

[34] Nijholt, B. & Akhmerov, A. R. Orbital effect of magnetic field on the Majorana phase diagram. *Phys. Rev. B* **93,** 235434 (2016)

[35] Mishmash, R. V., Aasen, D., Higginbotham, A. P. & Alicea, J. Approaching a topological phase transition in Majorana nanowires. *Phys. Rev. B* **93,** 245404 (2016)

[36] Vuik, A., Eeltink, D., Akhmerov, A. R. & Wimmer, M. Effects of the electrostatic environment on the Majorana nanowire devices. *New J. Phys.* **18,** 033013 (2016)

[37] Car, D., Wang, J., Verheijen, M. A., Bakkers, E. P. A. M. & Plissard, S. R. Rationally designed single-crystalline nanowire networks. *Adv. Mater.* **26,** 4875-4879 (2014)

[38] Flöhr, K. et al. Manipulating InAs nanowires with submicrometer precision. *Rev. Sci. Instrum.* **82,** 113705 (2011)

[39] Suyatin, D. B., Thelander, C., Björk, M. T., Maximov, I. & Samuelson, L. Sulfur passivation for ohmic contact formation to InAs nanowires. *Nanotechnology* **18,** 105307 (2007)

7

Conclusion

In this chapter we highlight the conclusion of the reported experiments in each chapter, discuss the shortcomings of our approach, and suggest future directions.

Chapter 3

Using a model consisting of a nanowire-transistor with contact resistances allowed us to systematically study the InSb nanowire mobility, which we found to be limited by adsorbents on the nanowire surface and/or the substrate. After optimizing the fabrication parameters accordingly, we reproducibly obtained mobility values that are among the highest in the nanowire literature. Nevertheless our average mobility values of 25 000 cm^2/Vs are well below the mobilities of the state-of-the-art two-dimensional III–V systems. For instance Ref. [1] reports 200 000 cm^2/Vs for InSb quantum wells. This suggests that there is big room for further improvement.

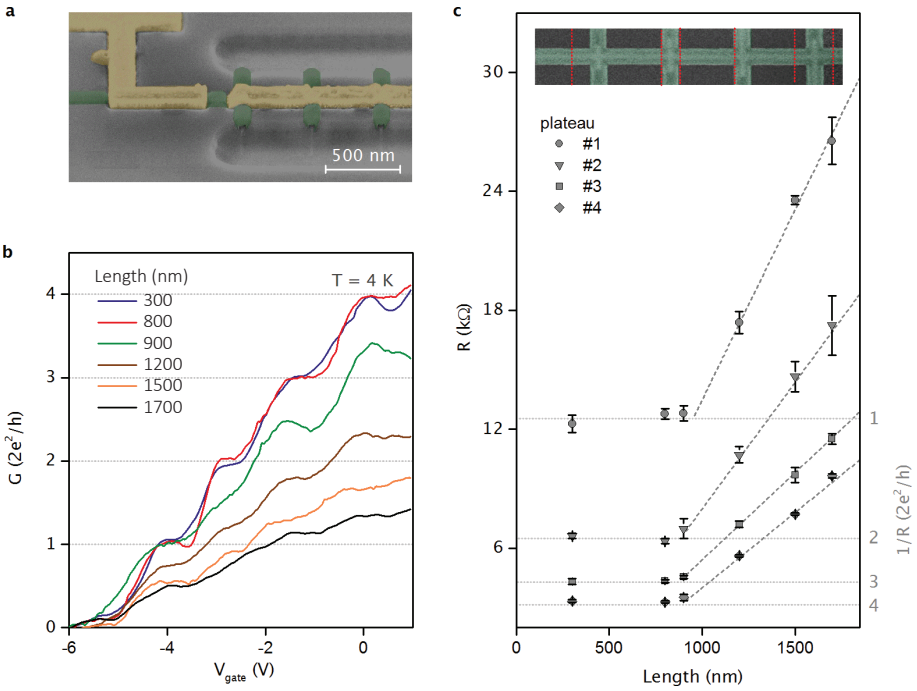

Figure 7.1 | Long mean free path in template-assisted grown InAs nanowires. a, The scanning electron image shows the template (green), the substrate (gray), and the metallic contacts (yellow). InAs nanowires (not visible) are grown inside the template. Contacts are realized by selectively removing the template at the contact areas. This method also allows for growing nanowire cross-junctions. Image shows a device with ~ 200 nm channel length. **b,** Conductance as a function of back gate voltage shows quantized plateaus up to 800 nm channel length. For longer channels quantization is lost, but plateaus can still be identified. **c,** Distribution of plateaus in resistance for varying channel lengths. For channels shorter than 800 nm, the resistance of the channel is determined by the number of occupied modes, demonstrating one-dimensional ballistic transport. Dashed lines indicate $R = (nG_0)^{-1} \times (1 + l_c/l_e)$, with n the number of modes, G_0 the conductance quantum, l_c the channel length, and $l_e \sim 1\,\mu$m the mean free path. Inset shows a device before realizing the contacts. Red lines indicate the position of the right metallic contact for each device with a different channel length. Left contact is on y-axis (outside the image) whose position is fixed for all devices. All panels adapted from [3].

A physical separation of the transport channel from scattering regions has been central in developing today's high-mobility material systems. Transport through a nanowire is naturally prone to surface scattering due to the high surface-to-volume ratio. However, it is possible to separate the nanowire channel from the surface, for example with an insulating shell enclosing the channel. This idea has been implemented for InAs nanowires using a InP shell which has increased the mobility significantly [2]. Similarly, very recently Ref. [3] has demonstrated a notable improvement in mean free path by growing InAs nanowires within a predefined template which limits the exposure of the channel to ambient and adsorbents, see Figure 7.1. This method has resulted in clear signatures of ballistic transport for channel lengths up to 800 nm, whereas a fabrication equivalent to the one reported in this dissertation has showed ballistic transport in InSb nanowire channels up to 400 nm [4].

Chapter 4

Increasing the uniformity of the nanowire–superconductor interface resulted in a hard superconducting gap and supercurrent in the InSb nanowire which persisted in the presence of magnetic fields. The interface improvements due to noninvasive cleaning of the nanowire surface and inclusion of a wetting layer before the superconductor deposition provide a technical guideline for inducing superconductivity also for other material systems, for example topological insulators. However, despite these improvements, the nanowire–superconductor interface still has a residual barrier, evident from the signatures of dot formation between the contacts and from the absence of quantized conductance plateaus.[1] We previously discussed that the ambient exposure of the wire surface, which was unavoidable in our process, could result in formation of an interface barrier. However, ambient exposure of the interface can be avoided in more advanced realizations of Majorana wires, for example in hybrid wires with an as-grown semiconductor–superconductor interface [6]. Another alternative is to employ more selective in situ cleaning techniques that can clean the wire surface more effectively while keeping the crystalline structure pristine. Figure 7.2 shows such a method that has been developed

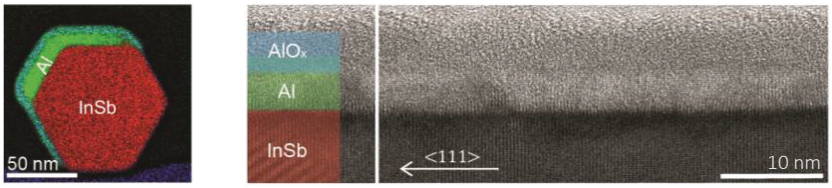

Figure 7.2 | InSb nanowires with in situ hydrogen-cleaned surface. Left panel shows the cross-sectional image of an InSb nanowire whose surface is in situ hydrogen cleaned prior to the growth of a thin Al film which covers two facets of the wire continuously along its axis. Right panel shows a transmission electron image of the wire, with the <100> wire axis indicated. The thin Al film is coving the wire continuously. The nanowire–superconductor interface appears crystalline and impurity-free. Both panels taken from [7].

[1] Conductance plateaus can be regularly observed for InSb nanowire devices with equivalent geometry but two normal metal contacts [5] or when one of the superconducting contacts is replaced with a normal metal one, as reported in chapter 5.

for InSb nanowires [7]. Here, the wire native oxide is in situ cleaned with hydrogen prior to superconductor film growth. This technique has been shown to remove the interface barrier to great extent [8]. Eliminating this barrier or its variation from device to device is an important step towards realizing a topological quantum computer based on semiconductor nanowires. This is because scalable designs involve many Majorana wires which are coupled to each other through a normal conducting wire section. Figure 7.3 shows an example where Majorana wires are connected via gate-defined quantum dots [9]. Here, the presence of unwanted barriers would pose a difficulty in operation of large-scale Majorana network devices.

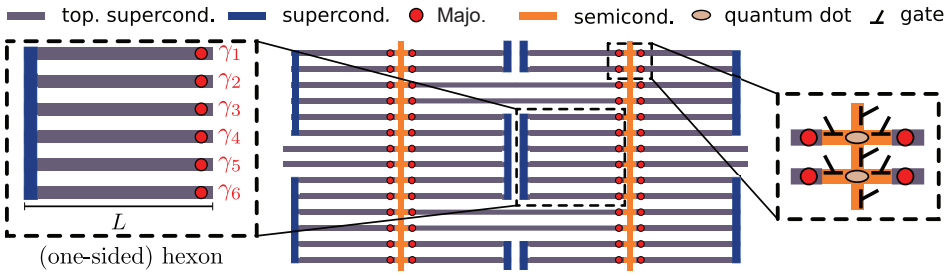

Figure 7.3 | A scalable architecture for topological qubits based on Majorana wires. The minimal building block is a topological Cooper pair box containing six Majoranas, here called the hexons, magnified on the left hand side. The operation of the topological qubit relies on selective coupling of Majoranas to nearby quantum dots defined by gates, depicted in the magnified panel on the right. Adapted from [9].

7

Chapter 5

The device improvements reported in the previous chapters resulted in ballistic transport in InSb nanowires with induced superconductivity. The structural and chemical analyses of the measured device confirmed the high-quality interface between the nanowire and the NbTiN superconductor. The numerical analysis indicated a mean free path on the order of the length of the proximitized wire. These results constitute a substantial improvement in induced superconductivity in semiconductor nanowires. However, the presence of magnetic-field-induced subgap states is a crucial shortcoming of the reported approach to realize Majorana nanowire qubits. This is because the non-trival topology of Majorana wires rely on fermion parity conservation which subgap states can violate by allowing single electron tunneling, the so-called quasiparticle poisoning [10]. We speculate that these magnetic-field-induced subgap states are due to vortex formation in NbTiN, a type-II superconductor. Numerical simulations of our devices using Ginzburg–Landau model have shown that within the magnetic field range of our experiments the NbTiN film becomes populated with vortices which nucleate at the nanowire–superconductor interface [11].

It is possible to eliminate or decrease the number of vortices by using a type I superconductor with a long coherence length, the length scale defining the size of a vortex. Because superconductors with a long coherence length generally have small critical magnetic fields, one must additionally decrease the cross-sectional area of the super-

conductor normal to the magnetic field direction to retain superconductivity. This has been realized in InAs and InSb nanowires interfacing aluminum, a superconductor with a long coherence length, which is grown at low temperatures to guarantee the continuity of the film on the nanowire for very small film thickness (< 10 nm) [6, 7]. Figure 7.2 shows such a realization for an InSb nanowire. The nanowire shows a significantly decreased magnetic-field-induced subgap states [7, 12], shown in Figure 7.4.

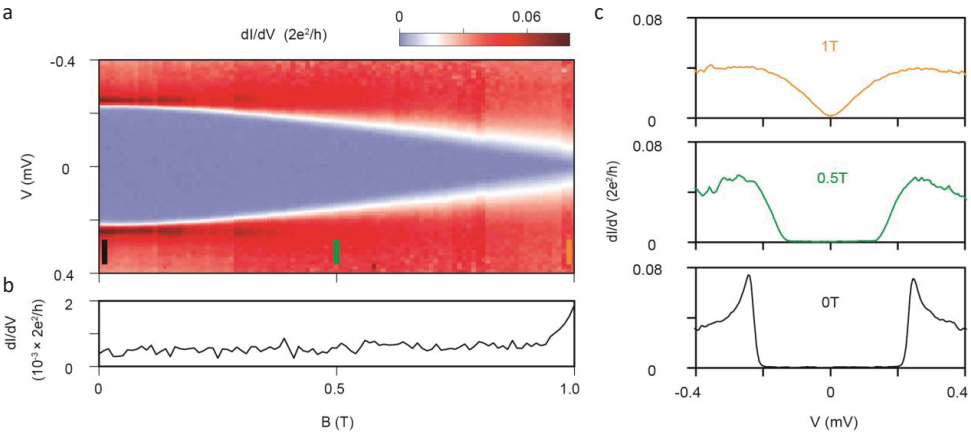

Figure 7.4 | Hard superconducting gap in InSb nanowires interfacing a thin Al film at finite magnetic fields. **a,** Differential conductance of the InSb nanowire device as a function of bias voltage and in-plane magnetic field. The measurement is taken in the tunneling regime resolving the induced superconducting gap ~ 0.2 meV. As the magnetic field increases, the induced gap shrinks, but the subgap conductance stays constant at a value close to zero. **b,** Horizontal line cut from **a** for zero bias voltage. **c,** Vertical line cuts from **a** for the magnetic field values indicated with colored bars. All panels adapted from [7].

Chapter 6

Owing to the device improvements reported in the previous chapters we were able to demonstrate rigid zero bias peaks that are stable over an extended range in Zeeman energy and gate voltage in nanowire devices that show ballistic transport properties. Our observations exclude alternative explanations of the reported zero bias peaks that are based on disorder and support a Majorana interpretation. Nevertheless, the experiments did not show a zero bias peak with a quantized conductance value of $2e^2/h$, a predicted hallmark of Majoranas [13].

A Majorana zero bias peak (ZBP) is expected to reach its quantized value in the zero temperature limit. However, finite temperatures can decrease the height of the ZBP, whose width, in this case, becomes set by the temperature T via FWHM $\sim 3.5 k_B T$. Here FWHM is the full width at half maximum, and k_B the Boltzmann constant. Our reported FWHM $\gtrsim 20\,\mu$eV corresponds to $T \gtrsim 65$ mK which is larger than the estimated electron temperature ~ 50 mK. Below we discuss a mechanism which could result in an additional broadening of the ZBP, recently put forward by Liu et al [14].

Liu et al numerically simulated the nanowire devices used in our experiment with parameters taken from the measurement, and were able to reproduce our results assum-

ing a dissipation term in the Hamiltonian, shown in Figure 7.5. The source of dissipation was argued to be the presence of vortices in our NbTiN film. Here, a vortex core acts as a fermion bath that can result in a loss of energy and particles. This broadens the ZBP lowering its height, similar to the effect of temperature. Above we discussed that the use of a type I superconductor can eliminate vortex formation, and could allow for a Majorana ZBP reaching its quantized value. Indeed, very recent studies which use aluminum have reported ZBPs approaching $2e^2/h$ [8, 15], much higher than what we reported in this dissertation.

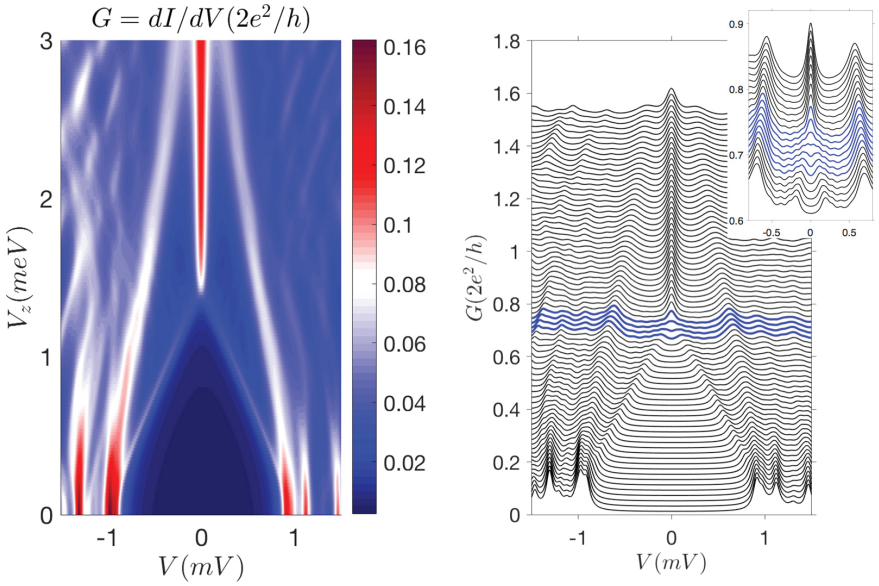

Figure 7.5 | Numerical simulation of the Majorana nanowire devices used in our experiment. Left panel shows the differential conductance as a function of bias voltage and a magnetic along the wire axis. Line traces are plotted on the right with an offset. Inset zooms in on the small bias range around the critical magnetic field. Simulation assumes ballistic transport through a proximitized wire section of length ~ 1.3 μm, an induced gap of 0.9 meV at zero magnetic field, a g factor ~ 40, a spin–orbit energy ~ 0.25 meV, two occupied subbands, and the presence of dissipation. Compare with Figure 6.4 in the previous chapter.

References

[1] Yi, W. et al. Gate-tunable high mobility remote-doped InSb/$In_{1-x}Al_xSb$ quantum well heterostructures. *Appl. Phys. Lett.* **106,** 142103 (2015)

[2] Jiang, X. et al. InAs/InP radial nanowire heterostructures as high electron mobility devices. *Nano Lett.* **7,** 3214 (2007)

[3] Gooth, J. et al. Ballistic one-dimensional InAs nanowire cross-junction interconnects. *Nano Lett.* **17,** 2596 (2017)

[4] Kammhuber, J. Spin-orbit interaction in ballistic nanowire devices. PhD thesis, Delft University of Technology (2017)

[5] Kammhuber, J. et al. Conductance quantization at zero magnetic field in InSb nanowires. *Nano Lett.* **16,** 3482 (2016)

[6] Krogstrup, P. et al. Epitaxy of semiconductor–superconductor nanowires. *Nature Mater.* **14,** 400 (2015)

[7] Gazibegovic, S. et al. Epitaxy of advanced nanowire quantum devices. arXiv:1705.01480 (2017)

[8] Wang, G. In search of quantized Majorana zero-bias peaks. MSc thesis, Delft University of Technology (2017)

[9] Karzig, T. et al. Scalable designs for quasiparticle-poisoning-protected topological quantum computation with Majorana zero modes. *Phys. Rev. B* **95,** 235305 (2017)

[10] Rainis, D. & Loss, D. Majorana qubit decoherence by quasiparticle poisoning. *Phys. Rev. B* **85,** 174533 (2012)

[11] Garaud, J. Private communication (2016)

[12] Deng, M. T. et al. Majorana bound state in a coupled quantum-dot hybrid-nanowire system. *Science* **354,** 1557 (2016)

[13] Law, K. T.; Lee, P. A. & Ng, T. K. Majorana Fermion Induced Resonant Andreev Reflection. *Phys. Rev. Lett.* **103,** 237001 (2009)

[14] Liu, C.-X.; Sau, J. D. & Das Sarma, S. Role of dissipation in realistic Majorana nanowires. *Phys. Rev. B* **95,** 054502 (2017)

[15] Nichele, F. et al. Scaling of Majorana zero-bias conductance peaks. arXiv:1706.07033 (2017)

Acknowledgements

The four and a half years I have spent in Delft turned out to be the best part of my life. Like everything, however, it had to end. Sad to leave behind, but at the same time comforting to realize one can learn so many different things and form so many bonds, both professionally and personally, anywhere at any age.

I clearly remember how I was charmed by **Leo**, the superstar of quantum transport, into doing a PhD on Majoranas even though I had initially considered other fields for a change. Besides making offers one cannot refuse, your ability to identify the most important problems in condensed matter and your endless motivation to learn from every experiment and calculation are some of the traits I hope to have acquired by working with you. Your team grew in size but you have always stayed on top of physics. Thank you for giving me the opportunity to work on such a big, challenging and highly visible project. It was a great experience, and I will strive for reaching this level of scientific excellence in the rest of my career. I wish you all the best in your endeavor to realize a topological quantum computer.

Before going into the personal details of my PhD, here I thank my committee. **Erik**, I am grateful to you for being my second promotor, I acknowledge you once again five paragraphs below. **Charlie**, thank you for being in my committee, and kindly considering remarks on your drafts. Your research has been an indispensable source of motivation during my PhD. **Silvano**, I really enjoyed your critical questions in Basel after my first ever invited talk. Thank you for being in my committee, and I hope you will not go easy on me also this time. **Lieven**, I am indebted to you for taking part even though I picked the defense date within the only time frame you told me is not good. **Yaroslav**, thank you for taking your time to referee this dissertation. **Srijit**, I am grateful to you for being in my committee, you are acknowledged once again seven paragraphs below.

Also my sincere thanks to **Philip** for taking me without a degree, and allowing me to finish the final parts of this dissertation in his lab.

Right from the start of my PhD, I have been quickly welcomed to the lab by **Kun**, **Daniel**, **Vincent** and **David**, a set of people who will likely remain the most friendly but at the same time the most intimidating group (gang?) I have encountered in a professional setting. I thought twice about joining the team after my interview dinner but the offer was unrefusable. And fortunately so. David, thank you for being my mentor in the first months, not only for helping me getting started and patiently answering all my questions, but also for allowing me to integrate to QT easily. We have entirely different approaches in our work, and watching you succeed very well in your research has taught me a lot. I am happy to have collaborated with you on many projects. Vincent, I admit that we had friction from time to time, but it was only because your opinion mattered to me. You were tough but always on point in your criticism, which shaped my scientific personality. I hope you consider those heated discussions as insignificant details not affecting the big and positive picture—I am very glad that our collaboration has resulted

in papers, and hope to see you and Marieke somewhere soon. Kun, you were the calmer side of the fantastic duo, and all those things I mention above for Vincent holds for you as well. I have both enjoyed and benefited a lot from working with you. I am happy that you are back in academia, we might keep in touch regularly at conferences and share our love for cats for many years. All the best with Miao. Daniel, we didn't end up working together that closely but we have surely connected on many other levels. Our trip to Sicily was a memorable experience, and so were the many other trips we had and the parties we have been to. It was very nice to have you as a house mate, thank you for showing me how to be in the moment. I wish you and Sára great time together.

My first year turned out to be productive owing to **Ilse**. I was fortunate enough to work with you from the early on to have my scientific character shaped by your methodical approach. Thank you for setting me a good example; the contrast between my office desk and my clean room notes is all you. The productivity persisted by the inclusion of two truly great master students to our team, **Fokko** and **Jasper**. I am not overstating when I say the biggest part of this dissertation is based on your work. You showed your eagerness to learn in many ways. Your independence resulted in us learning from you, and together we made it work in the end. Jasper, my first master student, I still remember how proud I felt when you defended your thesis super smoothly. I am glad that you stayed for a PhD in our group.

Enter **Hao** and **Michiel** around one and a half years in. You arrival marks an apparent push to the Majorana project. We formed the team very naturally and immediately started tackling problems in a fundamental and systematic way. Later, Michiel had to go but Hao could stay. Thank god. (the one in Delft, the only one I believe) Together we overcame the scientific and management challenges, and our collaboration resulted in a lot of papers giving us what we needed to stay in the game. I cannot thank you enough for being both a workhorse and an experienced postdoc at the same time, while patiently tolerating all my ups and downs. Hopefully everything will work out for both of us and we will continue our collaboration in the future. For now, I am happy to see you make a good team with Michiel again, and with motivated students **Di**, **Guan**, **Nick**, and of course Jouri. **Jouri**, it was a bummer we didn't overlap longer, I enjoyed working with you a lot and getting exposed to your precise questions. I really liked the fact that I had to convince you even for small things, you never took my word for it, always asked for a solid explanation and made me think. On top of all that, after spending a bit of time outside lab, it became crystal clear that we had the same interest in music, a highly pleasant coincidence.

Erik, your team's contribution was integral for this dissertation. The fact that I have more papers with you than with Leo tells a lot about how important your nanowires have been for my research. It was always informative to hear your scientific point of view, and I hope to work with you again in the future if all goes according to plan. **Sébastien**, likewise, you are greatly acknowledged for your contribution to the InSb nanowire growth in Eindhoven. **Diana**, we currently have nine papers together, how cool is that? It was so much fun to have you around, not only in the lab during measuring, but also whenever we did organics or acids together, even when we failed to actually make a device. You can be quite intense and unpredictable, but also very loving which is all that matters. I promise I will visit you and Markus at your new place in the first opportunity. I expect to

see you both fully awake until sunrise, so please be prepared.

Maja, thank you for the collaboration which resulted in four papers together, for believing in my story and encouraging me to keep going. Your remarks on drafts were very useful, always contributing to the paper. I really enjoyed our late night tour on Mullholland Dr, thank you for being a perfect guide during our trip, it was a lot of fun. **Attila**, here I admit that a considerable part of this dissertation (more than you think) was an effort to convince you of my story. I vividly remember measuring the first Andreev enhancement signal just to prove a point after a conversation of ours, and including it in my slides for my werkbespreking the next day. (Turned out to be a bad talk since I chose to analyze data instead of sleeping.) Your critical remarks which shaped this work are greatly acknowledged. **Jakob**, your work played a key role in making ballistic transport the new standard in semiconductor nanowires, evidenced by our dissertation titles. We not only managed to have papers together, but also spent great time listening to the songs of your people.

Srijit, your expertise in boron nitride transfer has been productive for the wire team as well. Your innovative yet down to earth approach was influential in shaping my research path after PhD. Your remarks on drafts were eye openers, you could easily see the holes in the story, and change how I choose to present the data. I hope to be able to send you more drafts and get your feedback, and maybe even collaborate in the very near future. It was always a pleasure to finish the night outs with you towards the early morning.

This clean room heavy dissertation could not have been completed without my theory collaborators **Michael** and **Michał**. Thank you very much for your calculations, for being approachable and pleasant to ask questions to, be it about the experiment, or just some random thing I thought during shower. Our discussions kept my feet on the ground. **Anton**, our discussions had somehow the opposite effect, but your critical views on widely accepted interpretations consistently got me question what I thought I knew. Thank you for that. **Kevin**, we overlapped only briefly, but I was able to benefit from our discussions.

The materials studies in this dissertation involved various collaborations. **Marina**, your work on superconducting films was indispensable. I greatly benefited from our discussions about all sorts of details about sputtering. **Sonia**, your TEM analyses were an essential addition to our experiments. Thank you for showing us what we were actually measuring, and also for being open to collaborating. **Sebastian**, your work on lamellae is greatly acknowledged. **Kenji** and **Takashi** sensei, thank you for providing the hBN flakes, I will continue using your crystals.

Some contributions may not end up written in publications no matter the importance. **Remco**, **Mark**, **Bram**, **Jelle**, **Siebe**, and **Olaf**, your input to the research coming out of QuTech (actually almost the entire Lorentzweg 1) is invaluable, this dissertation could not be completed if it wasn't for you. Your relaxed vibes make it a pleasure to chat with you about anything, not only work. **Raymond** & **Raymond** and **Marijn**, you are greatly acknowledged for your contribution to the measurement electronics, QuTech is very lucky to have you on board. **Jason**, B013 has kept its functionality thanks to you even though it's complexity has increased tremendously. **Nick**, your efforts on fabrication improvements are greatly acknowledged. **Marja**, **Yuki**, **Simone**, **Jenny**, **Heera** and **Joanna**,

thank you for making everything run smooth, you were always willing to help even when it was far beyond your job description. Finally, I acknowledge the **clean room staff** without whom I cannot imagine how I would complete a dissertation involving around a thousand nanowire devices.

During my time in Delft, I was lucky enough to be a part of one of the nicest offices one can imagine. **Julia**, **Arjan** and **Jakob**, thank you very much for providing the relaxed and fun atmosphere of B016. The combination of Julia's smile, Arjan's chill, and Jakob's pleasant conversations felt like a blessing amid PhD chaos. I am so happy that we all survived the hard times and have now smoother paths ahead. Julia, also thanks a lot for your help in communicating our work. **Jie**, I am very thankful for our uplifting late night conversations, you always managed to cheer me up. Your advices on career and writing papers were inspiring and I especially want to acknowledge you for motivating me to make a good story out of a pile of data and slides, which came together nicely in the end thanks to your encouragement. I also thank sincerely the entire **Topo team** for contributing to the atmosphere I really enjoyed to be in. I wish you all the best in your careers and hope to cross paths sometime somewhere. Please consider that if we all end up in academia, we will have an easier time with the referees.

PhD life can be quite intense when the expectation vs reality gap is large. Even with long working hours, all nighters, lab weekenders, sometimes things just don't work no matter what you do for reasons no one can know why. I was very fortunate to be surrounded by many great people who helped me to carry on when that happened, and showed me there is more to life than working. I got a head start thanks to **Floris** and **Wolfgang** who took me as their house mate to Kloksteeg 23, a magic place facilitating so many connections. It was very nice to share the house, and your friendly welcome which let me blend in with the QT life smoothly. You guys left for postdoc but the house kept its charm to attract the finest residents. First Daniel moved in ever so naturally, and then following his suggestion, we asked Stefan to join. **Stefan**, I feel lucky to have our paths crossed, knowing you gave me new perspectives on what to look for in a friend. You were always in good mood to hang out, a perfect partner to have fun or be sad with. Having you as a house mate kept me sane during the hardest periods. As if all this was not enough, I have made many good friends thanks to you, it is remarkable how you manage to gather the best people around. You throw a casual party and I end up getting married to one of your guests, with you being the best man. We run into a random friend of yours who ends up taking creepy photos of me sleeping on the plane, and even that guy becomes my inseparable friend. Everyone you touch turns into gold, I hope you make the right choice for your postdoc. (I can help you decide) **Vidak**, thank you for letting me know you first before showing me those photos. Also for being so chill and effortlessly fun, and for making me forget regularly that I have a PhD to finish. You are the best (de)crime partner I can ever wish for to listen to music, meet new people and dance. Or even make people dance for an entire night playing our favorite tunes! I hope you will wait for me and we will continue from where we left off. But even if you leave, there is always a job at McDonald's, and McDonald's in every country. **Nodar**, your move in was so organic that the only difference was you going to sleep using the stairs instead of the door. You are very gentle and friendly, forming a surprising contrast to your looks. We first shared the neighboring offices, then the neighboring rooms, ranted about work,

had deep conversations on life, chill weekends under the sun and dark sweaty parties in basements with lots of hugs. It was very fulfilling to be around you and your endless love. Thank you for helping me survive my PhD, I hope we end up living closely and keep what we have going for the rest of our lives. **LeChuck**, my most royal companion in Delft, thank you for your constant presence during my PhD. Spending time with you even for a few minutes could strip me off all the stress. You made me realize how much I loved you when you briefly run away. We might part our ways, but I want you know that it's all for your own good.

My life and our living room has hosted many people who were a joy to spend time with. **Anais**, I feel lucky to keep the close connection, I especially like your views on gender and food, I hope to visit you very soon. **Michiel**, sorry to make you listen the same part of the song over and over again whenever I put on some music. **James**, your food is great, also your photography, but your taste in videos is just too weird. **Alex**, you are one of the nicest people to get drunk with. **Ana**, I love your food and your motivation. "Of course you can do it, you just have to want it." I really hope we ride your bike someday. **Piermarco**, our day and night outs ended up being deeply bonding experiences. **Klaus**, your competitiveness can only be matched by your friendliness. **Christian**, you should trademark your eccentric ideas on quantum internet considering they sell well in men's magazines. **Emre**, so nice that you and Yasemin will join us here in Cambridge. **Peter**, I am happy to pass on the honor of being a resident of Kloksteeg 23 to you. **Hannes** and **Yun**, thank you for helping with our move and for your social presence. **Alessandro**, **Nandini**, **Stijn**, **Natalia**, **Machiel**, **Debbie**, **Kaan** I am glad to have crossed paths with you and I very much hope seeing you again.

I also thank my mentors and advisors in Jülich without whom it would not be possible for me to even start this PhD. I am greatly indebted to **Yusuf**, **Christian**, **Thomas** and **Hans** for not only introducing me to physics, but also showing me how science is done and helping me choose a research path. Yusuf, I especially thank you for our video conversations which have always been a source of motivation during the hard times. It was an honor to be your best man and I hope to see you in the next opportunity.

I finally thank **my family** whose endless love and support has allowed me to pursue this path. My dear parents, I am inspired by your motivation to learn which you keep still today. My lovely twin sister, I feel lucky to go through similar stages of life with you and have your support. It was a nice coincidence to end up with you in the same country after many years, and also great to know we will unite again for our postdocs. Last words go to my wife Tanja who has been there for me in this journey, patiently enduring the downs and joyfully celebrating the ups with me. Thank you for that Sunday morning in Belgrade, for dancing together through many nights, for explanations of art, for being my safe haven in difficult times, for encouraging me in work and in music, and for coming here with me all the way across an ocean. I am happy that our days apart have finally ended and looking forward to our shared future.

Curriculum Vitæ

Önder GÜL

06 Oct 1987 Born in Konya, Turkey

Education

2001–2006 Secondary school
Deutsche Schule Istanbul, Turkey

2006–2012 Dipl.-Ing., Electrical Engineering and Information Technology
RWTH Aachen University, Germany
Thesis: Phase-coherent transport in GaAs/InAs core/shell nanowires
Advisor: Prof. Dr. Thomas Schäpers

2013–2017 PhD, Applied Sciences
Delft University of Technology, Netherlands
Thesis: Ballistic Majorana nanowire devices
Advisor: Prof. Dr. Leo P. Kouwenhoven

Employment

2009 Research assistant
Electronic Materials Research Lab (EMRL)
RWTH Aachen University, Germany
Advisor: Prof. Dr. Rainer Waser

2010–2012 Research assistant
Peter Grünberg Institute (PGI-9)
Forschungszentrum Jülich, Germany
Advisor: Prof. Dr. Thomas Schäpers

2017– Postdoctoral researcher
Department of Physics
Harvard University, USA
Advisor: Prof. Dr. Philip Kim

List of Publications

* Equal contribution

14. *Spin–orbit interaction and orbital effect of magnetic field in Majorana nanowire devices*
Jouri D.S. Bommer*, Hao Zhang*, **Önder Gül***, Piotr Rożek, Bas Nijholt, Diana Car, Sébastien R. Plissard, Erik P.A.M. Bakkers, Kenji Watanabe, Takashi Taniguchi, Michael Wimmer, Leo P. Kouwenhoven
in preparation

13. *Ballistic Majorana nanowire devices*
Önder Gül*, Hao Zhang*, Jouri D.S. Bommer*, Michiel W.A. de Moor, Diana Car, Sébastien R. Plissard, Erik P.A.M. Bakkers, Attila Geresdi, Kenji Watanabe, Takashi Taniguchi, Leo P. Kouwenhoven
submitted to *Nature Nanotechnology*

12. *Observation of conductance quantization in InSb nanowire networks*
Elham M.T. Fadaly, Hao Zhang, Sonia Conesa-Boj, Diana Car, **Önder Gül**, Roy L.M. op het Veld, Sébastien R. Plissard, Sebastian Koelling, Leo P. Kouwenhoven, Erik P.A.M. Bakkers
Nano Letters (in press)

11. *Conductance through a helical state in an InSb nanowire*
Jakob Kammhuber, Maja C. Cassidy, Fei Pei, Michał P. Nowak, Adriaan Vuik, **Önder Gül**, Diana Car, Sébastien R. Plissard, Erik P.A.M. Bakkers, Michael Wimmer, Leo P. Kouwenhoven
Nature Communications **8**, 478 (2017)

10. *Ballistic superconductivity in semiconductor nanowires*
Hao Zhang*, **Önder Gül***, Sonia Conesa-Boj, Michał P. Nowak, Michael Wimmer, Kun Zuo, Vincent Mourik, Folkert K. de Vries, Jasper van Veen, Michiel W.A. de Moor, Jouri D.S. Bommer, David J. van Woerkom, Diana Car, Sébastien R. Plissard, Erik P.A.M. Bakkers, Marina Quintero-Pérez, Maja C. Cassidy, Sebastian Koelling, Srijit Goswami, Kenji Watanabe, Takashi Taniguchi, Leo P. Kouwenhoven
Nature Communications **8**, 16025 (2017)

9. *Hard superconducting gap in InSb nanowires*
Önder Gül, Hao Zhang, Folkert K. de Vries, Jasper van Veen, Kun Zuo, Vincent Mourik, Sonia Conesa-Boj, Michał P. Nowak, David J. van Woerkom, Marina Quintero-Pérez, Maja C. Cassidy, Attila Geresdi, Sebastian Koelling, Diana Car, Sébastien R. Plissard, Erik P.A.M. Bakkers, Leo P. Kouwenhoven
Nano Letters **17**, 2690 (2017)

8. *InSb nanowires with built-in $Ga_xIn_{1-x}Sb$ tunnel barriers for Majorana devices*
Diana Car, Sonia Conesa-Boj, Hao Zhang, Roy L.M. op het Veld, Michiel W.A. de Moor, Elham M.T. Fadaly, **Önder Gül**, Sebastian Koelling, Sébastien R. Plissard, Vigidis Toresen, Michael Wimmer, Kenji Watanabe, Takashi Taniguchi, Leo P. Kouwenhoven, Erik P.A.M. Bakkers
Nano Letters **17**, 721 (2016)

7. *Revealing the band structure of InSb nanowires by high-field magnetotransport in the quasiballistic regime*
Florian Vigneau, **Önder Gül**, Yann-Michel Niquet, Diana Car, Sebastien R. Plissard, Walter Escoffier, Erik P.A.M. Bakkers, Ivan Duchemin, Bertrand Raquet, Michel Goiran
Physical Review B **94**, 235303 (2016)

6. *Conductance quantization at zero magnetic field in InSb nanowires*
Jakob Kammhuber, Maja C. Cassidy, Hao Zhang, **Önder Gül**, Fei Pei, Michiel W.A. de Moor, Bas Nijholt, Kenji Watanabe, Takashi Taniguchi, Diana Car, Sébastien R. Plissard, Erik P.A.M. Bakkers, Leo P. Kouwenhoven
Nano Letters **16**, 3482 (2016)

5. *Towards high mobility InSb nanowire devices*
Önder Gül*, David J. van Woerkom*, Ilse van Weperen*, Diana Car, Sébastien R. Plissard, Erik P.A.M. Bakkers, Leo P. Kouwenhoven
Nanotechnology **26**, 215202 (2015)

4. *Giant magnetoconductance oscillations in hybrid superconductor–semiconductor core/shell nanowire devices*
Önder Gül*, H. Yusuf Günel*, Hans Lüth, Torsten Rieger, Tobias Wenz, Fabian Haas, Mihail Lepsa, Gregor Panaitov, Detlev Grützmacher, Thomas Schäpers
Nano Letters **14**, 6269 (2014)

3. *Flux periodic magnetoconductance oscillations in GaAs/InAs core/shell nanowires*
Önder Gül, Nataliya Demarina, Christian Blömers, Torsten Rieger, Hans Lüth, Mihail I. Lepsa, Detlev Grützmacher, Thomas Schäpers
Physical Review B **89**, 045417 (2014)

2. *Realization of nanoscaled tubular conductors by means of GaAs/InAs core/shell nanowires*
Christian Blömers, Torsten Rieger, Patrick Zellekens, Fabian Haas, Mihail I. Lepsa, Hilde Hardtdegen, **Önder Gül**, Nataliya Demarina, Detlev Grützmacher, Hans Lüth, Thomas Schäpers
Nanotechnology **24**, 035203 (2013)

1. *Comparison of InAs nanowire conductivity: influence of growth method and structure*
Kamil Sladek, Andreas Winden, Stephan Wirths, Karl Weis, Christian Blömers, **Önder Gül**, Thomas Grap, Steffi Lenk, Martina von der Ahe, Thomas E. Weirich, Hilde Hardtdegen, Mihail Ion Lepsa, Andrey Lysov, Zi-An Li, Werner Prost, Franz-Josef Tegude, Hans Lüth, Thomas Schäpers, Detlev Grützmacher
Physica Status Solidi (c) **9**, 230 (2012)

TU Delft

Casimir PhD Series 2017-29
ISBN 978-90-8593-313-7

Propositions

accompanying the dissertation

Ballistic Majorana nanowire devices

by

Önder GÜL

1. Zero-energy signatures of Majoranas cannot be explained by any existing theory based on disorder.

   Chapter 6 of this dissertation

2. Increasing the uniformity of a semiconductor–superconductor interface reduces the density of states in the semiconductor at energies within the superconducting gap.

   Chapters 4 and 5 of this dissertation

3. It is impossible to experimentally disprove a scientific hypothesis in isolation.

   Duhem–Quine thesis

4. Scientific theories persist owing to their applicability, not to their ability to describe the universe consistently.

5. A researcher's primary duty for the advancement of science is to be self-critical.

6. Increasing the representation of the researchers on temporary contracts in the governance of universities can increase the job satisfaction in academia.

7. Punishments should be replaced with rehabilitation to advance morality.

8. Productivity of a society is maximized when it results from self-expression of individuals.

9. Living on a tight schedule limits tolerance and creativity.

These propositions are regarded as opposable and defendable, and have been approved as such by the promotor Prof. Dr. L. P. Kouwenhoven.

Stellingen

behorende bij het proefschrift

Ballistic Majorana nanowire devices

door

Önder GÜL

1. Kenmerken van Majorana's bij nul energie kunnen niet worden verklaard door bestaande theorieën op basis van wanorde.

   Hoofdstuk 6 van dit proefschrift

2. Het verhogen van de uniformiteit van een halfgeleider–supergeleider interface vermindert de toestandsdichtheid in de halfgeleider bij energieën binnen de supergeleidende gap.

   Hoofdstukken 4 and 5 van dit proefschrift

3. Het is onmogelijk om een op zichzelf staande wetenschappelijke hypothese experimenteel te weerleggen.

   Duhem–Quinestelling

4. Wetenschappelijke theorieën volharden door hun toepasbaarheid, niet door hun vermogen om het universum consistent te beschrijven.

5. De voornaamste taak van een onderzoeker voor de vooruitgang van de wetenschap is om zelfkritisch te zijn.

6. Het vergroten van de vertegenwoordiging van onderzoekers die tijdelijke contracten hebben in het bestuur van universiteiten kan de werktevredenheid in de academische wereld vergroten.

7. Straffen moeten worden vervangen door rehabilitatie om de moraliteit te bevorderen.

8. Productiviteit van een samenleving wordt gemaximalizeerd als ze voortvloeit uit de zelfexpressie van individuen.

9. Het leven volgens een strak schema beperkt tolerantie en creativiteit.

Deze stellingen worden opponeerbaar en verdedigbaar geacht en zijn als zodanig goedgekeurd door de promotor Prof. Dr. L. P. Kouwenhoven.